New Multi-Pulse Diode Rectifier Average Models for AC and DC Power Systems Studies

Huiyu Zhu

Dissertation submitted to the Faculty of the Virginia Polytechnic Institute and State University in partial fulfillment of the requirements for the degree of

DOCTOR OF PHILOSOPHY

in

ELECTRICAL ENGINEERING

APPROVED:

Prof. Douglas K. Lindner

Prof. Dushan Boroyevich

Prof. Fred Wang

Prof. Rolando Burgos

Prof. Yilu Liu

Prof. Donald J. Leo

December 13, 2005
Blacksburg, Virginia

Keywords: multi-phase diode rectifier, average model, system harmonic resonance, optimization using genetic algorithm

Copyright 2005, Huiyu Zhu

New Multi-Pulse Diode Rectifier Average Models for AC and DC Power Systems Studies

by

Huiyu Zhu
Chairman: Douglas K. Linder
The Bradley Electrical and Computer Engineering Department

ABSTRACT

More power semiconductors are applying to the aircraft power system to make the system smaller, lighter and more reliable. Average models provide a good solution to system simulation and can also serve as the basis to derive the small signal model for system-level study using linear control theory.

A new average modeling approach for three-phase and nine-phase diode rectifiers with improved ac and dc dynamics is proposed in this dissertation. The key assumption is to model the load current using its first-order Taylor Series expansion throughout the entire averaging time span. A thorough comparison in the time domain is given of this model and two additional average models that were developed based on different load current assumptions, using the detailed switching models as the benchmark. The proposed average model is further verified by experimental results.

In the frequency domain, the output impedance of a nine-phase diode rectifier is derived, and the sampling effect in the average model is investigated by Fourier analysis.

The feeder's impedance before the rectifier is modeled differently in the output impedance in contrast in the equivalent commutation inductance.

The average model is applied to the resonance study in a system composed of a synchronous generator, a nine-phase diode rectifier and a motor drive. The Thevenin's and Norton's equivalent circuits are derived to construct a linearized system. The equivalent impedances are derived from the average models, and the source are obtained from the switching circuit by short-circuit or open-circuit. Transfer functions are derived from the harmonic sources to the bus capacitor voltage for resonance study. The relationship between the stability and the resonance is analyzed, and the effect of controllers on the resonance is investigated.

Optimization is another system-level application of the average model. A half-bridge circuit with piezoelectric actuator as its load is optimized using genetic algorithm. The optimization provides the possibility to design the actuator and its driving circuit automatically.

ACKNOWLEDGEMENT

I would first like to thank my advisor, Dr. Douglas K. Lindner, who always gives me the encouragement and support in my research work. From him, I learned not only the knowledge, but to have the right attitude towards research.

I would take this opportunity to express my sincere appreciation to the faculties that I've been working with Dr. Dushan Boroyevich, Dr. Fred Wang and Dr. Rolando Burgos. Your challenge gives me a hard time, yet it is turned into a better work. I'm also grateful to my other committee members: Dr. Yilu Liu and Dr. Donald J. Leo.

I'm especially indebted to my colleagues: Mr. Fredric Lacaux, who initiated the mathematical averaging methodology for nine-phase diode rectifier in CPES, Mr. Alexander Uan-zo-li and Mr. Arman Roshan, who collaborated immensely on the experimental prototypes, Mr. Sebastian Rosado, Mr. Carl, Mr. Jerry Francis, Mr. Bin Huang and Mr. Callaway Cass. It was a pleasure to work with those talent and hard-working people.

I would also like to acknowledge the administrative and lab management staff in the Center of Power Electronics Systems (CPES): Ms. Marianne Hawthorne, Mr. Robert Martin, Ms.Teresa Shaw, Ms. Linda Gallagher, Ms. Trish Rose, Mr. Jamie Evans, Ms. Elizabeth Tranter and Ms. Michelle Czamanske, for their instant help in my CPES work.

The friendship in CPES has made my stay more pleasant and enjoyable. Special thanks are given to: Dr. Jinghai Zhou, Dr. Yuancheng Ren, Dr. Shuo Wang, Dr. Bin Zhang, Dr. Lingying Zhao, Dr. Xin Zhang, Mr. Bing Lu, Ms. Yan Jiang, Ms. Jing Xu, Ms Yan Liang, Mr. Meng Yu, Dr. Yang Qiu, Dr. Qian Liu, Mr. Yan Dong, Mr. Dianbo Fu, Ms. Michele Lim, Mr. Wenduo Liu, Mr. Wei Shen, Mr. Hongfang Wang, Dr. Xigen

Zhou, Ms. Ning Zhu, Dr. Qun Zhao, Dr. Zhengxue Xu, Dr. Bo Yang, Dr. Jinghong Guo, Dr. Kaiwei Yao, Mr. Chuanyun Wang, Ms. Li Ma, Ms. Manjing Xie, Ms. Chunping Song and Ms Juanjuan Sun. I appreciate the help from you and will cherish our friendship life long.

With much love, I would like to thank to my husband, Mr. Xiaofeng Bao, who has always been there with love and encouragement.

My appreciation goes toward my parents. Although you are thousands of miles away, you gave me the most valuable strength and courage to go through this journey.

There are some friends outside of the CPES who made my life in Blacksburg more pleasant. You may never realize the value of your help to me.

This work was conducted with the use of Saber, donated in kind by Synopsys of the CPES Industrial Consortium. Also, this work made use of ERC shared facilities supported by the National Science Foundation under Award Number EEC-9731677.

TO MY PARENTS

GUOLIANG ZHU

XUEMEI SHI

AND MY HUSBAND

XIAOFENG BAO

TABLE OF CONTENTS

ABSTRACT ..... **ii**

ACKNOWLEDGEMENT ..... **iv**

TABLE OF CONTENTS ..... **vii**

LIST OF FIGURES ..... **xiii**

LIST OF TABLES ..... **xvi**

CHAPTER 1 INTRODUCTION **1**

1.1 Dissertation Background 1

1.1.1 Average model of power converters in aircraft power system 1

1.1.2 Average model applications 4

1.2 Literature Review 7

1.2.1 More Electric Aircraft (MEA) 7

1.2.2 Ac-dc converters in MEA 8

1.2.3 Average modeling of ac-dc converters 9

1.2.4 System harmonics resonance study 12

1.2.5 Optimization 13

1.3 Dissertation outline 14

CHAPTER 2 OVERVIEW OF AVERAGE MODEL FOR DIODE RECTIFIER 16

2.1. Introduction 16

2.2. Line-commutated three-phase diode rectifier 17

2.3. Average model of diode rectifier 19

2.3.1. Transfer function method 20

2.3.2. Mathematical derivation 21

2.3.3. Method comparison 24

2.4. Summary 25

CHAPTER 3 IMPROVED DYNAMIC AVERAGE MODEL OF DIODE RECTIFIER 27

3.1. Introduction 27

3.2. Operation principle of nine-phase diode rectifier 28

3.3. Assumptions 30

3.3.1. Input voltage source 30

3.3.2. Transformer and rectifier 31

3.3.3. Commutation angle 32

3.4. Improved dynamic average model of three-phase diode rectifier 33

3.4.1. Line current and commutation angle μ 34

3.4.2. Averaged dc output voltage and current 37

3.4.3. Averaged ac currents 38

3.5. Improved dynamic average model of nine-phase diode rectifier 40

3.5.1. Commutation and conduction for nine-phase diode rectifier 41

3.5.2. Commutation inductance of nine-phase diode rectifier 42

3.5.3. Average model of nine-phase diode rectifier 45

3.5.3.1. Line current and averaged dc voltage 45

3.5.3.2. Averaged ac currents 46

3.6. Discussion of average model 50

3.7. Simulation result 52

3.8. Summary 54

CHAPTER 4 TIME DOMAIN EVALUATION OF AVERAGE MODEL FOR DIODE RECTIFIER…..... 55

4.1. Introduction 55

4.2. Overview of different average models 56

4.2.1. Static model 56

4.2.2. Dynamic model 58

4.3. Switching model 60

4.4. Time domain evaluation 62

4.4.1. Definition of evaluation method 62

4.4.2. Steady state evaluation 64

4.4.3. Transient evaluation 69

4.5. Experimental validation 74

4.6. Summary 77

CHAPTER 5 FREQUENCY DOMAIN ANALYSIS OF AVERAGE MODEL FOR DIODE RECTIFIER… 79

5.1. Introduction 79

5.2 Output impedance for nine-phase diode rectifier 80

5.2.1 Output impedances from different average models 80

5.2.2 Output impedances with feeder's impedance 85

5.2.3 Output impedances with generator's impedance 87

5.3 Frequency domain analysis of the average and linearized models 88

5.3.1 Averaging theory for PWM converters 88

5.3.2 Averaging theory for line-commutated diode rectifier 92

5.4 Experiment for output impedance 97

5.5 Summary 98

CHAPTER 6 SYSTEM HARMONIC RESONANCE STUDY 99

6.1 Introduction 99

6.2 System modeling for resonance study 101

6.2.1 Overview of previous research 101

6.2.2 System modeling 102

6.2.3 Norton's equivalent circuit for motor drive 103

6.2.3.1 PWM and motor drive model 103

6.2.3.2 Norton's equivalent circuit derivation 104

6.2.3.3 Norton's equivalent circuit verification 108

6.2.4 Thevenin's equivalent circuit for diode rectifier and generator 111

6.2.4.1 Generator and nine-phase diode rectifier model 111

6.2.4.2 Thevenin's equivalent circuit derivation 112

6.2.4.3 Thevenin's equivalent circuit verification 113

6.3 Resonance study 118

6.3.1 Relationship between resonance and stability 119

6.3.2 Bandwidth of VSI-MD on system resonance 124

6.3.3 Generator's dynamics on system resonance 127

6.4 System simulation 129

6.5 Summary 132

CHAPTER 7 SYSTEM OPTIMIZATION 133

7.1 Introduction 133

7.2 System modeling 134

7.2.1 Switching power amplifier 135

7.2.2 PZT actuator model 139

7.3 Circuit optimization 140

7.3.1 Objective function 141

7.3.2 Design variables 142

7.3.3 Constraints 145

7.3.4 Optimization result 146

7.4 System optimization 148

7.4.1 Objective function 148

7.4.2 Design variables 149

7.4.3 Constraints 150

7.4.4 Optimization result 151

7.5 Summary 154

CHAPTER 8 SUMMARY AND FUTURE WORK 155

8.1 Summary 155

8.2 Future Work 159

8.2.1 Average modeling of diode rectifier 159

8.2.2 System resonance study 159

8.2.3 System Optimization 160

REFERENCE 161

VITA 177

LIST OF FIGURES

Figure 2-1 3-phase line-commutated diode rectifier....18
Figure 2-2 Operation of 3-phase diode rectifier....18
Figure 2-3 AC line current....19
Figure 2-4 Transfer function method....20
Figure 2-5 Average model derived by transfer function method....21
Figure 3-1 Schematic of 18-pulse nine phase diode rectifier....28
Figure 3-2 Nine-phase autotransformer diagram....29
Figure 3-3 I-V curve of diode rectifier....32
Figure 3-4 Nine-phase diode rectifier....33
Figure 3-5 Line current comparison with and without R_c and dynamics....36
Figure 3-6 Commutation and conduction period of nine-phase diode rectifier....42
Figure 3-7 DC output voltage vs. Commutation angle....51
Figure 3-8 Simulation result....53
Figure 4-1 Definition of average current....60
Figure 4-2 Magnetic model of autotransformer....61
Figure 4-3 Interpolation method....63
Figure 4-4 DC output voltage under different conditions @ steady state....65
Figure 4-5 Quantified comparison result for dc output voltage @ steady state....66
Figure 4-6 AC line current for the nine-phase diode rectifier @ steady state....67
Figure 4-7 Quantified comparison result for ac currents in *dq*-axes @ steady state....68
Figure 4-8 DC output voltage @ transient....70
Figure 4-9 Ac line current for nine-phase diode rectifier @ full load to half load....70
Figure 4-10 Approximation effect of the secondary inductance of autotransformer....72
Figure 4-11 Quantified comparison result for dc output voltage @ full load to half load 72
Figure 4-12 Quantified comparison result for ac currents in *dq*-axes @ transient....73
Figure 4-13 Prototype of the nine-phase diode rectifier....74
Figure 4-14 Hardware v.s. Improved model @ steady state....75

Figure 4-15 Winding current for one leg 76
Figure 4-16 Hardware vs. Improved model @ transient 77
Figure 5-1 Output impedance from the average model 82
Figure 5-2 Output impedance including output filter 83
Figure 5-3 Output impedance of nine-phase diode rectifier 84
Figure 5-4 System schematic to measure the output impedance 86
Figure 5-5 Comparison of output impedance of diode rectifier with filter 86
Figure 5-6 Buck circuit 90
Figure 5-7 Fourier analysis of V_{sw} 94
Figure 5-8 Fourier analysis for three-phase and nine-phase diode rectifier 95
Figure 5-9 Influence of commutation inductance and load current on sampling issue 96
Figure 5-10 Measurement of output impedance (nine-phase diode rectifier with output filter) 97
Figure 5-11 Output impedance comparison (nine-phase diode rectifier with output filter) 97
Figure 6-1 Typical rectifier-inverter power system 101
Figure 6-2 Simplified aircraft power system 102
Figure 6-3 Equivalent circuit of the system for resonance study 103
Figure 6-4 Inverter and motor drive model 103
Figure 6-5 Average model of VSI-MD 104
Figure 6-6 Control block diagram 106
Figure 6-7 Input impedance of VSI-MD 106
Figure 6-8 Verification of Y_{in} 108
Figure 6-9 Verification result of Y_{in} 109
Figure 6-10 Verification of I_{in} 109
Figure 6-11 Verification result of I_{in} 110
Figure 6-12 Generator controller 111
Figure 6-13 Generator and rectifier model 112
Figure 6-14 Output impedance of generator and rectifier with output filter inductor 113
Figure 6-15 Verification of Z_{eq} 114
Figure 6-16 Verification result of Z_{eq} 115

Figure 6-17 Generator vs. Voltage source 116
Figure 6-18 Verification of V_d 117
Figure 6-19 Verification result of V_d 117
Figure 6-20 Verification result of V_d 118
Figure 6-21 Simple linear system schematic 120
Figure 6-22 Gain of V_{C0}/V_{in} 120
Figure 6-23 Stability study of Z_s and Z_{load} 121
Figure 6-24 DC power system with two-port network 122
Figure 6-25 Impedance definition of rectifier-inverter system 123
Figure 6-26 Impedance of VSI-MD variation with control bandwidth 125
Figure 6-27 Bode plot of V_{C0}/V_d with different Z_{in} 125
Figure 6-28 Control Bandwidth influence on resonance 126
Figure 6-29 Control Bandwidth influence on stability 127
Figure 6-30 Generator open-loop transfer function V_{rms}/V_{ex} 128
Figure 6-31 Generator close-loop output impedance 128
Figure 6-32 Generator controller's influence on the resonance 129
Figure 6-33 Transfer functions of entire system 130
Figure 6-34 DC bus voltage V_{C0} under different conditions 131
Figure 7-1 Optimization system 134
Figure 7-2 Power amplifier circuit topology 136
Figure 7-3 Control loop for flyback converter 136
Figure 7-4 Average model of half-bridge circuit 137
Figure 7-5 Half-bridge circuit with controller 138
Figure 7-6 Average model of half-bridge circuit 138
Figure 7-7 Recurve actuator 139
Figure 7-8 System model in Simulink 140
Figure 7-9 Correction factor for R_{sa} 144
Figure 7-10 Pareto-optimal curve: trade-off between P_{loss} and Q_e 152
Figure 7-11 Switching frequency vs. α 153
Figure 7-12 Reactive components values. vs. α 153

LIST OF TABLES

Table 3-1 Simulation parameters 52

Table 4-1 Hardware system parameters 75

Table 6-1 Filter parameters for simple linear system 120

Table 7-1 Design variables of circuit optimization 144

Table 7-2 Circuit optimization result 147

Table 7-3 Design variables for actuator 150

CHAPTER 1 INTRODUCTION

1.1 Dissertation Background

1.1.1 Average model of power converters in aircraft power system

The work in this dissertation is based on the next generation of the aircraft power system. Aircraft transportation capability has been increasing dramatically since the 1960s. The traditional aircraft subsystem is powered by a combination of electrical, hydraulic, mechanical and pneumatic means. When power requirements and complexity grow, this system becomes large, heavy and difficult to maintain [1-4].

The concept of the "More Electric Aircraft" (MEA) has been proposed to solve this problem since 1990s. The ultimate objective of the MEA is to completely replace the non-electrical power in the aircraft with electricity. This idea was first applied to meet the military requirement for less overall weight of the aircraft, lower maintenance costs, higher reliability and better performance. With increasing capacity of civil aircrafts, it has been also applied into civil aircraft power systems [2].

The fast development of power electronics makes it feasible to transmit the energy to the load electrically. Power electronics is used throughout the entire system, including power generation, power transmission, environmental control, etc. In the future, it will be also utilized to replace the traditional circuit breakers [3].

The trend for building such a complex aircraft power system is to manufacture components from different vendors and then to synthesize these components. This can reduce the design cost and shorten the design cycle. However, the success of the system integration cannot be guaranteed. Simulation is then necessary for system-level study before the integration of the hardware components.

Because of power switches, it is usually difficult and sometimes even impossible to simulate the entire system using the physical model of each component. The simulation step for power switching devices must be chosen to be very small, typically in milliseconds. However, the transient of the system usually lasts hundreds of milliseconds. A huge amount of time is consumed and the convergence is a big problem. Furthermore, the switching action of power devices causes the system to be discontinuous and non-linear, which prohibits using classical control theory for system analysis. For instance, aircraft power systems always have many motor drives as the loads. The motor drive is a constant power load and is a negative resistor in the small-signal sense. Therefore, the system stability is critical. It is convenient to use stability criteria for a dc-distributed power system if the system is linear and time-invariant (LTI). The detailed switching model is not suitable for this condition.

Simulation using average models is much faster than simulation using the switching models. In system-level study, the exact behavior of the power switching devices is not always of concern, which allows the possibility of using the average model for many simulation cases.

Most switching power converters are LTI circuits for every switch configuration. Averaging different circuit topologies within one switching period T provides a way to

eliminate the switching action from the circuit. The average modeling technique then changes a discontinuous system into a continuous system, which forms the basis for developing small-signal model.

The average modeling technique is first applied to dc-dc pulse-width-modulator (PWM) converters, and then is expanded to ac-dc PWM converters. In an aircraft power system, instead of PWM converters, multi-phase diode rectifiers are preferred to convert ac to dc due to their high power capability and reliability. The multiphase diode rectifier is usually composed of a multi-phase transformer, diode rectifier bridges and an output filter. Compared with three-phase diode rectifier, the harmonics in the line current and the output voltage of the multi-phase diode rectifier are much lower.

Averaging the line-commutated diode rectifier is not so straightforward. There is no "switching period" as there is in PWM converters, although the circuit topology changes. During the past decade, much research has been focused on developing the average model for a line-commutated diode rectifier, but mostly for only the three-phase diode rectifier. Meanwhile, the dynamics of the model still need to be improved. A more accurate dynamic average model for a multi-phase diode rectifier is necessary for system study.

Besides the development of the average model, the average model validation is important for model's application, especially in the frequency domain. Assumptions are unavoidable during the modeling process because of the limitations of the averaging technique. Sampling theory has been applied to explain phenomena in a dc-dc PWM converter [57]. The model's evaluation, both in the time domain and in the frequency

domain, is important for proper applications of the model. Such problems have not been investigated before this study.

1.1.2 Average model applications

After obtaining the average model, the next task in this dissertation is to apply the model to system-level study. Two different applications are demonstrated in this work: system harmonic resonance study and system optimization. These two applications are typical system-level studies that cannot be carried out without the average models of the switching power converters.

Resonance occurs when the system nature frequency is equal to the harmonic source frequency in the system. The harmonic source might generate from the nonlinear block in the system, or when the system is under abnormal operating conditions. Many efforts have been made in the past to predict the resonance in power systems and damp it. To predict the resonance, the transfer function from the harmonic source to the voltage or current of the node that is concerned is derived. The system nature frequency and the amplification of the harmonics under each frequency can be obtained from the gain of the transfer function. For systems that have switching power converters, the non-linear blocks are usually modeled by ideal voltage or current sources depending on their characteristics, under the assumption that their internal impedances are small enough to neglect.

This modeling approach is effective under many conditions. Nevertheless, there are some cases in which this assumption does not hold true. For example, in this dissertation, the resonance study is based on a simplified aircraft system, composed of a synchronous

generator, a nine-phase diode rectifier, a motor drive and filters. When the filters in this system are designed to be small in order to reduce the size and weight of the aircraft power system, the internal impedance of the switching converter is comparable to the filters and cannot be ignored. Therefore, Thevenin's and Norton's equivalent circuits are proposed to substitute for the non-linear blocks in the system to derive the transfer function, which requires the average models of the switching converters. How to obtain the equivalent circuits is the main goal of this research.

In most resonance studies, the relationship between stability and resonance is not clearly stated. Additionally, the parameter sensitivity to the system resonance needs to be investigated to provide design guidance. All of these are questions that should be answered during resonance study.

Another application of average models is optimization. System optimization has been proposed for the aircraft power system because the weight and size are critical. Traditional design depends mainly on engineers' experience, which may result in a sub-optimal design. Furthermore, because of the interaction between the load and the circuit, the traditional design approach is highly compartmentalized and sequential. Mathematical optimization has emerged recently as an integration platform to design the system in an organized and methodical way. It allows the designer to potentially use a large number of design variables and to generate the design automatically.

The example system for optimization used in this dissertation is a switching amplifier with an actuator as its load. The multi-phase diode rectifier is not chosen because the optimization of the transformer has already been studied and is easily applied to the multi-phase diode rectifier [90]. Moreover, in the aircraft system, the interaction between

the converter and the load is of high interest, while the diode rectifier has little interaction with the load and only provides the dc bus voltage.

In contrast, the actuator and its driving amplifier have close interaction in the aircraft system. Actuators employing smart materials have attracted substantial attention in the past decade because of their high power density. Piezoelectric (PZT) and electrostrictive materials are two smart materials that change their shapes in response to an electric field. For smart structure applications where the frequency is above 5Hz, piezoelectric material is usually used due to its ability to use in a high operating frequency range [86], which is the case in the work here.

The capacitive characteristic of the PZT actuator brings the challenge of the design of driving amplifiers. Although the actuator consumes almost no real power, a considerable amount of reactive power circulates between the actuator and the amplifier. A standard linear amplifier dissipates the regenerated energy into heat, which then requires a bulky and heavy heat sink. In contrast, a switching power amplifier can recycle the regenerative energy back to the source, resulting in a small, light and efficient amplifier. In [87], the comparison of linear and switching drive amplifiers is presented, given the conclusion that the linear amplifier consumes more power than the switching amplifier.

The optimization is applied to the switching power converter and the PZT actuator. Accurate models of each component are necessary for the optimization. In order to be executable with commercial optimization software, the switching power converter must be described with mathematical equations, which come from the average models.

In summary, this dissertation is focused on the average models of switching converters and their applications in system-level study.

1.2 Literature Review

1.2.1 More Electric Aircraft (MEA)

Electricity was first used in the aircraft power system for ignition, which only required hundreds of watts. Within one century, the electricity has exceeded over megawatts [1, 2]. Due to fast-increasing requirement, the concept of the MEA is proposed to reduce the weight and size of the aircraft.

Power generation and distribution in the aircraft system has changed significantly in order to reduce the weight and size of the system. The dc power system was used at the beginning of aircraft design. The dc voltage changed from 14.25V to 28V in 20 years. Later, a 115/200V, 400Hz ac system was selected to have a lighter system. This ac system is still in wide use today [1-8].

There are three main methods to generate ac systems: a constant speed drive (CSD), a variable speed constant frequency (VSCF) system and a dc-link system. The latter two systems have variable frequencies out of the generators, and the fixed frequency for the system is provided through switching power converters. The advantage of these two systems is that they provide a better starter/generator system without mechanical parts [8].

Other system architectures are also of interest. One such architecture was introduced in the 1980s, when a 270V dc power system was proposed by NASA to reduce the wire weight. This power system has been applied on some military aircrafts.

The variable frequency system is very cost-effective and is becoming widely used on business jets [5]. The generator's efficiency during the entire frequency range and the power quality are major concerns in such a system.

Among these architectures, the variable frequency generator is promising for future designs. Therefore, the variable frequency system becomes the major concern in this dissertation.

1.2.2 Ac-dc converters in MEA

The development of power electronics makes the MEA feasible. The key achievement of power electronics in terms of designing the MEA is the increase in power density obtained by power semiconductors, which is applied from the power generation to power distribution and utilization. For example, various types of power converters generate multi-level voltages in the aircraft power system for different usage. The loads in the MEA also require lots of motor drives and dc-dc converters [13-16].

In an MEA, power converters must meet the system harmonic requirements, especially the converters that connect the generators and the dc buses [17]. Either active or passive rectifiers can be used as front-end converters for aircraft power systems. Multi-phase diode rectifiers are passive converters, which are based on multi-phase transformers. In [18] and [19], comprehensive comparisons between a twelve-pulse diode rectifier and an active PWM converter are presented. Compared with active rectifiers, transformer unit rectifiers (TRU) are simpler, more reliable and more efficient. A conventional TRU is an unregulated device, but its output voltage can be controlled by adding controllers into the system (RTRU) [20, 21], which is beyond the scope of the dissertation.

In a current MEA, there are two main types of passive ac-dc converters: six-phase (twelve-pulse) diode rectifiers and nine-phase (eighteen-pulse) diode rectifiers. The six-

phase diode rectifier usually provides the 28V dc voltage in the aircraft power system. In [22], one such low-weight, low-cost rectifier is developed. Obviously, the harmonics become lower when the number of rectification pulses increases, and the nine-phase diode rectifier is proposed. An autotransformer, instead of a transformer, is used before the diode rectifier bridge. Different autotransformer topologies are compared in [23] in terms of weight, power rating, and efficiency. In [24], the harmonics influenced by the autotransformer is discussed. A detailed analysis of a nine-phase diode rectifier is given in [25]. With these converters, the aircraft power system has different levels of dc voltage for the power distribution system.

1.2.3 Average modeling of ac-dc converters

System simulation involving switches is not an easy task [26, 27]. For easier analysis and faster simulation, a multi-level modeling approach is proposed to meet the modeling guidelines [28]. Switching models are only necessary when switching ripples are of interest or detailed transient information is needed. Otherwise, average models provide enough information at a low frequency range [29, 30]. Meanwhile, average models change the discontinuous system into the continuous system, which are the basis of small-signal models to use classical control theory [31].

The average modeling technique for modeling switching power converters has been studied since the 1970s. The state-space averaging method was first proposed for PWM dc-dc converters in [32]. For each switching configuration (ON or OFF), the circuit is linear. The state-space averaging method is to average the two circuits within one switching period. This method is useful but is limited. A generalized averaging method

refines the state-space averaging method using Fourier series expansion [33, 34]. Fourier coefficients other than that of the fundamental frequency are taken into account. Using this method, the ripples can be recovered in the average model. This method is applied also in multi-converter systems to simulate the dc power system [35, 36].

In a three-phase ac-dc system, the state-space averaging method can be applied to PWM converters with the Park transformation [37]. However, the average model of the three-phase diode rectifier cannot be derived directly by this method. The operating principle of the diode rectifier is given in [38]. The circuit topology changes during the commutation and conduction periods. In reference [41], based on the fundamental averaging theory, the average model of the line-commutated three-phase diode rectifier with an ideal input voltage source is derived by averaging the dc output voltage within 60°. In [42], the generator's equations are combined into the average model of the rectifier when the subtransient impedances of the generator in *d,q*-axes are not the same. This model is the static model, which assumes that the load current stays constant. When the load current is assumed to change during one switching period, another average model is developed, which is explained in [43]. This is defined as a dynamic average model of the diode rectifier. In [44], it is pointed out that the commutation angle is only related to the average current during the commutation period. The average model is then completely re-derived using other forms of mathematical expression.

The static model of the three-phase diode rectifier in [41] is expanded to a six-phase diode rectifier in [45]. Reference [46] gives the equivalent circuit for a six-phase diode rectifier when there is line inductance before the transformer. Reference [47] presents the

static average model when the generator is modeled together with the six-phase diode rectifier.

All the above average models for diode rectifiers are derived using mathematics. Another approach for deriving models is to treat the diode rectifier as a black box and get its input-output voltage and current relationships. This has been successfully applied to a three-phase and multi-phase diode rectifier [48-50]. The impedance characteristic of a six-phase synchronous generator-rectifier system is obtained via this method [51].

The nine-phase diode rectifier is applied in the aircraft power system, which also needs the multi-level modeling approach [52]. In [53], the quasi-stationary small-signal model of a nine-phase diode rectifier is developed, which is used to predict the system stability.

The validation of the average model is of great concern. Reference [56] makes the points that the small signal models of PWM converters are not valid after half of the switching period, due to the sampling theory [56]. The sampled-data model improves the model's accuracy by combining discrete modeling techniques [57]. In [58], the average model is improved by modeling the sampling block using a transfer function. However, it is still limited to the same frequency range [59]. Reference [60] describes the approximation and validation of the average model in detail using mathematics. Documentation of such investigation does not exist for average models of line-commutated diode rectifiers.

Average models can include harmonic distortion, as presented in [54, 55], which is beyond the scope of this work.

1.2.4 System harmonics resonance study

Harmonic study is discussed intensively in industrial power systems [66-73]. The existence of a nonlinear load or an unbalanced component brings more harmonics into the system. There are two resonant conditions: series resonance and parallel resonance. In [67], the measurement of hardware for harmonics study is given however, it is better to use system models to predict the harmonics before it occurs. System modeling for harmonic studies needs to be accurate, but also needs to result in models that are not too complicated. It is pointed out in [68] that the harmonic source should be modeled using Norton's or Thevenin's equivalent circuits. The nonlinear load is classified into two types of harmonic source: Current Source Nonlinear Load (CSNL) or Voltage Source Nonlinear Load (VSNL) [69]. The CSNL can be modeled as the Norton's equivalent circuit, while the VSNL should be modeled as the Thevenin's equivalent circuit. In [70-72], Thevenin's equivalent circuit is used to predict the resonance in an ac power system. Reference [73] studies when harmonics might occur due to an unbalanced input voltage. Various damping methods are proposed for an ac power system [75-77].

However, there are not many studies on resonance for dc power distribution systems. In [78] and [79], the harmonics resonance is studied in a railway system, which is quite similar to an aircraft system. The transfer function is derived from the harmonics to the bus capacitor by modeling the harmonic sources as ideal current sources. Impedance modeling is proposed in [80] based on a numerical-linearization technique. It shows that impedance at low frequency will influence the resonance, but this method requires a great deal of computation.

1.2.5 Optimization

System optimization is proven to be effective in reducing the weight and size of the aircraft system [88]. The optimization for the actuator and the electronics circuit was performed separately in the past. An overview of optimization for the piezoelectric actuator and its electronics circuit is given in [91]. There are many papers for actuator optimizations, while the number of papers on the optimization for the driving circuit is limited.

Nonetheless, there is some literature on optimization in power electronics in the past [92-99]. Early efforts focus on strictly continuous optimization [92-97], which means all design variables are continuous variables. Different objective functions were selected, such as the weight of the inductor or the power dissipation in the circuit. Continuous optimization can result in a better design than the traditional design, but it has two shortcomings: 1) the switch selection for drive amplifier cannot be handled and 2) the optimal result must be round to the off-the-shelf components, which will degrade the effect of optimization.

More recent work has employed genetic algorithms as discrete optimizers for device selection, using cost to be the objective function [95, 96]. Genetic algorithms (GA) are probability-based algorithms that utilize the process of natural selection, and have been experimentally proven to be robust in their application to many research problems [100].

1.3 Dissertation outline

The dissertation includes two main parts: the average model development of line-commutated diode rectifiers (Chapter 2 to Chapter 5) and the application of average models in system-level study (Chapter 6 and 7).

Chapter 2 gives a detailed overview of the existing average models for line-commutated diode rectifiers. Two different modeling approaches are introduced and compared. This comparison determines the choice of the modeling approach for a multi-phase diode rectifier in a variable frequency system in this work.

In Chapter 3, new average models of three-phase and nine-phase diode rectifiers with improved dynamics are developed. The derivations for average models of three-phase and nine-phase diode rectifiers are very similar. Therefore, the detailed derivation is described based on three-phase diode rectifiers for simplicity. For nine-phase diode rectifiers, the difference when considering the feeder's inductance before the transformer is stressed due to the existence of the autotransformer. The limitation of the average model is presented at the end of this chapter.

The time domain evaluation of new average models of three-phase and nine-phase diode rectifiers is given in Chapter 4. The three average models, the static model, original dynamic model and new improved dynamic model, are developed in MATLAB/Simulink and are compared to the detailed switching model in Saber. Interpolation is utilized in order to give quantized comparison results. The models are compared under both steady state and transient conditions. The experimental validation of the improved dynamic average model is also given in Chapter 4.

In Chapter 5, output impedances of nine-phase diode rectifiers are derived based on different average models for system-level study. When a generator is considered instead of an ideal voltage source, the influence of the generator output impedance is discussed, which provides useful information for Chapter 6. Another topic in Chapter 5 is the frequency validation of the average model. The sampling effect in the average model is given by simulation result.

The average model is applied into system harmonic resonance study in Chapter 6. The system consists of a generator, a nine-phase diode rectifier and a motor drive. The average models replace the switching power converter, including the rectifier and the inverter for the motor drive. Norton's and Thevenin's equivalent circuits are developed for system linearization. Transfer functions are derived in this chapter to predict the resonance and the controller influence of the motor drive and generator on system resonance is given according to the simulation result. Some issues of resonance, such as the relationship between the resonance and stability, are presented.

Chapter 7 gives the optimization of an electronics circuit with a piezoelectric actuator as its load. The average model must be used with commercial optimization software. The genetic algorithm is selected as the optimization algorithm. The objective function, design variables and constraints are given for the circuit and the system optimization.

Conclusions and possible future research work are presented in Chapter 8.

CHAPTER 2 OVERVIEW OF AVERAGE MODEL FOR DIODE RECTIFIER

2.1. Introduction

Line-commutated diode rectifiers are often applied to ac-dc power systems with constant power loads. Because of the negative resistance characteristic of the constant power load in the small-signal sense, the system stability becomes a critical issue in such a system. It is convenient and valuable to use the classical linear time-invariant (LTI) control theory for linear system stability study. However, since the switching model of the diode rectifier is discrete and non-linear, it is impossible to use the LTI theory directly. An average model is then required as the first step to eliminate higher-order harmonics in the waveforms by calculating the average value during one switching interval. During this switching interval, the high-frequency switching content is averaged out. This averaging function is sometimes referred to as the "moving average" or "fast average". Assuming that T is the switching period, this function can be written as $\bar{x} = \frac{1}{T} \cdot \int_{t}^{t-T} x(t) \cdot dt$, where x are the state variables [39].

Furthermore, using the average model, the simulation time will be much less than the simulation time using the switching model because there is no longer any switching action. The average model also provides a basis to derive a small-signal model with perturbation and linearization.

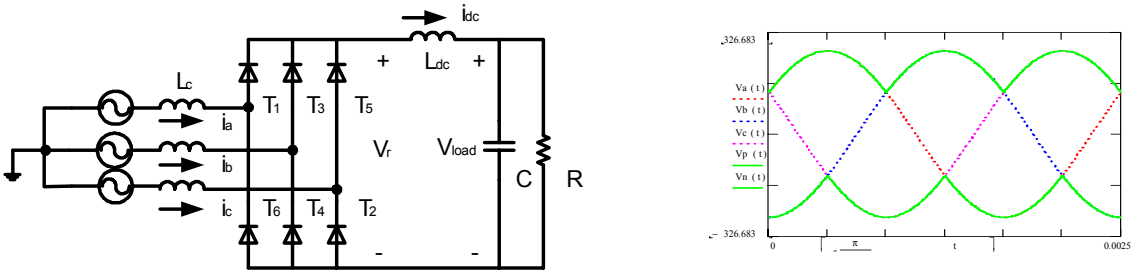
The average modeling technique has been studied for dc-dc PWM converters for over 30 years [56-60]. The state-space averaging method is now widely used in the modeling work of dc-dc PWM converters by replacing switches with dependent voltage and current sources. This method has been extended to ac-dc PWM converters [37].

The average model for the line-commutated diode rectifier cannot be derived in the same way. Although the circuit topology changes within one switching period, the switches cannot be substituted by single-pole-double-throw switches, which prohibit replacing the switches by dependent sources. Instead, the state variables in the rectifier are averaged directly. The output dc voltage and input ac currents in *dq*-axes are chosen as the state variables in the rectifier.

There are two existing averaging methods [42, 48] to derive the average model for a three-phase line-commutated diode rectifier, denoted as the transfer function method and the mathematical derivation method. Both methods use the moving average theory but each with a different approach. In this chapter, the detailed modeling approaches are introduced and compared.

2.2. Line-commutated three-phase diode rectifier

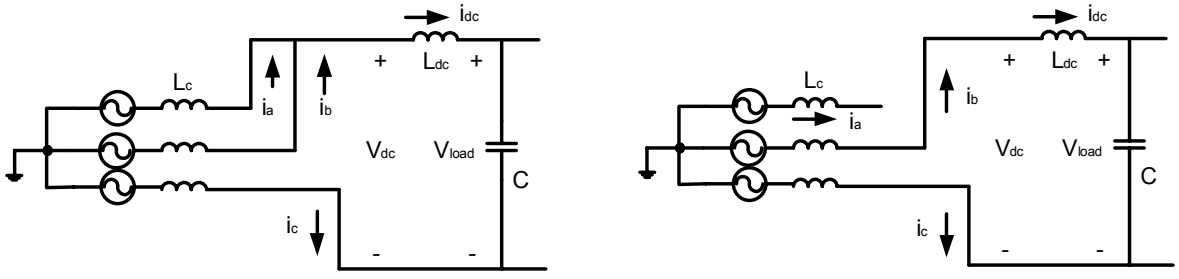
A three-phase diode rectifier can convert alternating current into direct current. The circuit topology of a line-commutated three-phase diode rectifier is shown in Figure 2-1(a) and the voltage waveforms are given in Figure 2-1 (b).



(a) three-phase diode rectifier **(b) voltage waveforms**

Figure 2-1 3-phase line-commutated diode rectifier

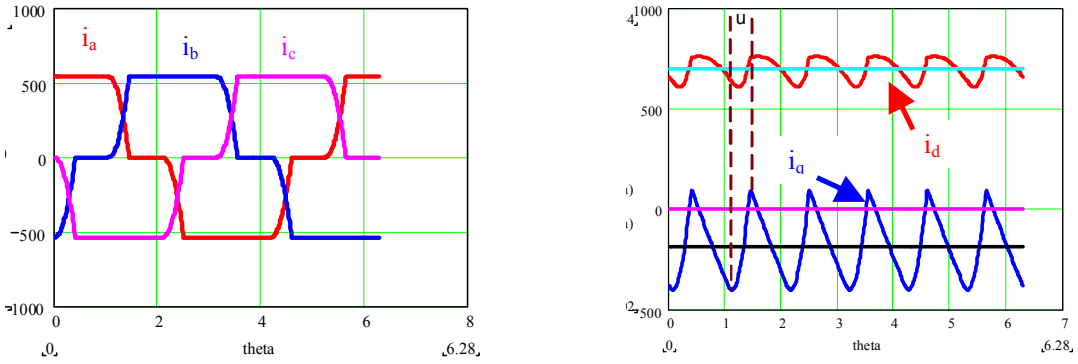
According to the diode characteristics, the ac line current will be switched from one diode bridge to another at six times the line frequency. The current transfer cannot be completed instantaneously when line-commutating inductance L_c exists. For example, at $\pi/3$ in Figure 2-1(b), current will transfer from i_a to i_b, while i_c conducts full current i_{dc}. There are three diodes conducting current T_1, T_2, and T_3 till i_a is equal to i_{dc} and the current transfer is completed. This period is defined as the commutation period. After the commutation period, only two diodes conduct current (i_b and i_c for this case), T_2 and T_3, till another current transfer begins. This is defined as the conduction period. The circuit topology will change between the commutation and conduction period. Figure 2-2 gives operation models in the commutation and conduction periods of every switching period.



(a) commutation period **(b) conduction period**

Figure 2-2 Operation of 3-phase diode rectifier

The symmetrical structure of the diode rectifier leads to the periodical waveform of the output dc voltage V_{dc} with a frequency that is six times the line frequency. Since commutation also occurs at this frequency, it is denoted as the switching frequency f_{sw} for the three-phase diode rectifier. Although the ac line currents' frequency is equal to the line frequency, their expression in *dq*-axes using the Park transformation has the same switching frequency as f_{sw}, shown in Figure 2-3.



(a) in abc-axes **(b) in dq-axes**

Figure 2-3 AC line current

2.3. Average model of diode rectifier

The derivation of the average model for a three-phase diode rectifier has been proposed in [41-44, 48-49], which can be categorized in two methods: the transfer function method and the mathematical derivation method. Both methods average the state variables of the rectifier within one switching period.

2.3.1. Transfer function method

The transfer function method was proposed for deriving the average model for a three-phase generator-rectifier with generator in [48]. The transfer function between the output and input of the rectifier is found using a black box approach, as in Figure 2-4.

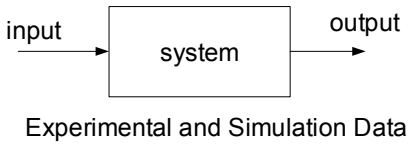


Figure 2-4 Transfer function method

For each operating point, the relationship of the magnitude between the input and the output vector is calculated. The input and output data are obtained either from hardware experiments or from detailed simulation results. The magnitudes of the generator's output voltage and current in the *dq*-axes at the fundamental frequency are assumed to be proportional to the dc components of the rectifier output voltage and current. The average model is shown Figure 2-5. δ is the angle between the generator output voltage in *d,q*-axes V_d and V_q. The angle between the generator output current in the *dq*-axes I_d and I_q are denoted as α. For each operating point, δ can be calculated by $tg^{-1}(V_q/V_d)$. The coefficient k_v is the ratio between the magnitude of the rectifier output voltage V_{dc} and its input voltage V_d, V_q, δ. The ac currents I_d and I_q can be modeled using the dc current I_{dc}, the magnitude ratio k_i and phase α. To develop the average model, the value of coefficients k_v, k_i and α should be determined using the switching model.

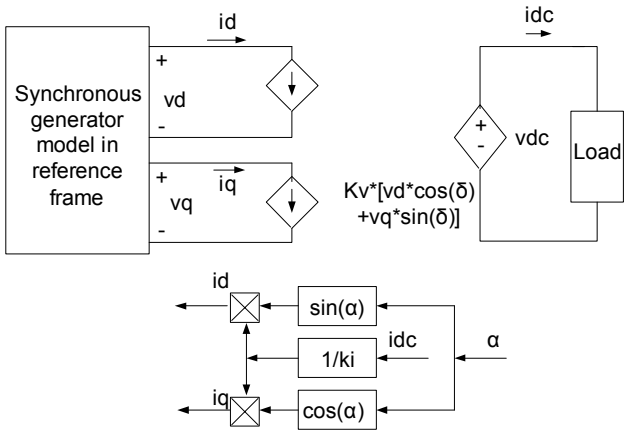


Figure 2-5 Average model derived by transfer function method

This method has been extended for the multi-phase transformer rectifier unit in [50]. Curve fitting of k_v, k_i and α is utilized to create an average model of the circuit in a certain range. The averaged model is almost the same as the model in Figure 2-5 except that the synchronous reference frame is used instead of the arbitrary reference frame, which means that V_q is set to zero and there is no δ in the model.

2.3.2. Mathematical derivation

The mathematical derivation method is to derive the differential equations of the circuit during the commutation and the conduction period, which includes both the dc-side output voltage and the ac-side input current. The equations are then averaged within one switching period [41].

The period *(π/3, 2π/3)* is chosen in which the equations will be derived. If the load current i_{dc} is assumed to be constant during one switching period, the static average model is derived. From Figure 2-2, the equations of the circuit during the commutation period is written as

$$2 \cdot L_c \cdot \frac{di_a}{dt} = V_b - V_a \cdot \tag{2-1}$$

Using the boundary condition $i_a(\pi/3)=0$, the line current i_a is expressed as

$$i_a(t) = \frac{\sqrt{3} \cdot V}{2 \cdot \omega \cdot L_c} \cdot (1 - \cos\mu), \tag{2-2}$$

where V is the peak value of the input voltage source, ω is the line frequency in *rad/sec* and μ is the commutation angle. When i_a is equal to i_{dc}, the commutation ends, which means that the commutation angle is

$$\mu = \arccos\left(1 - \frac{2\omega \cdot L_c \cdot i_{dc}}{\sqrt{3} \cdot V}\right) \cdot \tag{2-3}$$

The output voltage is determined by

$$\overline{V_{dc}} = \frac{3 \cdot \sqrt{3}}{\pi} \cdot V - \frac{3 \cdot \omega \cdot L_c}{\pi} \cdot I_d \cdot \tag{2-4}$$

This model has been improved to include dynamics in the circuit. The load current is not assumed to be constant but to change Δi_{dc} during one switching period. The commutation angle for this model is the same as in (2-3). The output voltage is derived by averaging its expressions during the commutation and conduction period, which is

$$\overline{V_{dc}} = \frac{3 \cdot \sqrt{3}}{\pi} \cdot V - \frac{3 \cdot \omega \cdot L_c}{\pi} \cdot I_d - 2 \cdot L_c \cdot \frac{di_{dc}}{dt} \cdot \tag{2-5}$$

The ac currents in the *dq*-axes are derived but Δi_{dc} is ignored. The expressions are

$$\begin{aligned} \overline{i_d} &= \frac{3}{\pi} \cdot \left(\int_{\frac{\pi}{3}}^{\frac{\pi}{3}+\mu} i_{d,com}(t) \cdot dt + \int_{\frac{\pi}{3}+\mu}^{\frac{2\pi}{3}} i_{d,con}(t) \cdot dt \right) = \overline{i_{d,com}} + \overline{i_{d,con}}, \\ \overline{i_q} &= \frac{3}{\pi} \cdot \left(\int_{\frac{\pi}{3}}^{\frac{\pi}{3}+\mu} i_{q,com}(t) \cdot dt + \int_{\frac{\pi}{3}+\mu}^{\frac{2\pi}{3}} i_{q,con}(t) \cdot dt \right) = \overline{i_{q,com}} + \overline{i_{q,con}} \end{aligned} \tag{2-6}$$

where $\overline{i_{d,com}}$, $\overline{i_{q,com}}$ are the input currents during the commutation period in the *dq*-axes, and $\overline{i_{d,con}}$, $\overline{i_{q,con}}$ are input currents during the conduction period. The ac currents could

be obtained by solving the differential equations of the circuit in the three-phase diode rectifier, followed by Park transformations. The detailed derivation procedure can be seen in [41].

The average model using this method has the same topology as in Figure 2-5 except that V_{dc} and I_d, I_q will be expressed by equations.

When the input voltage source is a generator, the commutation inductance should involve the generator's output impedance, which is basically an inductor in series with a resistor. Besides the line inductance, it will also contribute to the commutation period of the diode rectifier.

The generator's output impedance is in the *dq*-axes, but the calculation of the commutation angle is based on the commutation inductance in 3-phase. This brings the challenge of how to match the generator impedance in *dq*-axes into line commutation inductance. Reference [42] gives the average model of a synchronous generator-fed rectifier at steady state. Combing the generator model with the diode rectifier, the flux of the generator is used instead of the voltage magnitude in the averaging process of the diode rectifier. The equivalent line commutation inductance is

$$L_{ss}(\beta)=\frac{1}{2}\cdot\left(L_d''+L_q''\right)+\left(L_d''-L_q''\right)\cdot\sin\left(2\beta+\frac{\pi}{6}\right), \tag{2-7}$$

where L_d'' and L_q'' are subtransient inductances and β is the delay firing angle. For the diode rectifier here, β is zero. The steady state commutation inductance L_{ss} becomes L_d'' in this work.

Reference [43] improves the model to have transient characteristic by assuming the load current change within one switching period. The transient commutating inductance is defined as

$$L_t(\beta) = L_d'' + L_q'' + (L_d'' - L_q'') \cdot \sin\left(2\beta - \frac{\pi}{6}\right) \cdot \quad (2\text{-}8)$$

When β is zero, the transient commutation inductance L_t is equivalent to $0.5 \cdot L_d'' + 1.5 \cdot L_q''$.

In the work above, the generator is expressed with its open-loop subtransient impedance L_d'' and L_q''. This is because the switching actions of the diodes are much faster than the generator's dynamics. Moreover, the close-loop subtransient impedance is almost the same as the open-loop subtransient impedance. Therefore, the open-loop subtransient impedance can represent the generator's behavior for this situation.

2.3.3. Method comparison

The transfer function method and mathematical derivation are both powerful tools for developing the average model of the diode rectifier. They are both based on the assumption that the input voltage source and the line inductances are symmetrical and balanced. Only under this condition, does the circuit have the switching frequency of six times the line frequency and can it be averaged within that period.

Using the transfer function method to derive the average model of the rectifier is easy and straightforward. The transfer function method avoids the complex calculation of the differential equations. Meanwhile, the non-linearity effects of the circuit, such as the saturation of the transformer, could be taken into account when obtaining the parameters. The disadvantage of this method is that the switching model must be simulated under each operating point to obtain the data, and it is time-consuming to build the lookup tables of the coefficients for the average model. Since this method is static by definition, the inclusion and improvement for model dynamics has been proven to a difficult task to

achieve. Moreover, when the line frequency is not constant, curve fitting adds intricateness to frequency identification.

In contrast, the mathematical model is completely unlimited in this sense. The line frequency becomes one of the variables in the expression of the average model, like the input voltage source. The circuit dynamics can be included in the average model. Once the model is developed, it is easy to use under different parameters in the system. Its disadvantage is that the generator and the rectifier have to be modeled as one block, where the generator's dynamics is ignored. The calculation of the commutation inductance becomes complicated when the system has multiple branches in parallel. The non-linearity in the system is also not considered in the derivation.

Since our models are developed specifically for a variable-frequency aircraft power system, the mathematical method is adopted in this work for deriving the average model.

2.4. Summary

The basic operation principle of the three-phase diode rectifier is introduced in this chapter. The switching period of the rectifier is six times the line frequency based on its symmetrical structure. The commutation period is the time period during which current transfers from one branch to another. The development of the average model of the rectifier is to average the output dc voltage and ac currents during the commutation and conduction periods.

The relationship between the input and the output variables can be obtained either by the transfer function method using the switching model simulation result point by point, or by mathematical derivation of the differential equations. Both methods are limited to a

symmetrical and balanced system. Since mathematical derivation is more suitable for a variable-frequency power system, it is chosen as the averaging method in this dissertation.

CHAPTER 3 IMPROVED DYNAMIC AVERAGE MODEL OF DIODE RECTIFIER

3.1. Introduction

The average model of the diode rectifier forms the basis for obtaining the small-signal model, which is a necessity for system stability. In [41], the static and dynamic models of three-phase diode rectifier are derived, as illustrated in Chapter 2 in detail.

The existing dynamic average model for the three-phase diode rectifier takes dynamics into consideration to some extent by assuming that the load current changes within one switching period. However, the load current change is ignored when deriving the commutation angle and ac line currents. In this chapter, the dynamic model of three-phase diode rectifier is improved. The key assumption taken for improved dynamics is to model the load current using its first-order Taylor Series expansion during the complete averaging time span, i.e., during both commutation and conduction periods. This improves both dc voltage and ac current dynamics, since the load current is never assumed constant and expressed in terms of its average value during the commutation period. The resultant improved average model has better accuracy on the system-level study. Additionally, the steady state performance is improved by modeling parasitic resistances, and by using a non-ideal I-V characteristic to model the diodes.

Same modeling approach is applied to a nine-phase diode rectifier to obtain its average model in this chapter. There are two special issues for nine-phase diode

rectifiers. First, it has an autotransformer and the feeder's inductance before the autotransformer needs to be referred to the secondary for equivalent commutation inductance. It cannot be achieved by simply multiplying the feeder's inductance with the turns ratio because of the nonlinearity of the diode rectifier. Second, a nine-phase *dq*-transformation is defined to model the line current. The limitation of the model is discussed at the end of this chapter.

3.2. Operation principle of nine-phase diode rectifier

A multi-phase diode rectifier is often applied in an aircraft power system as a front-end converter. The nine-phase diode rectifier is introduced in this work. It is composed of an autotransformer unit and one nine-phase diode bridge. The topology of this converter is shown in Figure 3-1.

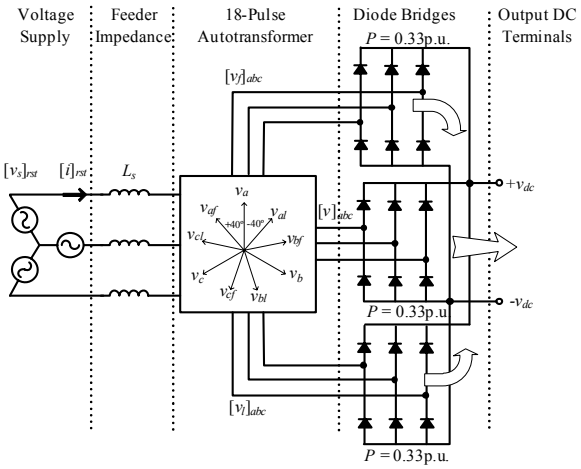


Figure 3-1 Schematic of 18-pulse nine phase diode rectifier

The autotransformer has nine secondary windings that generate three sets of three-phase voltages, denoted as forward, center and lagging voltages, each phase-shifted by

+40º, 0º, and -40º with respect to the primary input voltage source. These voltages feed the three diode bridges in direct connection with their dc terminals. Each diode conducts the full load current for 40º, as opposed to paralleled 18-pulse rectifiers where diodes conduct 1/3 of the load current for 120º. One type of autotransformer phasor diagram is shown in Figure 3-2.

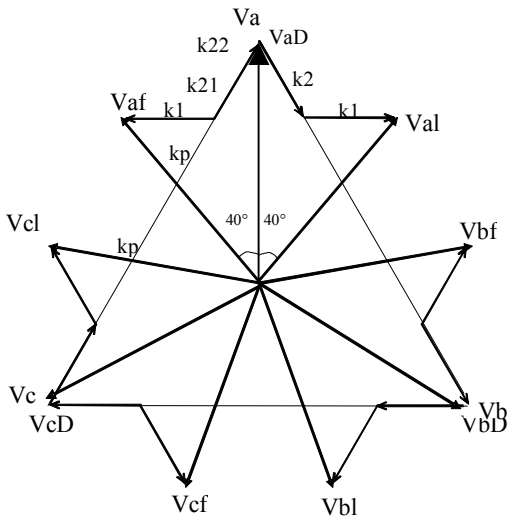


Figure 3-2 Nine-phase autotransformer diagram

The primary-secondary voltage ratio per phase is denoted as n_v and the corresponding secondary-primary current ratio is denoted as n_i. Since each diode bridge will deliver one-third of the total power, the relationship between n_v and n_i becomes

$$n_i = 3 \cdot n_v . \tag{3-1}$$

The voltage ratio n_v can be calculated based on the number of turns in each winding from the vector diagram. **Error! Reference source not found.**

3.3. Assumptions

Assumptions are made in order to derive the mathematical averaged model for three-phase and nine-phase diode rectifiers. Some assumptions are made for the sake of simplicity, while others are necessary for derivation. In this section, all the assumptions will be given prior to derivation.

3.3.1. Input voltage source

The three-phase input voltage source must be symmetrical and balanced, which allows the diode rectifier to have the desired "switching frequency". Given that only the fundamental frequency is considered when doing the averaging, an implicit assumption is that all power transfer occurs at the line frequency.

The input voltage source is

$$\begin{cases} V_a = V \cdot \cos(\omega t + \theta_0) \\ V_b = V \cdot \cos\left(\omega t - \frac{2\pi}{3} + \theta_0\right) \\ V_c = V \cdot \cos\left(\omega t + \frac{2\pi}{3} + \theta_0\right) \end{cases}, \tag{3-2}$$

where V is the amplitude of the voltage source, ω is the line frequency in *rad/sec* and θ_0 is the initial angle. θ_0 can be set arbitrarily for derivation convenience. The voltage source is ideal and has no output impedance.

In order to simplify the derivation, the voltage in the *abc*-axes will be converted to the *d*-axis only using the Park transformation as

$$T_{dq}^{3}=\sqrt{\frac{2}{3}}\cdot\begin{bmatrix}\cos(\theta+\theta_0) & \cos\left(\theta-\frac{2\pi}{3}+\theta_0\right) & \cos\left(\theta+\frac{2\pi}{3}+\theta_0\right)\\ -\sin(\theta+\theta_0) & -\sin\left(\theta-\frac{2\pi}{3}+\theta_0\right) & -\sin\left(\theta+\frac{2\pi}{3}+\theta_0\right)\end{bmatrix}. \tag{3-3}$$

3.3.2. Transformer and rectifier

The nine-phase diode rectifier includes an autotransformer and one nine-phase diode bridge. An *LC* output filter is usually connected with the diode rectifier at the dc output terminal. The average model of this unit is based on the average model of an equivalent nine-phase diode rectifier, given that both the autotransformer and the dc filter are passive components without switching elements.

From Figure 3-2, it shows that the autotransformer impedance is a complex cross-connected set of parallel and series impedances between the three-phase lines. However, the equivalent commutation inductance for each phase is required to average the nine-phase diode bridge within 20º. Fortunately, assuming the simplified equivalent impedance on the secondary side of the autotransformer almost does not cause the loss of useful information when simulating the averaged model. Specifically, the assumptions made in the autotransformer model are:

1. Autotransformer symmetry: the secondary voltage of the autotransformer is the same;
2. Autotransformer leakage impedance: the transformer leakage is modeled by using equal series inductances with each phase;
3. Magnetizing inductance: this inductance is neglected due to its much larger value when compared to the leakage inductances;

4. Nonlinear effects: saturation and hysterisis are not considered for the transformer.

The diodes are modeled by the I-V curve in Figure 3-3. The forward voltage drop V_{on} and on-state resistor R_{on} are considered. The switching behavior of the diodes is assumed to be ideal, which means that they will turn on or off instantaneously.

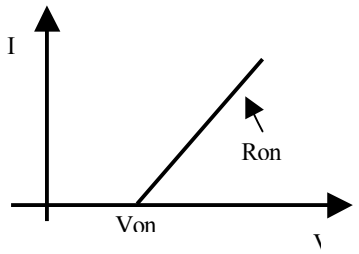
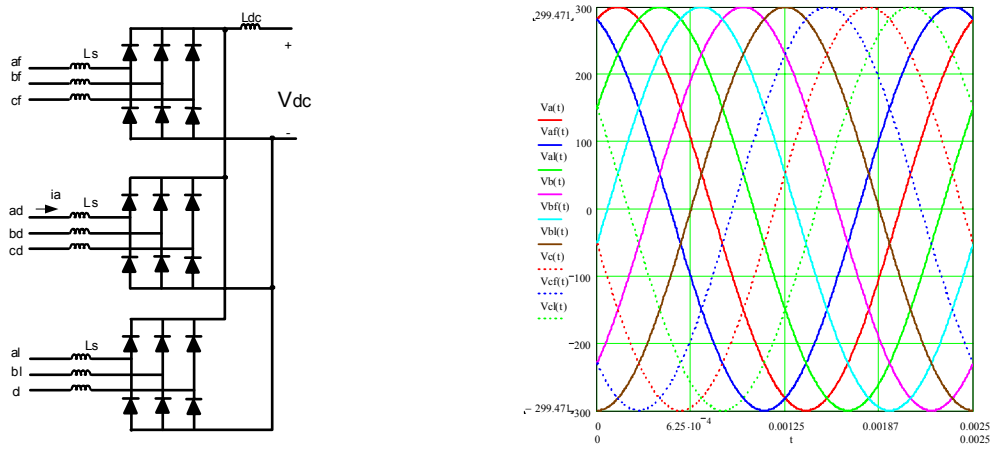


Figure 3-3 I-V curve of diode rectifier

These assumptions yield the following topology to model the average action of the nine-phase diode rectifier bridge. The input voltage to the diode bridge is shown in Figure 3-4 (b).

3.3.3. Commutation angle

There are five different operation modes for diode rectifier [38]. In this chapter, the model is only valid for Mode 1, which requires that the commutation should be finished within one switching period. For a three-phase diode rectifier, the commutation angle μ should be less than 60°; while for the nine-phase diode rectifier, μ should be less than 20°. The commutation angle is determined by the load current, commutation inductance, line frequency and voltage, which is shown in the following derivation. The validation of the model will be discussed in detail in section 3.5.



(a) topology **(b) input voltage**

Figure 3-4 Nine-phase diode rectifier

3.4. Improved dynamic average model of three-phase diode rectifier

The mathematical derivation method is used in this work to obtain the average model of diode rectifiers. As illustrated in Chapter 2, the difference among the static and dynamic model originally comes from their different assumptions on load current i_{dc}. In these models, the variation of i_{dc} is ignored either completely or partially during the derivation [41-43]. In this work, i_{dc} is assumed to vary linearly throughout the entire averaging period, i.e., during both commutation and conducting periods. Specifically, i_{dc} is approximated using its first-order Taylor Series expansion as

$$i_{dc}(\theta) = i_{dc0} + k \cdot (\theta - \frac{\mu}{2}), \tag{3-4}$$

where i_{dc0} is the average value of i_{dc} during the commutation period, μ is the commutation angle, and k is the derivative of current $di_{dc}/d\omega t$ during this period of time. Equation (3-4)

captures the variation of i_{dc} even during the commutation period, resulting in a better dynamic approximation for the converter output voltage and input currents.

Since μ only depends on the average current during the commutation [44], it is important that i_{dc0} be defined as the average current during the commutation period, not the entire averaging period as has been the case in previous work.

For convenience in derivation, the initial angle of input voltage source V_a is set to be $-\pi/3$, which is defined as

$$\begin{aligned} V_a &= V \cdot \cos\left(\omega \cdot t - \frac{\pi}{3}\right) \\ V_b &= V \cdot \cos\left(\omega \cdot t - \pi\right) \\ V_c &= V \cdot \cos\left(\omega \cdot t + \frac{\pi}{3}\right) \end{aligned} \quad . \tag{3-5}$$

3.4.1. Line current and commutation angle μ

The average model is to derive averaged ac line currents and dc output voltage during the commutation and conduction period, which are functions of the commutation angle μ. Therefore μ has to be determined as the first step. It can be accomplished by deriving one of the ac line currents using boundary conditions. The current chosen here for analysis is phase A's current of the direct bridge i_{ad}.

Choosing the average period when the current commutates from phase C to A ($\theta = 0$ till $\theta = \pi/3$), the boundary conditions for three line currents are

$$\begin{aligned}
[i]_{abc}\big|_{\theta=0} &= \left[0 \quad -i_{dc0}+k\,\mu/2 \quad i_{dc0}-k\,\mu/2\right] \\
[i]_{abc}\big|_{\theta=\mu} &= \left[i_{dc0}+k\,\mu/2 \quad -i_{dc0}-k\,\mu/2 \quad 0\right] \\
[i]_{abc}\big|_{\theta=\pi/3} &= \left[i_{dc0}+k\left(\pi/3-\mu/2\right) \quad -i_{dc0}-k\left(\pi/3-\mu/2\right) \quad 0\right]
\end{aligned} \tag{3-6}$$

During the commutation, phases A and C are shorted at the dc terminal and i_a is derived as

$$L_c \cdot \frac{di_c(t)}{dt} - L_c \cdot \frac{di_a(t)}{dt} = V_a - V_c, \tag{3-7}$$

when the parasitic resistor R_c is ignored and

$$i_c(t) + i_a(t) = -i_{dc}(t). \tag{3-8}$$

By substituting equations (3-4)(3-5)(3-8) into (3-7) and using the initial conditions when θ=0º, the differential equation describing the dynamics of i_a may be solved as

$$i_a(\theta) = -\frac{\sqrt{3}}{2\cdot\omega L_c}\cdot \mathrm{V}\cdot(1-\cos\theta) - \frac{\mathrm{k}}{2}\cdot\theta. \tag{3-9}$$

When i_a equals the full load dc current, the commutation period ends and phase C ceases to conduct when ω is μ, which means

$$-\frac{\sqrt{3}}{2\cdot\omega L_c}\cdot \mathrm{V}\cdot(1-\cos\mu) - \frac{\mathrm{k}}{2}\cdot\mu = -i_{dc0} - \mathrm{k}\cdot\left(\mu - \frac{\mu}{2}\right). \tag{3-10}$$

The commutation angle can then be derived from (3-10) as

$$\mu = \arccos\left(1 - \frac{2\cdot\omega L_c \cdot i_{dc0}}{V\cdot\sqrt{3}}\right). \tag{3-11}$$

When taking the parasitic resistor R_c into consideration, i_a is expressed as

$$i_a(\theta)=\frac{-\sqrt{3}}{2}\cdot\frac{V\cdot[R_c\cdot\sin(\theta)-\omega L_c\cdot\cos(\theta)]}{(\omega L_c)^2+R_c^{\,2}}-\frac{1}{2}\cdot\left(i_{dc0}-\frac{k\cdot u}{2}+k\cdot\theta\right)+\left[\frac{-\sqrt{3}}{2}\cdot\frac{V\cdot\omega L_c}{(\omega L_c)^2+R_c^{\,2}}+\frac{1}{2}\cdot\left(i_{dc0}-\frac{k\cdot u}{2}\right)\right]\cdot e^{-\frac{R_c}{\omega L_c}\cdot\theta} \quad (3\text{-}12)$$

If R_c is considered, μ has to be solved by the numerical method. However, under the system parameters in Table 3-1, the error of the commutation angle is 0.6% when R_c is neglected. Even if R_c increased 10 times, this error would be only 0.94%. Hence, equation (3-11) may be still considered valid when the R_c is taken into consideration in the rest of the derivation.

The line current expression could be further simplified if the dynamics of the load current is ignored, which is

$$i_a(\theta)=-\frac{\sqrt{3}}{2\cdot\omega L_c}\cdot \mathrm{V}\cdot(1-\cos\theta) \quad (3\text{-}13)$$

Comparing equations (3-9),(3-12) and (3-13) in Figure 3-5, it can be seen that the parasitic resistor R_c could be ignored, but dynamic k must be considered for an accurate result.

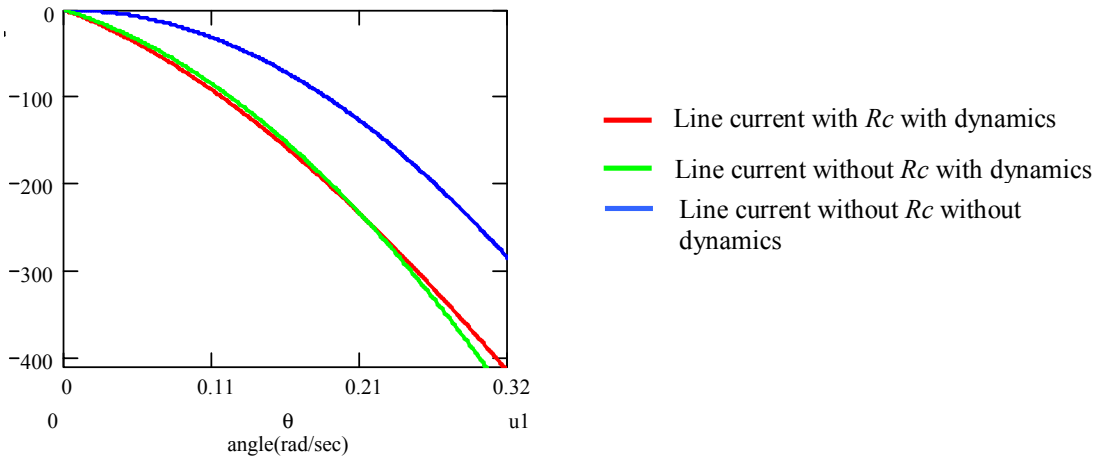


Figure 3-5 Line current comparison with and without R_c and dynamics

3.4.2. Averaged dc output voltage and current

From the rectifier side, the dc-side output voltage can be derived using integration as

$$V_{dc} = \frac{3}{\pi} \cdot \int_0^{\frac{\pi}{3}} \left[(V_a - V_b) + (\omega L_c) \cdot \left(\frac{di_b}{d\theta} - \frac{di_a}{d\theta} \right) + R_c \cdot (i_b - i_a) \right] \cdot d\theta \,. \tag{3-14}$$

According to boundary conditions in (3-6) and the current expression in (3-9), (3-14) may be solved in parts as

$$\begin{aligned}
&\frac{3}{\pi} \cdot \int_0^{\frac{\pi}{3}} (V_a - V_b) \cdot d\theta = \frac{3}{\pi} \sqrt{3} \cdot V \\
&\frac{3}{\pi} \cdot \int_0^{\frac{\pi}{3}} \omega L_c \cdot \left(\frac{di_b}{d\theta} - \frac{di_a}{d\theta} \right) \cdot d\theta = -\frac{3}{\pi} \cdot \omega L_c \cdot i_{dc0} - L_c \cdot \frac{di_{dc}}{dt} \cdot \left(2 - \frac{3\mu}{2\pi} \right) \\
&\frac{3}{\pi} \cdot \int_0^{\frac{\pi}{3}} R_c \cdot (i_b - i_a) \cdot d\theta = \frac{V}{2 \cdot \omega L_c} \cdot R_c \cdot \frac{3 \cdot \sqrt{3}}{\pi} \cdot (-\mu + \sin\mu) - R_c \cdot i_{dc0} \cdot \left(2 - \frac{3\mu}{\pi} \right) \\
&\qquad - \frac{di_{dc}}{dt} \cdot \frac{R_c}{\omega} \cdot \left(\frac{\pi}{3} - \mu + \frac{3}{\pi} \cdot \frac{\mu^2}{4} \right)
\end{aligned} \,. \tag{3-15}$$

Additionally, the diode is modeled by its I-V curve in Figure 3-3 with its forward voltage drop V_{on} and on-state resistance R_{on}. The final expression of the output voltage is

$$\begin{aligned}
V_{dc} = {} & \frac{3\sqrt{3}}{\pi} \cdot V \cdot \left(1 + (R_c + R_{on}) \cdot \frac{-\mu + \sin\mu}{2 \cdot \omega L} \right) - \left[\frac{3}{\pi} \cdot \omega L_c + (R_c + R_{on}) \cdot \left(2 - \frac{3\mu}{\pi} \right) \right] \cdot i_{dc0} \\
& - \frac{di_{dc}}{dt} \cdot \left[L_c \cdot \left(2 - \frac{3\mu}{2\pi} \right) + \frac{(R_c + R_{on})}{\omega} \cdot \left(\frac{\pi}{3} - \mu + \frac{3}{\pi} \cdot \frac{\mu^2}{4} \right) \right] - 2 \cdot V_{on} .
\end{aligned} \tag{3-16}$$

Finally, equating (3-16) with the averaged dc-link equation in that period

$$V_{dc} = V_{load} + R_{dc} \cdot \left(i_{dc0} + \frac{k}{2} \cdot \left(\frac{\pi}{3} - \mu \right) \right) + L_{dc} \cdot \frac{di_{dc}}{dt} \,, \tag{3-17}$$

yields the state space equation of i_{dc}

$$\frac{di_{dc}}{dt}=\frac{\frac{3\sqrt{3}}{\pi}\cdot V\cdot\left(1+\left(R_c+R_{on}\right)\cdot\frac{-\mu+\sin\mu}{2\cdot\omega L_c}\right)-\left[\frac{3}{\pi}\cdot\omega L_c+\left(R_c+R_{on}\right)\cdot\left(2-\frac{3\mu}{\pi}\right)+\mathrm{R_{dc}}\right]\cdot i_{dc0}-V_{load}-2\cdot V_{on}}{L_{dc}+L_c\cdot\left(2-\frac{3\mu}{2\pi}\right)+\frac{2\cdot\left(R_c+R_{on}\right)+R_{dc}}{2\omega}\cdot\left(\frac{\pi}{3}-\mu\right)+\frac{R_c+R_{on}}{\omega}\cdot\frac{3}{\pi}\cdot\frac{\mu^2}{4}} \tag{3-18}$$

3.4.3. Averaged ac currents

The ac currents in the *dq*-axes have the same period as that of the output dc voltage, so it is reasonable to average the ac currents in the *dq*-axes with the Park transformation. The dc load current maintains its dynamic information as shown in (3-4) throughout the entire derivation. By using this equation and the integration boundary conditions given in (3-6), the averaged ac line currents can be derived. Because the line currents have different expressions during the commutation and conduction periods, the average model is derived at each interval and summarized together as

$$\begin{aligned}\overline{i_d}&=\overline{i_{d,com}}+\overline{i_{d,con}}\\ \overline{i_q}&=\overline{i_{q,com}}+\overline{i_{q,con}}\end{aligned}, \tag{3-19}$$

where $i_{d,com}$ and $i_{q,com}$ are currents during the commutation period, and $i_{d,con}$ and $i_{q,con}$ are the ones during the conduction period.

In order to simplify the derivation, the initial angle of the *dq*-axes transformation will be set to be zero. This requires the initial angle of the input voltage source to be zero, not $-\pi/3$ as the one in the above section. The current commutation between i_a and i_b occurs at $\pi/3$. Specifically, during the commutation period, the ac line currents are given by

$$\begin{aligned} i_a(\theta) &= -i_{dc0} + \frac{\sqrt{3}\cdot V}{2\cdot\omega\cdot L_c}\cdot(1-\cos\theta) - \frac{k}{2}\cdot\left(\theta-\frac{\pi}{3}-\mu\right) \\ i_b(\theta) &= -\frac{\sqrt{3}\cdot V}{2\cdot\omega\cdot L_c}\cdot(1-\cos\theta) - \frac{k}{2}\cdot\left(\theta-\frac{\pi}{3}\right) \\ i_c(\theta) &= i_{dc0} + k\cdot\left(\theta-\frac{\pi}{3}-\frac{\mu}{2}\right) \end{aligned} \quad . \tag{3-20}$$

Then, by applying the Park transformation, we have

$$\begin{aligned} i_{d,com}(\theta) &= \sqrt{\frac{2}{3}}\cdot\left(\cos\theta\cdot i_a(\theta) + \cos\left(\theta-\frac{2\pi}{3}\right)\cdot i_b(\theta) + \cos\left(\theta+\frac{2\pi}{3}\right)\cdot i_c(\theta)\right) \\ i_{q,com}(\theta) &= \sqrt{\frac{2}{3}}\cdot\left(-\sin\theta\cdot i_a(\theta) - \sin\left(\theta-\frac{2\pi}{3}\right)\cdot i_b(\theta) - \sin\left(\theta+\frac{2\pi}{3}\right)\cdot i_c(\theta)\right) \end{aligned} \quad . \tag{3-21}$$

Averaging above currents during [$\pi/3$, $\mu+\pi/3$], the averages dq-axes currents during commutation period are given by

$$\begin{aligned} \overline{i_{d,com}} &= \frac{3}{\pi}\cdot\left[-\sqrt{2}\cdot i_{dc0}\cdot\left(\cos\left(\frac{2\pi}{3}+\mu\right)+\frac{1}{2}\right)+\sqrt{\frac{3}{2}}\cdot\frac{V}{\omega L_c}\cdot\left(-\cos\mu+\frac{\cos 2\mu}{4}+\frac{3}{4}\right)\right] \\ &\quad -\frac{3\sqrt{2}}{2\pi}\cdot\mathrm{k}\cdot\left[-\sqrt{3}+\sqrt{3}\cdot\cos\mu-\mu\cdot\cos\left(\mu+\frac{\pi}{3}\right)+\frac{1}{2}\mu\right] \\ \overline{i_{q,com}} &= \frac{3}{\pi}\cdot\left[\sqrt{2}\cdot i_{dc0}\cdot\left(\sin\left(\frac{2\pi}{3}+\mu\right)-\frac{\sqrt{3}}{2}\right)+\sqrt{\frac{3}{2}}\cdot\frac{V}{\omega L_c}\cdot\left(\sin\mu-\frac{\sin 2\mu}{4}-\frac{\mu}{2}\right)\right] \\ &\quad -\frac{\sqrt{6}}{2\pi}\cdot\mathrm{k}\cdot\left[-3+\frac{3}{2}\cdot\mu\cdot\cos\mu+\frac{\sqrt{3}}{2}\cdot\mu\cdot\sin\mu+\frac{3}{2}\mu\right] \end{aligned} \tag{3-22}$$

The line currents during the conduction period are

$$\begin{aligned} i_a(\theta) &= 0 \\ i_b(\theta) &= -\left[i_{dc0} + k\cdot\left(\theta-\frac{\pi}{3}-\frac{\mu}{2}\right)\right] \\ i_c(\theta) &= i_{dc0} + k\cdot\left(\theta-\frac{\pi}{3}-\frac{\mu}{2}\right) \end{aligned} \quad . \tag{3-23}$$

The average dq-axes currents during the conduction period can be derived using the same approach, which is

$$\begin{aligned}\overline{i_{d,con}} &= \frac{3\sqrt{2}}{\pi}\cdot\left[\cos\left(\mu+\frac{\pi}{3}\right)+\frac{1}{2}\right]\cdot i_{dc0}-\frac{3\sqrt{2}}{\pi}k\cdot\left[\frac{\sqrt{3}}{2}+\frac{\pi}{6}+\frac{\mu}{2}\cdot\left(\cos\left(\mu+\frac{\pi}{3}\right)-\frac{1}{2}\right)-\sin\left(\mu+\frac{\pi}{3}\right)\right]\\ \overline{i_{q,con}} &= \frac{3\sqrt{2}}{\pi}\cdot\left[\sin\left(\mu+\frac{\pi}{3}\right)-\frac{\sqrt{3}}{2}\right]\cdot i_{dc0}-\frac{3\sqrt{2}}{\pi}k\cdot\left[-\frac{1}{2}+\frac{\sqrt{3}\cdot\pi}{6}-\frac{\sqrt{3}\cdot\mu}{4}-\cos\left(\mu+\frac{\pi}{3}\right)-\frac{\mu}{2}\sin\left(\mu+\frac{\pi}{3}\right)\right]\end{aligned} \quad (3\text{-}24)$$

Substituting equations (3-22) (3-24) into (3-19) , the average currents in the *dq*-axes are

$$\begin{aligned}\overline{i_d} &= \frac{3\sqrt{2}}{\pi}\cdot i_{dc0}\cdot\cos\mu+\frac{3\sqrt{2}}{2\pi}\cdot k\cdot\left(\sin\mu-\frac{\pi}{3}\right)-\frac{3\sqrt{6}}{2\pi}\cdot\frac{V}{\omega L_c}\cdot\left(\cos\mu-\frac{\cos 2\mu}{4}-\frac{3}{4}\right)\\ \overline{i_q} &= -\frac{3\sqrt{2}}{\pi}\cdot i_{dc0}\cdot\sin\mu+\frac{3\sqrt{2}}{2\pi}\cdot k\cdot\left(1+\cos\mu-\frac{\sqrt{3}\pi}{3}\right)-\frac{3\sqrt{6}}{2\pi}\cdot\frac{V}{\omega L_c}\cdot\left(-\sin\mu+\frac{\mu}{2}+\frac{\sin 2\mu}{4}\right)\end{aligned} \quad (3\text{-}25)$$

The complete average model of three-phase diode rectifier is composed of equation (3-18) and (3-25).

3.5. Improved dynamic average model of nine-phase diode rectifier

The procedure to derive the average model of the nine-phase diode rectifier is almost the same as the one of the three-phase diode rectifier. The input voltage to the diode rectifier is the secondary voltage of the autotransformer unit. For convenience in derivation, the initial angle of the primary input voltage source V_a is set to be – */9*, which is defined as

$$\begin{aligned}V_a &= V_p\cdot\cos\left(\omega\cdot t-\frac{\pi}{9}\right)\\ V_b &= V_p\cdot\cos\left(\omega\cdot t-\frac{\pi}{9}-\frac{2\pi}{3}\right)\\ V_c &= V_p\cdot\cos\left(\omega\cdot t-\frac{\pi}{9}+\frac{2\pi}{3}\right).\end{aligned} \quad (3\text{-}26)$$

The secondary voltages then become

$$V_{ad} = V_s \cdot \cos\left(\omega \cdot t - \frac{\pi}{9}\right) \qquad V_{af} = V_s \cdot \cos\left(\omega \cdot t - \frac{\pi}{9} + \frac{2\pi}{9}\right)$$
$$V_{bd} = V_s \cdot \cos\left(\omega \cdot t - \frac{\pi}{9} - \frac{2\pi}{3}\right) \quad , \quad V_{bf} = V_s \cdot \cos\left(\omega \cdot t - \frac{\pi}{9} - \frac{2\pi}{3} + \frac{2\pi}{9}\right),$$
$$V_{cd} = V_s \cdot \cos\left(\omega \cdot t - \frac{\pi}{9} + \frac{2\pi}{3}\right). \qquad V_{cf} = V_s \cdot \cos\left(\omega \cdot t - \frac{\pi}{9} + \frac{2\pi}{3} + \frac{2\pi}{9}\right)$$

(3-27)

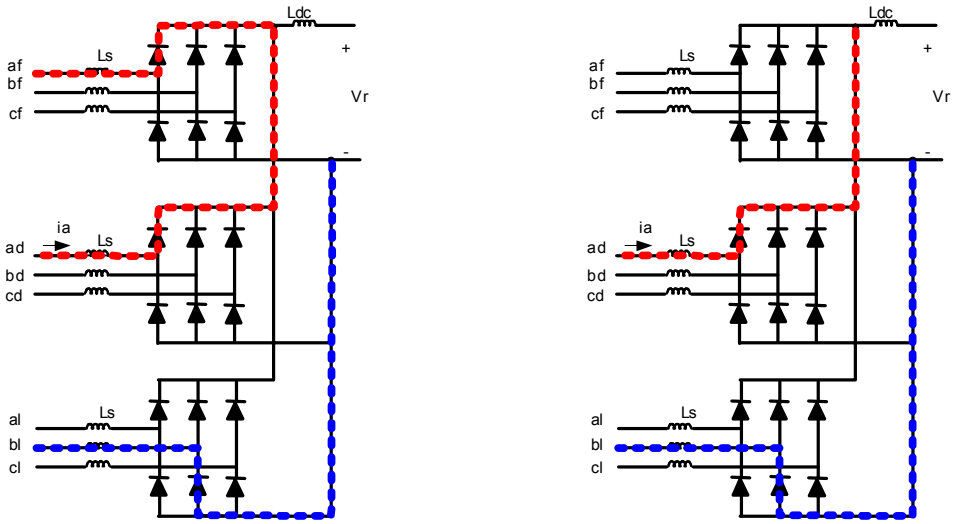
$$V_{al} = V_s \cdot \cos\left(\omega \cdot t - \frac{\pi}{9} - \frac{2\pi}{9}\right)$$
$$V_{bl} = V_s \cdot \cos\left(\omega \cdot t - \frac{\pi}{9} - \frac{2\pi}{3} - \frac{2\pi}{9}\right),$$
$$V_{cl} = V_s \cdot \cos\left(\omega \cdot t - \frac{\pi}{9} + \frac{2\pi}{3} - \frac{2\pi}{9}\right)$$

where V_{ad}, V_{bd} and V_{cd} are for the direct bridge, V_{af}, V_{bf} and V_{cf} are for the forward bridge and V_{al}, V_{bl} and V_{cl} are for the lagging one.

3.5.1. Commutation and conduction for nine-phase diode rectifier

The nine-phase diode rectifier has commutation and conduction modes during one switching period, similar to the three-phase diode rectifier. Figure 3-6 depicts the active diodes during a full period, showing the commutation period where three diodes are conducting in (a) and the conduction period where only two diodes conduct in (b) as previously described.

The averaging period of this rectifier is chosen to be 20° because the ripple frequency of its output voltage is 18 times that of the input voltage source (18-pulse), which implies that a commutation occurs every 20° on its nine-phase ac side.



(a) **commutation period** **(b) conduction period**

Figure 3-6 Commutation and conduction period of nine-phase diode rectifier

3.5.2. Commutation inductance of nine-phase diode rectifier

When deriving the average model for a three-phase diode rectifier, the commutation inductance is the line inductance of the feeders and cables. However, for the nine-phase diode rectifier, the commutation inductance is not as simple to determine due to the autotransformer.

From the nine-phase diode rectifier topology in Figure 3-1, the commutation inductance includes both the feeder's inductance L_p and the leakage inductance L_s of the autotransformer. A straightforward way to model L_p into the commutation inductance is to refer it onto the secondary side of the autotransformer. If the voltage and current of the autotransformer are all sinusoidal waveforms, L_p can be referred to the secondary side by multiplying the square of the autotransformer's turns ratio. However, the secondary current is a square waveform because of the diode bridge, which changes the current ratio

of the autotransformer. A new current ratio between the primary and the secondary of the autotransformer must be derived. Assuming that the transformer's core magnetomotive force (MMF) is zero, the first equation $\sum n \cdot i = 0$ is given for each leg of the autotransformer. Using Kirchoff's current law at each node as the second equation, the transfer function of the primary and the secondary current of each phase can be derived as

$$\begin{aligned}
i_{ap} &= \left(1-\frac{k_3}{k_2+k_p}\right)\cdot i_{ad} + \frac{2\cdot k_p + k_2}{2\cdot(k_p+k_2)}\cdot(i_{af}+i_{al}) + \frac{k_{21}}{2\cdot(k_p+k_2)}\cdot i_{bd} \\
&\quad + \frac{k_1+k_2}{2\cdot(k_p+k_2)}\cdot(i_{bf}+i_{cl}) - \frac{k_1}{2\cdot(k_p+k_2)}\cdot(i_{bl}+i_{cf}) + \frac{k_3}{2\cdot(k_p+k_2)}\cdot i_{cd} \\
i_{bp} &= \left(1-\frac{k_3}{k_2+k_p}\right)\cdot i_{bd} + \frac{2\cdot k_p + k_2}{2\cdot(k_p+k_2)}\cdot(i_{bf}+i_{bl}) + \frac{k_{21}}{2\cdot(k_p+k_2)}\cdot i_{cd} \\
&\quad + \frac{k_1+k_2}{2\cdot(k_p+k_2)}\cdot(i_{cf}+i_{al}) - \frac{k_1}{2\cdot(k_p+k_2)}\cdot(i_{cl}+i_{af}) + \frac{k_3}{2\cdot(k_p+k_2)}\cdot i_{ad} \\
i_{cp} &= \left(1-\frac{k_3}{k_2+k_p}\right)\cdot i_{cd} + \frac{2\cdot k_p + k_2}{2\cdot(k_p+k_2)}\cdot(i_{cf}+i_{cl}) + \frac{k_{21}}{2\cdot(k_p+k_2)}\cdot i_{ad} \\
&\quad + \frac{k_1+k_2}{2\cdot(k_p+k_2)}\cdot(i_{af}+i_{bl}) - \frac{k_1}{2\cdot(k_p+k_2)}\cdot(i_{al}+i_{bf}) + \frac{k_3}{2\cdot(k_p+k_2)}\cdot i_{bd}
\end{aligned}, \tag{3-28}$$

where i_{ap}, i_{bp} and i_{cp} are primary line currents for each phase of the autotransformer.

During commutation, only three branches conduct current. An example of this is when current transfers from i_{af} to i_{ad}, only i_{ad}, i_{af} and i_{bl} are not zero, which results in

$$i_{ap} = \left(1-\frac{k_3}{k_2+k_p}\right)\cdot i_{ad} + \frac{2\cdot k_p + k_2}{2\cdot(k_p+k_2)}\cdot i_{af} - \frac{k_1}{2\cdot(k_p+k_2)}\cdot i_{bl}\,. \tag{3-29}$$

During that commutation period, we also have

$$i_{af} + i_{ad} = -i_{dc}, \quad i_{bl} = i_{dc}\,. \tag{3-30}$$

Substituting equation (3-29) into (3-30), the primary line current can be written as

$$i_{ap} = \left(1 - \frac{2 \cdot k_3 + 2 \cdot k_p + k_2}{2 \cdot \left(k_2 + k_p\right)}\right) \cdot i_{ad} - \frac{2 \cdot k_p + k_2 + k_1}{2 \cdot \left(k_p + k_2\right)} \cdot i_{dc} . \tag{3-31}$$

If i_{dc} is assumed to keep constant, it is can be derived as

$$L_p \cdot \frac{di_{ap}}{dt} = L_p \cdot \left(1 - \frac{2 \cdot k_3 + 2 \cdot k_p + k_2}{2 \cdot \left(k_2 + k_p\right)}\right) \cdot \frac{di_{ad}}{dt} = 0.138 L_p \cdot \frac{di_{ad}}{dt} \tag{3-32}$$

So the current ratio from the primary to the secondary line currents in terms of commutation should be 0.138.

In one entire period 2π, there are two different modes of commutation. One mode is commutation between different bridges of the same phase, such as current commutation between (i_{af}, i_{ad}), (i_{ad}, i_{al}), (i_{bf}, i_{bd}), (i_{bd}, i_{bl}), (i_{cf}, i_{cd}) and (i_{cd}, i_{cl}). The other mode is the commutation between different phases, which is commutated between (i_{al}, i_{bf}), (i_{bl}, i_{cf}) and (i_{cl}, i_{af}). The current ratios of these two modes are not the same. The first mode is 0.138 as derived above, while it will be 0.375 for the other mode. Their occurrence times differ at a ratio of two to one. Since the assumption of the average model requires the commutation inductance to be identical at all times, the current ratio can be averaged as

$$n_i^{'} = \left(\frac{0.138 \times 2 + 0.375}{3}\right) = 0.217 , \tag{3-33}$$

and the total equivalent commutation inductance is

$$L_c = L_s + L_p \cdot n_v \cdot n_i^{'} . \tag{3-34}$$

For simplicity, the total parasitic resistor are also referred to the secondary side of the autotransformer as

$$R_c = R_s + R_p \cdot n_v \cdot n_i^{'} . \tag{3-35}$$

3.5.3. Average model of nine-phase diode rectifier

3.5.3.1. Line current and averaged dc voltage

Just as the three-phase diode bridge, the commutation angle μ for the nine-phase diode rectifier is derived first by the secondary line current. For instance, the commutation between i_{ad} and i_{af} occurs at time zero, while i_{bl} conducts load current all the time. The boundary conditions for the secondary line currents are

$$\begin{aligned}
\begin{bmatrix} i_{ad} & i_{af} & i_{bl} \end{bmatrix}_{\theta=0} &= \begin{bmatrix} 0 & -i_{dc0} + k\,\mu/2 & i_{dc0} - k\,\mu/2 \end{bmatrix} \\
\begin{bmatrix} i_{ad} & i_{af} & i_{bl} \end{bmatrix}_{\theta=\mu} &= \begin{bmatrix} -i_{dc0} - k\,\mu/2 & 0 & i_{dc0} + k\,\mu/2 \end{bmatrix} \\
\begin{bmatrix} i_{ad} & i_{af} & i_{bl} \end{bmatrix}_{\theta=\pi/9} &= \begin{bmatrix} -i_{dc0} - k\left(\pi/9 - \mu/2\right) & 0 & i_{dc0} + k\cdot\left(\frac{\pi}{9} - \frac{\mu}{2}\right) \end{bmatrix}
\end{aligned} . \tag{3-36}$$

From the rectifier schematic, the differential equation can be written as

$$L_c \cdot \frac{di_{ad}(t)}{dt} - L_c \cdot \frac{di_{ap}(t)}{dt} = V_{ad} - V_{ap} . \tag{3-37}$$

The line current can be derived using the same approach that is used for the three-phase diode rectifier. It is

$$i_{ad}(\theta) = -\frac{V}{\omega L_c} \cdot \sin\left(\frac{\pi}{9}\right) \cdot (1 - \cos\theta) - \frac{\mathrm{k}}{2} \cdot \theta \tag{3-38}$$

without considering the parasitic resistor R_c. When taking R_c into consideration, it becomes

$$\begin{aligned}
i_a(\theta) = &-\frac{V \cdot \sin\left(\frac{\pi}{9}\right) \cdot [R_c \cdot \sin(\theta) - \omega L_c \cdot \cos(\theta)]}{(\omega L_c)^2 + {R_c}^2} - \frac{1}{2} \cdot \left(i_{dc0} - \frac{k \cdot u}{2} + k \cdot \theta\right) \\
&+ \left[-\frac{V \cdot \sin\left(\frac{\pi}{9}\right) \cdot \omega L_c}{(\omega L_c)^2 + {R_c}^2} + \frac{1}{2} \cdot \left(i_{dc0} - \frac{k \cdot u}{2}\right)\right] \cdot e^{-\frac{R_c}{\omega L_c} \cdot \theta}
\end{aligned} . \tag{3-39}$$

The parasitic resistor R_c does not influence the commutation angle much. The commutation angle can be calculated using equation (3-38) as

$$\mu = a\cos\left(1-\frac{\omega\cdot L_c\cdot i_{dc}}{V\cdot\sin\left(\frac{\pi}{9}\right)}\right). \tag{3-40}$$

The dc output voltage of the nine-phase diode rectifier is expressed as the following equation when diodes and all other parasitic parameters are considered

$$\begin{aligned} V_{dc} = {} & \frac{18}{\pi}\cdot V\cdot\sin\left(\frac{\pi}{9}\right)\cdot\left(1+(R_c+R_{on})\cdot\frac{-\mu+\sin\mu}{2\cdot\omega L_c}\right)-\left[\frac{9}{\pi}\cdot\omega L_c+(R_c+R_{on})\cdot\left(2-\frac{9\mu}{\pi}\right)\right]\cdot i_{dc0} \\ & -\frac{di_{dc}}{dt}\cdot\left[L_c\cdot\left(2-\frac{9\mu}{2\pi}\right)+\frac{(R_c+R_{on})}{\omega}\cdot\left(\frac{\pi}{9}-\mu+\frac{9}{\pi}\cdot\frac{\mu^2}{4}\right)\right]-2\cdot V_{on} \end{aligned}. \tag{3-41}$$

The averaged dc-link equation in that period is

$$V_{dc} = V_{load} + R_{dc}\cdot\left(i_{dc0}+\frac{k}{2}\cdot\left(\frac{\pi}{9}-\mu\right)\right)+L_{dc}\cdot\frac{di_{dc}}{dt}. \tag{3-42}$$

The state space equation of i_{dc} can be derived by making (3-41) and (3-42) be equal as

$$\frac{di_{dc}}{dt} = \frac{\frac{18}{\pi}\cdot V\cdot\sin\left(\frac{\pi}{9}\right)\cdot\left(1+(R_c+R_{on})\cdot\frac{-\mu+\sin\mu}{2\cdot\omega L_c}\right)-\left[\frac{9}{\pi}\cdot\omega L_c+(R_c+R_{on})\cdot\left(2-\frac{9\mu}{\pi}\right)+\mathrm{R_{dc}}\right]\cdot i_{dc0}-V_{load}-2\cdot V_{on}}{L_{dc}+L_c\cdot\left(2-\frac{9\mu}{2\pi}\right)+\frac{2\cdot(R_c+R_{on})+R_{dc}}{2\omega}\cdot\left(\frac{\pi}{9}-\mu\right)+\frac{R_c+R_{on}}{\omega}\cdot\frac{9}{\pi}\cdot\frac{\mu^2}{4}}. \tag{3-43}$$

3.5.3.2. Averaged ac currents

When deriving the average currents in the *dq*-axes for a three-phase diode rectifier, the traditional *dq* frame transformation, as shown in equation (3-3), can be utilized. Nevertheless, this transformation is not suitable for the nine-phase diode rectifier because

there are nine vectors to be transferred to *dq*-axes. A new *dq* frame transformation T_{dq}^{9} for these vectors is then defined as (3-45).

The coefficient in (3-45) is to make $(T_{dq}^{9})^{-1}$ equal to $(T_{dq}^{9})^{T}$ and the converter active power remains constant in the *abc*, three-phase, and nine-phase *d-q* frames. For nine-phase vectors, we have

$$X_{dq}^{9} = T_{dq}^{9} \cdot X^{9} \quad \text{and} \quad X^{9} = \left(T_{dq}^{9}\right)^{T} \cdot X_{dq}^{9} \ . \tag{3-44}$$

$$T_{dq}^{9} = \frac{1}{3} \cdot \sqrt{\frac{2}{3}} \cdot \begin{bmatrix} \cos\left(\theta + \frac{2\pi}{9}\right) & -\sin\left(\theta + \frac{2\pi}{9}\right) \\ \cos\left(\theta - \frac{4\pi}{9}\right) & -\sin\left(\theta - \frac{4\pi}{9}\right) \\ \cos\left(\theta + \frac{8\pi}{9}\right) & -\sin\left(\theta + \frac{8\pi}{9}\right) \\ \cos\theta & -\sin\theta \\ \cos\left(\theta - \frac{2\pi}{3}\right) & -\sin\left(\theta - \frac{2\pi}{3}\right) \\ \cos\left(\theta + \frac{2\pi}{3}\right) & -\sin\left(\theta + \frac{2\pi}{3}\right) \\ \cos\left(\theta - \frac{2\pi}{9}\right) & -\sin\left(\theta - \frac{2\pi}{9}\right) \\ \cos\left(\theta - \frac{8\pi}{9}\right) & -\sin\left(\theta - \frac{8\pi}{9}\right) \\ \cos\left(\theta + \frac{4\pi}{9}\right) & -\sin\left(\theta + \frac{4\pi}{9}\right) \end{bmatrix}^{T} . \tag{3-45}$$

When the input voltage is the one in equation (3-27), the three secondary line currents conducting current during the commutation period are

$$\begin{aligned} i_{ad}(\theta) &= -\frac{V \cdot \sin\left(\frac{\pi}{9}\right)}{\omega \cdot L_c} \cdot (1 - \cos\theta) - \frac{k}{2} \cdot \theta \\ i_{af}(\theta) &= -i_{dc0} + \frac{V \cdot \sin\left(\frac{\pi}{9}\right)}{\omega \cdot L_c} \cdot (1 - \cos\theta) - \frac{k}{2} \cdot (\theta - \mu) \\ i_{bl}(\theta) &= i_{dc0} + k \cdot \left(\theta - \frac{\mu}{2}\right) \end{aligned} . \tag{3-46}$$

In each period, there are only three secondary branches conducting current during the commutation period; while there are only two secondary branches conducting current during the conduction period. This will simplify the current derivation in the *dq*-axes significantly. Applying equation (3-44) to derive the *dq*-axes currents at the secondary side of the autotransformer gives

$$\begin{aligned} i_{d,com}(\theta) &= \frac{\sqrt{2}}{3\cdot\sqrt{3}}\cdot\left(\cos\theta\cdot i_{ad}(\theta)+\cos\left(\theta+\frac{2\pi}{9}\right)\cdot i_{af}(\theta)+\cos\left(\theta-\frac{2\pi}{3}-\frac{2\pi}{9}\right)\cdot i_{bl}(\theta)\right) \\ i_{q,com}(\theta) &= -\frac{\sqrt{2}}{3\cdot\sqrt{3}}\cdot\left(\sin\theta\cdot i_{ad}(\theta)+\sin\left(\theta+\frac{2\pi}{9}\right)\cdot i_{af}(\theta)+\sin\left(\theta-\frac{2\pi}{3}-\frac{2\pi}{9}\right)\cdot i_{bl}(\theta)\right) \end{aligned} \quad . \tag{3-47}$$

Averaging (3-47) in [*0, /9*], the averaged ac currents in *dq*-axes during the commutation are

$$\begin{aligned} \overline{i_{d,com}} &= \frac{9}{\pi}\cdot\frac{\sqrt{2}}{3\cdot\sqrt{3}}\cdot\left\{\frac{1}{16}\cdot\frac{\mathrm{V}}{\omega\mathrm{L_c}}\cdot\left[\left(6\cdot\sin\left(\frac{\pi}{9}\right)-\sqrt{3}\right)\cdot\left(\sin(2\mu)-4\cdot\sin\mu+2\mu\right)\right.\right. \\ &\quad +\left[\left(1-2\cos\left(\frac{\pi}{9}\right)\right)\cdot\left(\cos 2\mu-4\cdot\cos\mu+3\right)\right]+\left[\cos\left(\frac{\pi}{18}\right)\cdot\left(1-2\cdot\sin\left(\mu+\frac{\pi}{6}\right)\right)\right]\cdot\mathrm{i_{dc0}} \\ &\quad \left.\left.+\mathrm{k}\cdot\left[\frac{\mu}{2}\cdot\left(-\cos\left(\frac{\pi}{18}\right)-\sin\mu-\sin\left(\mu+\frac{\pi}{9}\right)\right)+\left(\cos\left(\frac{\pi}{9}\right)+1\right)\cdot\left(\cos\frac{\pi}{9}-\cos\left(\mu+\frac{\pi}{9}\right)\right)\right]\right\} \\ \overline{i_{q,com}} &= -\frac{9}{\pi}\cdot\frac{\sqrt{2}}{3\cdot\sqrt{3}}\cdot\left\{\frac{1}{16}\cdot\frac{\mathrm{V}}{\omega\mathrm{L_c}}\cdot\left[\left(2\cdot\cos\left(\frac{\pi}{9}\right)-1\right)\cdot\left(2\mu-\sin(2\mu)+4\cdot\sin\mu\right)\right.\right. \\ &\quad +\left(\left(6\sin\left(\frac{\pi}{9}\right)-\sqrt{3}\right)\cdot\left(-\cos 2\mu+4\cdot\cos\mu-3\right)\right)+\left[\cos\left(\frac{\pi}{18}\right)\cdot\left(2\cdot\cos\left(\mu+\frac{\pi}{6}\right)-\sqrt{3}\right)\right]\cdot\mathrm{i_{dc0}} \\ &\quad \left.\left.+\mathrm{k}\cdot\left[\mu\cdot\cos\left(\frac{\pi}{18}\right)\cdot\left(\cos\left(\mu+\frac{\pi}{18}\right)+\frac{\sqrt{3}}{2}\right)+\left(\cos\left(\frac{\pi}{9}\right)+1\right)\cdot\left(\sin\frac{\pi}{9}-\sin\left(\mu+\frac{\pi}{9}\right)\right)\right]\right\} \end{aligned} \tag{3-48}$$

The line currents during the conduction period are

$$\begin{aligned} i_{ac}(\theta) &= -i_{dc0}+k\cdot\left(\theta-\frac{\mu}{2}\right) \\ i_{af}(\theta) &= 0 \\ i_{bl}(\theta) &= i_{dc0}+k\cdot\left(\theta-\frac{\mu}{2}\right) \end{aligned} \quad . \tag{3-49}$$

The corresponding averaged currents are

$$\begin{aligned}
\overline{i_{d,con}} &= \frac{9}{\pi}\cdot\frac{\sqrt{2}}{3\cdot\sqrt{3}}\cdot\left\{\left[-\cos\left(\frac{\pi}{18}\right)+\sin\mu+\sin\left(\mu+\frac{\pi}{9}\right)\right]\cdot \mathrm{i}_{\mathrm{dc0}}\right. \\
&\left.+k\cdot\left[\frac{\mu}{2}\cdot\cos\left(\frac{\pi}{18}\right)\cdot\left(1+2\cdot\sin\left(\mu+\frac{\pi}{18}\right)\right)+\cos\left(\mu+\frac{\pi}{9}\right)+\cos\mu-\cos\left(\frac{\pi}{18}\right)\cdot\left(\sqrt{3}+\frac{\pi}{9}\right)\right]\right\} \quad . \\
\overline{i_{q,con}} &= -\frac{9}{\pi}\cdot\frac{\sqrt{2}}{3\cdot\sqrt{3}}\cdot\left\{\left[\sqrt{3}\cdot\cos\left(\frac{\pi}{18}\right)-\cos\mu-\cos\left(\mu+\frac{\pi}{9}\right)\right]\cdot \mathrm{i}_{\mathrm{dc0}}\right. \\
&\left.+\mathrm{k}\cdot\left[-\frac{\mu}{2}\cdot\cos\left(\frac{\pi}{18}\right)\cdot\left(2\cos\left(\mu+\frac{\pi}{18}\right)+\sqrt{3}\right)+\sin\left(\mu+\frac{\pi}{9}\right)+\sin\mu-\cos\left(\frac{\pi}{18}\right)\cdot\left(1-\frac{\pi}{9}\cdot\sqrt{3}\right)\right]\right\}
\end{aligned} \tag{3-50}$$

Summarizing the above equations, the averaged ac currents in *dq*-axes are

$$\begin{aligned}
\overline{i_d} &= \frac{9}{\pi}\cdot\frac{\sqrt{2}}{3\cdot\sqrt{3}}\left\{\left[\cos\left(\frac{\pi}{18}\right)\cdot\left(2\sin\left(\frac{\pi}{6}+\mu\right)-1\right)-\sin\left(\mu+\frac{\pi}{9}\right)-\sin\mu+\cos\left(\frac{\pi}{18}\right)\right]\cdot i_{dc0}\right. \\
&+\frac{1}{16}\cdot\frac{V}{\omega L_c}\cdot\left[\left(-6\sin\left(\frac{\pi}{9}\right)+\sqrt{3}\right)\cdot(\sin 2\mu-4\cdot\sin\mu+2\cdot\mu)+\left(2\cos\left(\frac{\pi}{9}\right)-1\right)\cdot(\cos 2\mu-4\cos\mu+3)\right], \\
&+\mathrm{k}\cdot\left[\frac{\mu}{2}\cdot\left(\sin\mu+\sin\left(\frac{\pi}{9}+\mu\right)-2\cdot\sin\left(\mu+\frac{\pi}{18}\right)\cdot\cos\frac{\pi}{18}\right)-\cos\mu-\cos\left(\mu+\frac{\pi}{9}\right)\right. \\
&\left.\left.+\left(\cos\left(\frac{\pi}{9}\right)+1\right)\cdot\left(-\cos\left(\frac{\pi}{9}\right)+\cos\left(\mu+\frac{\pi}{9}\right)\right)+\cos\left(\frac{\pi}{18}\right)\cdot\left(\sqrt{3}+\frac{\pi}{9}\right)\right]\right\}
\end{aligned} \tag{3-51}$$

$$\begin{aligned}
\overline{i_q} &= -\frac{9}{\pi}\cdot\frac{\sqrt{2}}{3\cdot\sqrt{3}}\cdot\left\{\left[-2\cos\left(\frac{\pi}{18}\right)\cdot\cos\left(\frac{\pi}{6}+\mu\right)+\cos\mu+\cos\left(\mu+\frac{\pi}{9}\right)\right]\cdot i_{dc0}\right. \\
&+\frac{1}{16}\cdot\frac{V}{\omega L_c}\cdot\left[\left(1-2\cos\left(\frac{\pi}{9}\right)\right)\cdot(4\sin\mu-\sin 2\mu+2\mu)+\left(6\sin\left(\frac{\pi}{9}\right)-\sqrt{3}\right)\cdot(-4\cos\mu+\cos 2\mu+3)\right]. \\
&\left.+\mathrm{k}\cdot\left[\left(\cos\left(\frac{\pi}{9}\right)+1\right)\cdot\left(-\sin\left(\frac{\pi}{9}\right)+\sin\left(\mu+\frac{\pi}{9}\right)\right)-\sin\left(\mu+\frac{\pi}{9}\right)-\sin\mu+\cos\left(\frac{\pi}{18}\right)\cdot\left(1-\frac{\pi}{9}\cdot\sqrt{3}\right)\right]\right\}
\end{aligned} \tag{3-52}$$

The last term related to *k* in the above equations captures the dynamics of the line current caused by the load current variation.

It should be noticed here that the current expression in (3-51) is in a different *dq* frame than the one defined for voltage. Since the input voltage source has *– /9* as the initial angle when deriving these equations, the initial angle of T_{dq}^{9} also has to be set as *– /9* also, which means the final currents on the *dq*-axes should be

$$\begin{bmatrix}\overline{i_{ds}}\\ \overline{i_{qs}}\end{bmatrix} = \begin{bmatrix}\cos\left(-\frac{\pi}{9}\right) & -\sin\left(-\frac{\pi}{9}\right)\\ \sin\left(-\frac{\pi}{9}\right) & \cos\left(-\frac{\pi}{9}\right)\end{bmatrix}\cdot\begin{bmatrix}\overline{i_d}\\ \overline{i_q}\end{bmatrix} \tag{3-52}$$

To get the primary ac currents, the above currents must be multiplied by turns ratio n_i as

$$i_{dq,p} = n_i \cdot i_{dq,s} \tag{3-53}$$

The average model of nine-phase diode rectifier in *dq*-axes are then developed in MATLAB/Simulink using equations (3-43), (3-51), (3-52) and (3-53). Using the inverse Park transformation $(T_{dq}^{3})^{-1}$, the average model in the *abc*-axes can be derived.

3.6. Discussion of average model

A critical assumption of the average model derived in this chapter is that the commutation will be completed within one "switching period". In equations (3-11) and (3-40), this assumption sets the upper bound limitation of the equivalent commutation inductor value for three-phase diode rectifier as

$$L_c < \frac{\left(1-\cos 60^\circ\right)\cdot\sqrt{3}\cdot V}{2\cdot\omega\cdot i_{dc0}} = \frac{\sqrt{3}\cdot V}{4\cdot\omega\cdot i_{dc0}} \tag{3-54}$$

where L_c is the equivalent commutation inductor. This criterion can usually be satisfied in the three-phase diode rectifier under normal operation conditions. The typical commutation angle at full load is from 20° to 25° [38].

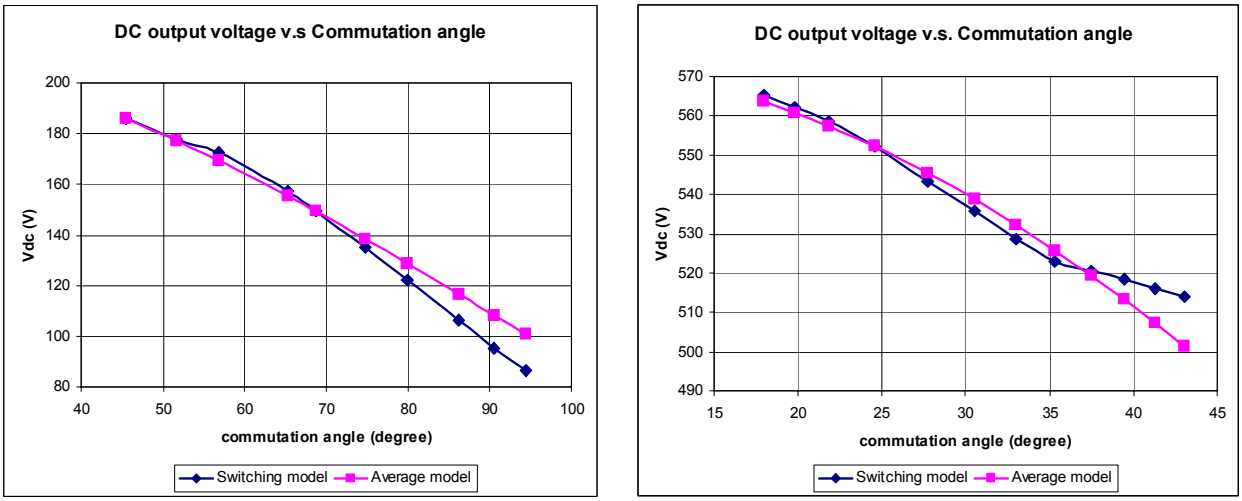
For the nine-phase diode rectifier, the limitation of the equivalent commutation inductance is

$$L_c < \frac{\left(1-\cos 20^\circ\right)\cdot V\cdot\sin\left(\pi/9\right)}{\omega\cdot i_{dc0}} = \frac{0.0206\cdot V}{\omega\cdot i_{dc0}}. \tag{3-55}$$

When the rectifier is applied in an aircraft power system, the line frequency varies from 360Hz to 800Hz. If the load is assumed be to 100kW and the RMS value of the

input voltage to be 230V, the limitation for equivalent commutation inductance is only 4.88μH when line frequency is 800Hz. However, the secondary inductor of the autotransformer is usually required to be very small to reduce the harmonics, which meets the requirement most of the time.

When the equivalent commutation inductance is beyond the maximum value in (3-54) and (3-55), the average model is not theoretically valid. The difference between the average model and the switching model is shown in Figure 3-7 at different commutation angles. It can be seen that the difference becomes larger when commutation angle is higher.



(a) **three-phase diode rectifier** **(b) nine-phase diode rectifier**

Figure 3-7 DC output voltage vs. Commutation angle

The mathematical derivation method of the average model has certain limitations. First, no capacitance is modeled into the rectifier. The average model of the rectifier with line capacitors should be re-derived. In [44], an average model for three-phase diode rectifier with line capacitors is derived. Secondary, if multiple branches are in parallel

with the rectifier, the equations of its average model become more complicated, unless the paralleled impedance is much larger than that of the rectifier so that it can be ignored. Additionally, this model cannot be used when the system stability is investigated from ac side of the power system, because the generator and the feeder cannot be modeled separately in the average model anymore.

3.7. Simulation result

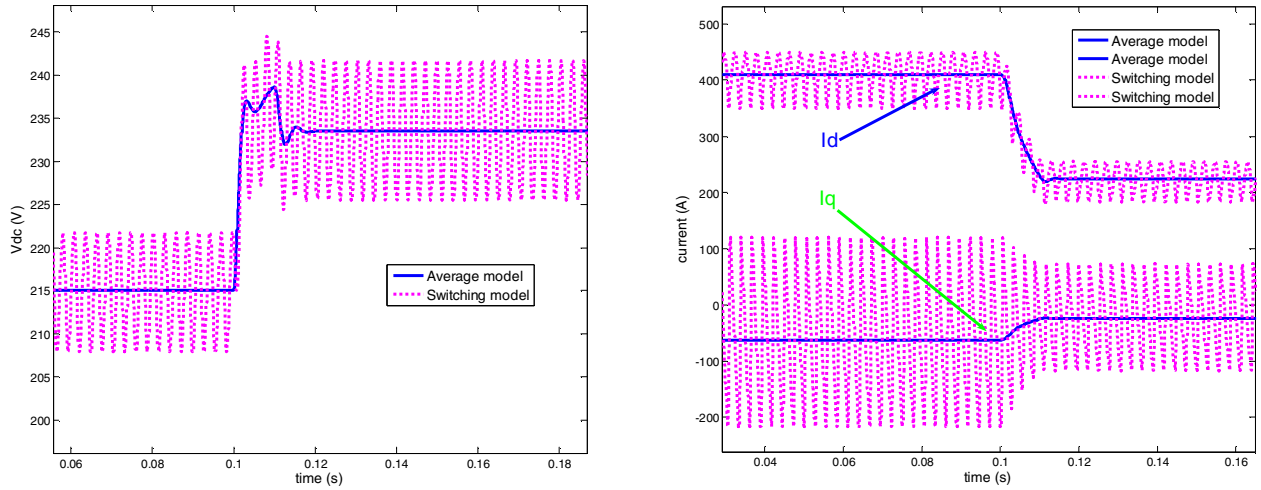
The average models for the three-phase and nine-phase diode rectifiers are implemented in MATLAB/Simulink. The output filter inductor is included in the average model, and its current is the only state variable in the MATLAB model. The feeder's inductance has to be included as the parameter for equations.

The three-phase diode rectifier will be utilized for both 60Hz in ac power system and high-frequency situations like aircraft power systems, while the nine-phase diode rectifier is usually only used in aircraft power systems. Figure 3-8 gives the simulation results of the three-phase and nine-phase diode rectifiers compared with the detailed switching model in Saber under the system parameters listed in Table 3-1. More comprehensive simulation results will be given in Chapter 4.

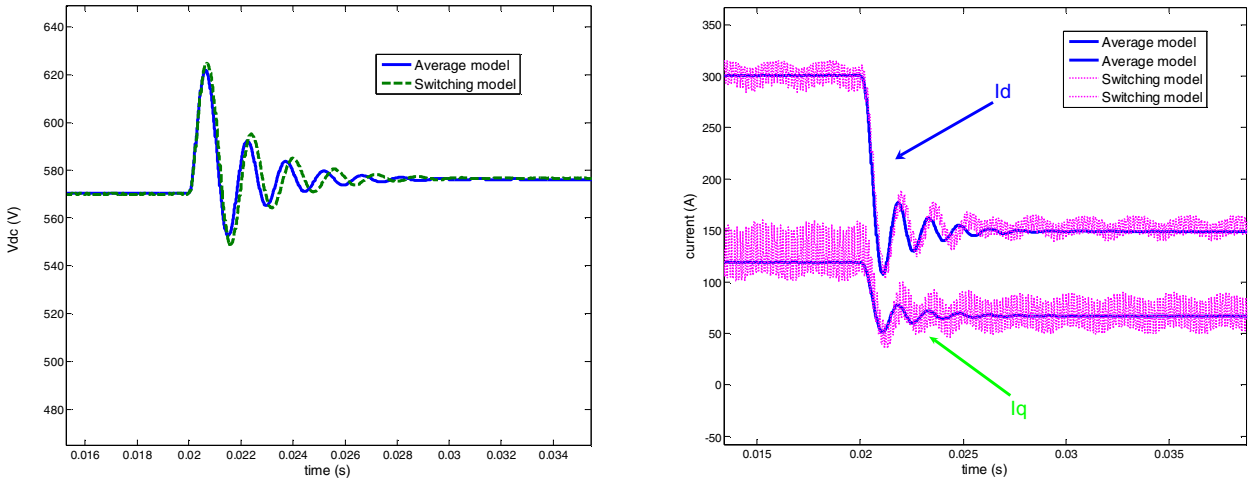
Table 3-1 Simulation parameters

Model	V_{rms}	L_p	L_s	R_p	R_s	f	R_{load}
3-phase	110V	30μH	- - -	10mΩ	- - -	60Hz	0.7Ω
9-phase	230V	10 μH	1.6μH	0.2mΩ	7.6mΩ	400Hz	2.11Ω

The average models have been implemented in Saber also. Unlike the model in MATLAB, the average model does not include the output filter inductor. The output signal of the average model in Saber is the averaged output voltage, which is equation (3-16). This model is suitable to get the small signal of the rectifier only, without the impedance of the output filter.



(a) **three-phase diode rectifier**



(b) **nine-phase diode rectifier**

Figure 3-8 Simulation result

3.8. Summary

In this chapter, the dynamic average models of the three-phase and nine-phase diode rectifier have been developed using mathematical derivation. The load current is modeled using its first-order Taylor series expansion during the entire switching period, which could improve the system's transient behavior over the existing model. When deriving average models, the commutation angle is first calculated using a line current expression, followed by averaging the dc side voltage and ac currents in the *dq*-axes.

The diode parameters are also taken into consideration in the average model as the forward voltage drop and on-state resistor. This improves the steady-state accuracy of the average model. For the nine-phase diode rectifier, the feeder's inductor before the autotransformer is contributed to the commutation period and should not be ignored. Because of the nonlinearity of the secondary current, the feeder's inductor needs to be referred to the secondary side by the transfer function of the primary and the secondary currents of the autotransformer during the commutation period.

The average model is only valid when the current transfer can be finished within one switching period, which is the normal case for either the three-phase or nine-phase diode rectifier.

CHAPTER 4 TIME DOMAIN EVALUATION OF AVERAGE MODEL FOR DIODE RECTIFIER

4.1. Introduction

In Chapter 3, average models for three-phase and nine-phase diode rectifiers with an improved ac dynamic and dc behavior are derived. The load current is modeled by its first-order Taylor series expansion. While average models of three-phase diode rectifiers have already been developed, this study assumes the load current in different ways. In this chapter, two additional average models of the diode rectifier are introduced: one is denoted as a "static model" because it does not model the dynamics in the rectifier, and the other one is denoted as a "dynamic model" which improves the dynamic behavior to some extent [41]. These two models were initially developed for three-phase diode rectifiers. In this work, they are expended for nine-phase diode rectifiers using the same procedure. This chapter compares the time domain of these models with that of the average model described in chapter 3, denoted as an "improved model" for the sake of simplicity.

A detailed switching model of a nine-phase diode rectifier is developed in Saber as a benchmark for the comparison. The output dc voltage and ac currents of each average model are compared. To have a clear and comprehensive comparison, quantified results are necessary. The square error of the waveforms between the switching model and each

average model are calculated under the steady-state and the transient conditions. Thereafter the validation of each average model is analyzed.

A 2kW prototype of a nine-phase diode rectifier is built to verify the average model. The comparison between the average model, the switching model and real hardware is presented at the end of this chapter.

4.2. Overview of different average models

Two different average models have been developed in the past, denoted as the "static model" and the "dynamic model" [41]. It can be concluded from its name that the static model captures only the steady state characteristic of the rectifier. The dynamic model improves upon the static model by considering the load current change during the derivation. The "improved model" developed in Chapter 3 is also a dynamic model, with the improvement on dc and ac transient behavior.

4.2.1. Static model

The static model is the simplest model among the three average models. In this model, the difference from the improved model is:

1. Load current is constant during one switching period;
2. Parasitic resistor of the ac line inductance is ignored;
3. Diodes are modeled as ideal switches—no forward voltage drop and no on-state resistor.

When the load current stays constant during one switching period, the dynamic characteristic of the diode rectifier is ignored. The system dynamic behavior is completely determined by the output filter. The second and third differences listed above are related to the steady state error in the static model. In order to stay consistent with the developed models in the existing literature, these parasitic parameters are not modeled for the static model, with the exception of the parasitic resistor of the output filter inductor. For the static model of nine-phase diode rectifiers, the feeder's parameters, including the inductance and parasitic resistances, are also excluded in order to investigate their influence on the model's accuracy.

The detailed derivation of the static model for the three-phase diode rectifier is given in [41]. The calculation of the commutation angle is the same as the calculation in Chapter 3, but the state space equation of the output current is modified to be

$$\frac{di_{dc}}{dt} = \frac{\frac{3\sqrt{3}}{\pi}\cdot V - \left(\frac{3}{\pi}\cdot \omega L + \mathrm{R_{dc}}\right)\cdot i_{dc0} - V_{load}}{L_{dc}} . \tag{4-1}$$

The equations for ac line currents are

$$\begin{aligned} \overline{i_{d,com}} &= \frac{3\sqrt{2}}{\pi}\cdot i_{dc0}\cdot\cos\mu - \frac{3\sqrt{6}}{2\pi}\cdot\frac{V}{\omega L_c}\cdot\left(\cos\mu - \frac{\cos 2\mu}{4} - \frac{3}{4}\right) \\ \overline{i_{q,com}} &= -\frac{3\sqrt{2}}{\pi}\cdot i_{dc0}\cdot\sin\mu - \frac{3\sqrt{6}}{2\pi}\cdot\frac{V}{\omega L_c}\cdot\left(-\sin\mu + \frac{\mu}{2} + \frac{\sin 2\mu}{4}\right) \end{aligned} . \tag{4-2}$$

Using the same derivation procedure, the static model for the nine-phase diode rectifier is also developed as

$$\frac{di_{dc}}{dt}=\frac{\frac{18}{\pi}\cdot V\cdot\sin\left(\frac{\pi}{9}\right)-\left(\frac{9}{\pi}\cdot\omega L+\mathrm{R_{dc}}\right)\cdot i_{dc0}-V_{load}}{L_{dc}}$$

$$\begin{aligned}\overline{i_d}=&\frac{9}{\pi}\cdot\frac{\sqrt{2}}{3}\cdot\left\{\frac{1}{16}\cdot\frac{\mathrm{V}}{\omega\mathrm{L_c}}\cdot\left[\left(6\cdot\sin\left(\frac{\pi}{9}\right)-\sqrt{3}\right)\cdot\left(\sin(2\mu)-4\cdot\sin\mu+2\mu\right)+\left(1-2\cos\left(\frac{\pi}{9}\right)\right)\times\right.\\&\left.\left(\cos 2\mu-4\cdot\cos\mu+3\right)+\left[\sin\mu+\sin\left(\mu+\frac{\pi}{9}\right)-2\cdot\sin\left(\mu+\frac{\pi}{6}\right)\cdot\cos\left(\frac{\pi}{18}\right)\right]\cdot\mathrm{i_{dc0}}\right\}\end{aligned}$$

$$\begin{aligned}\overline{i_q}=&\frac{9}{\pi}\cdot\frac{\sqrt{2}}{3}\cdot\left\{\frac{1}{16}\cdot\frac{\mathrm{V}}{\omega\mathrm{L_c}}\cdot\left[\left(2\cdot\cos\left(\frac{\pi}{9}\right)-1\right)\cdot\left(2\mu-\sin(2\mu)+4\cdot\sin\mu\right)+\left(6\sin\left(\frac{\pi}{9}\right)-\sqrt{3}\right)\times\right.\right.\\&\left.\left.\left(-\cos 2\mu+4\cdot\cos\mu-3\right)+\left[2\cos\left(\frac{\pi}{18}\right)\cdot\cos\left(\mu+\frac{\pi}{6}\right)-\cos\mu-\cos\left(\mu+\frac{\pi}{9}\right)\right]\cdot\mathrm{i_{dc0}}\right\}\end{aligned}$$

(4-3)

The static model is built in MATLAB/Simulink for the three-phase and the nine-phase diode rectifiers respectively for comparison.

4.2.2. Dynamic model

This dynamic average model is proposed in [41]. In contrast with the static model, the load current variation within one switching period is considered as Δi_{dc} when deriving the output dc voltage. Nonetheless, this variation is ignored when deriving ac line currents and the commutation angle. The dynamic model of the three-phase diode rectifier is

$$\begin{aligned}\mu&=\arccos\left(1-\frac{2\cdot\omega L_c\cdot i_{dc}}{V\cdot\sqrt{3}}\right)\\\frac{di_{dc}}{dt}&=\frac{\frac{3\sqrt{3}}{\pi}\cdot V-\left(\frac{3}{\pi}\cdot\omega L+\mathrm{R_{dc}}\right)\cdot i_{dc}-V_{load}}{L_{dc}+2\cdot L_c}\end{aligned}$$

(4-4)

This model is extended to the nine-phase diode rectifier in this work, which is

$$\mu = a\cos\left(1 - \frac{\omega \cdot L_c \cdot i_{dc}}{V \cdot \sin\left(\frac{\pi}{9}\right)}\right)$$
$$\frac{di_{dc}}{dt} = \frac{\frac{18}{\pi} \cdot V \cdot \sin\left(\frac{\pi}{9}\right) - \left(\frac{9}{\pi} \cdot \omega L_c + \mathrm{R_{dc}}\right) \cdot i_{dc} - V_{load}}{L_{dc} + 2L_c} \quad . \tag{4-5}$$

The equations for ac line current are exactly the same as equation (3-25) for three-phase and equation (4-3) for nine-phase diode rectifier. The dynamics are not included in the ac line current equations in the dynamic model.

Here we will explain why the different load current model will result in different average models. In the dynamic model, the load current is in the expression of both μ and the state space equation. Reference [44] proves that μ is only related to the average load current during the commutation period and the current derivative has no influence on it. Therefore, the load current in μ's expression should be the averaged load current during the commutation, while the load current in the state space equation is the initial load current in the switching period. If the load current is modeled using its first-order Taylor's Series expansion as in the improved model, their difference can be seen clearly from Figure 4-1 as i_{dcs} versus i_{dc0}.

In the dynamic model, it is assumed that i_{dcs} is equal to i_{dc0}. In the improved model, the difference between i_{dcs} and i_{dc0} is reflected by the load current model. This changes the boundary conditions of the ac currents at the beginning and at the end of the commutation and conduction period, which will influence the state equation for current of the output filter inductor.

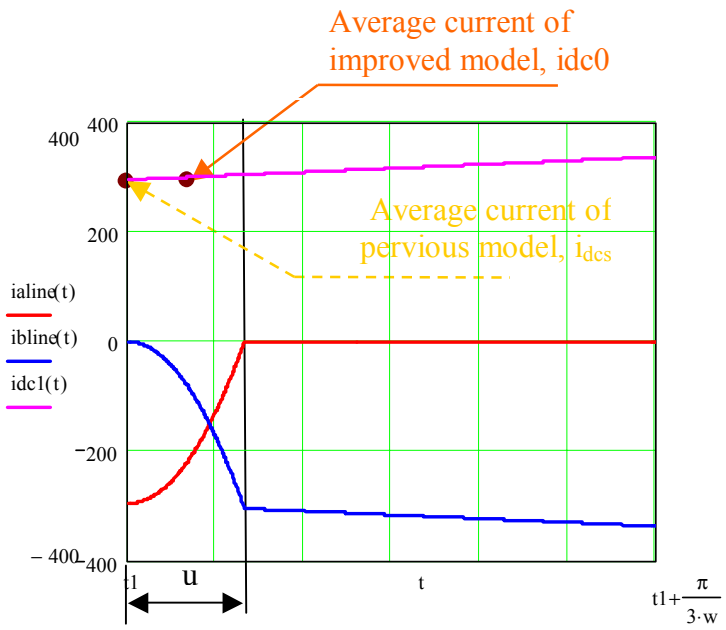


Figure 4-1 Definition of average current

4.3. Switching model

The switching models of three-phase and nine-phase diode rectifiers are the benchmark circuits for average model evaluations in the time domain, which are implemented using Saber software.

It is straightforward to develop the switching model for three-phase diode rectifier in Saber. The built-in diode model from Saber is used for the diode rectifier. The ac currents are transformed to *dq*-axes by *dq*-transformation, which is implemented in Saber using the MASTER language [63].

When modeling the nine-phase diode rectifier, modeling the autotransformer is the most critical issue. A pseudo-electric representation is used for a magnetic circuit of the autotransformer, which is shown in Figure 4-2 [64].

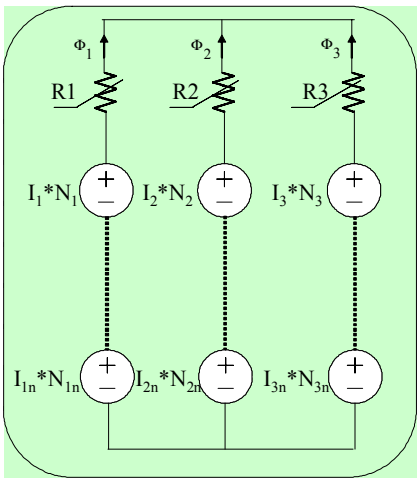


Figure 4-2. Magnetic model of autotransformer

In Figure 4-2, resistances R_1, R_2 and R_3 represent the reluctances of the magnetic paths for each core leg i while $N_{in} \cdot I_{in}$ denotes the MMF of the winding "in", with i =1, 2, 3 and n the number of the corresponding winding in every leg i. Modeled in this way, the three-phase autotransformer uses a fully coupled magnetic structure, which is very close to the real hardware.

The assumptions used to derive the average model are also valid for this switching model. The primary inductance is set to be zero for the autotransformer, and secondary inductances for the nine phases have the same value, which is different from the real hardware. A linear core is used in the autotransformer model in Saber. The purpose of this switching model is to investigate the precision of the average procedure based on

these assumptions. The comparison between the average model and real hardware is discussed in the following section.

4.4. Time domain evaluation

In the static and dynamic models, the dynamic of the diode rectifier is either not considered or partially considered. Moreover, most of the parasitic parameters are not included into these two models. Therefore, they have simpler forms than the improved model. In the following section, these three models, the static model, dynamic model and improved model, are compared using the detailed switching model as the benchmark under both steady state and transient conditions. This could provide guidance for application of the average model concerning the trade off between the model's complexity and precision.

4.4.1. Definition of evaluation method

Besides comparing the waveforms of different models, quantified results for comparison are needed for better illustration. The square error between switching and average model is defined as

$$e = \sum_{t=t_o}^{t_n} \left[x_{sw}(t) - x_{avg}(t) \right]^2 , \tag{4-6}$$

where t_0 and t_n are the beginning and the end time of comparison region. x_{sw} represents the voltage or current of the switching model, and x_{avg} is the voltage or current of

average models. The average model is closer to the switching model if *e* becomes smaller. In this work, the dc output voltage and the ac current in *dq*-axes are compared.

The challenge of the comparison lies in the different simulation parameters of the switching model and the average model. Based on the complex structure of the switching model, variable simulation step must be used in Saber to make the simulation converge. In all average models, the vector written to the workspace of MATLAB is sampled by fixed frequency. Consequently, the calculation in (4-6) cannot be performed directly because the time vectors from Saber and MATLAB do not match point by point.

Interpolation is used to solve this problem. Since the simulation step for the average model is fixed, this value is set as the maximum simulation step for the switching model. This means that the switching model will always have more data points than the average model. Weighted interpolation is applied to the switching model to get new data in the switching model corresponding to the ones in average model, as illustrated in Figure 4-3.

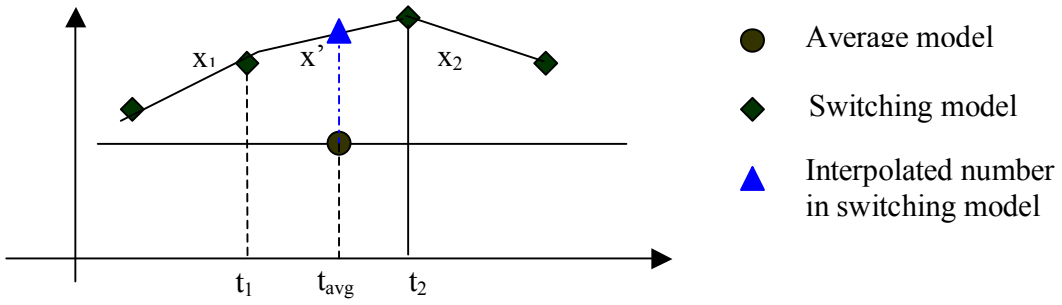


Figure 4-3. Interpolation method

The new value at the interpolated point is calculated as

$$x' = \frac{x_1 \cdot (t_2 - t_{avg}) + x_2 \cdot (t_{avg} - t_1)}{t_2 - t_1}. \tag{4-7}$$

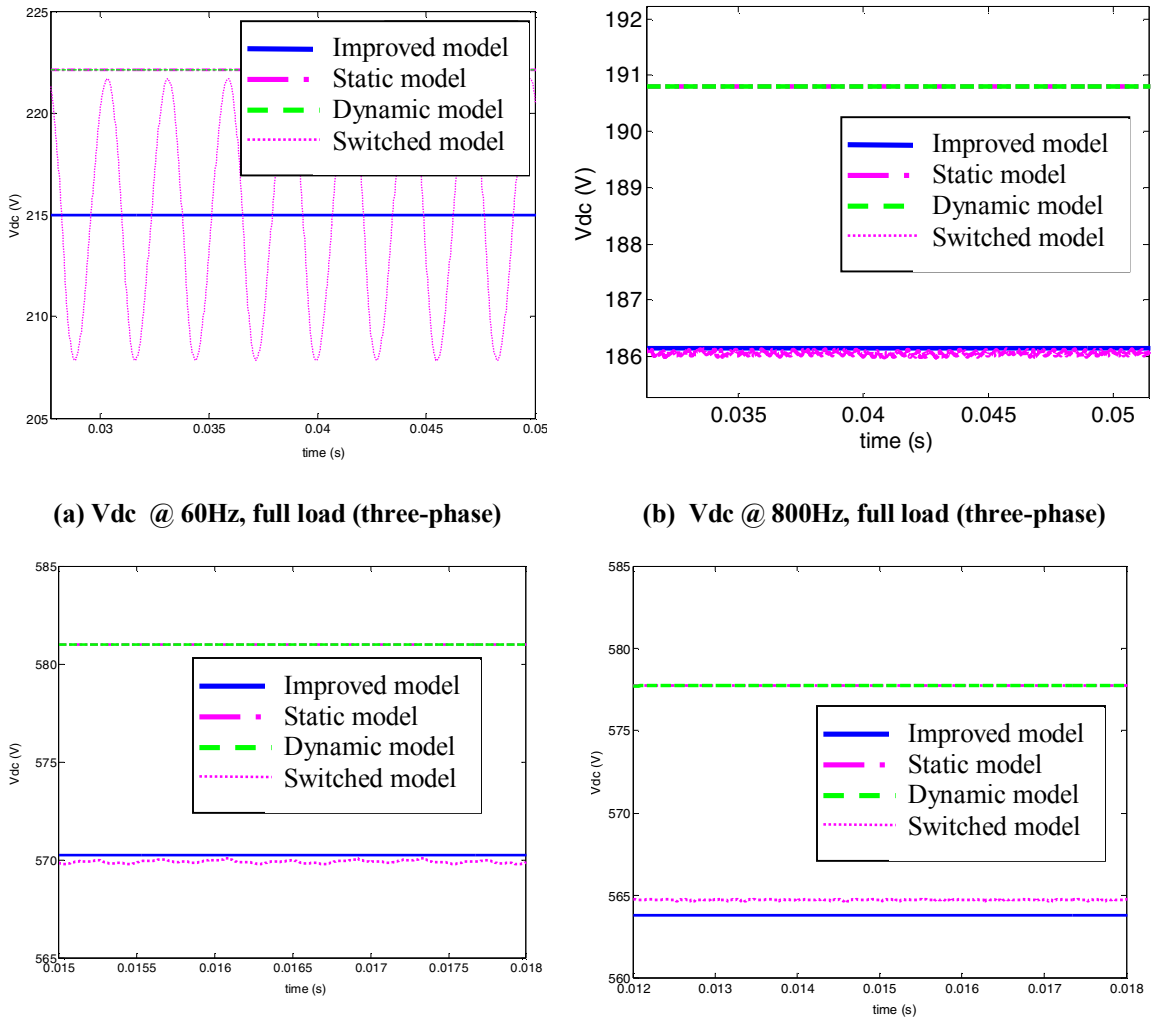
In Saber simulation, the simulation step is required to be a very small number for good accuracy. The waveforms of the switching model after interpolation are almost exactly the same as the waveforms of the original switching model.

4.4.2. Steady state evaluation

The steady state evaluation is performed for both the three-phase and the nine-phase diode rectifier. For the three-phase diode rectifier, the line frequency is chosen to be 60Hz, 360Hz, 600Hz and 800Hz because of the wide application. The nine-phase diode rectifier is usually installed on an aircraft power system, which has a variable frequency that ranges from 360Hz to 800Hz.

The capacity of the diode rectifier is assumed to be 50kW (0.7Ω resistive load) for the three-phase diode rectifier and 100KW (2.11Ω resistive load) for the nine-phase diode rectifier. The models under different load conditions from full load to 10% load are simulated here.

Under the steady state, the static model and the dynamic model are identical to each other. The waveforms of the dc output voltage of the three-phase and the nine-phase diode rectifiers under one typical condition are shown in Figure 4-4.



(a) Vdc @ 60Hz, full load (three-phase)

(b) Vdc @ 800Hz, full load (three-phase)

(c) Vdc @ 400Hz, full load (nine-phase)

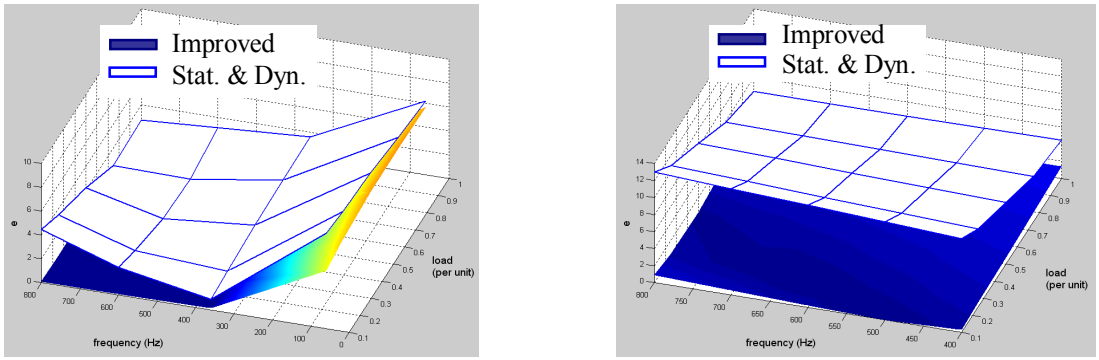
(d) Vdc @ 800Hz, full load for (nine-phase)

Figure 4-4. DC output voltage under different conditions @ steady state

The complete comparison results of the dc output voltage for the three-phase and the nine-phase diode rectifier are given in Figure 4-5. The x-axis "load" is per unit value, which means that it is one when full load condition is simulated. From that figure, it can be seen that the output dc voltage of the improved model has the least square error compared with the other two models under all conditions. For the three-phase diode rectifier, the error between the improved model and the switching model is relatively

large when the line frequency is 60Hz and it becomes smaller in the high-frequency range. For each frequency, the error does not change much with different loads. However, for the static model, the error changes significantly with the load condition. The reason for this is that the improved model has already taken all the parasitic parameters into consideration, including the voltage drop on the ac line resistor. In contrast, in the static model this voltage drop, which is almost linear with the load current, is ignored.

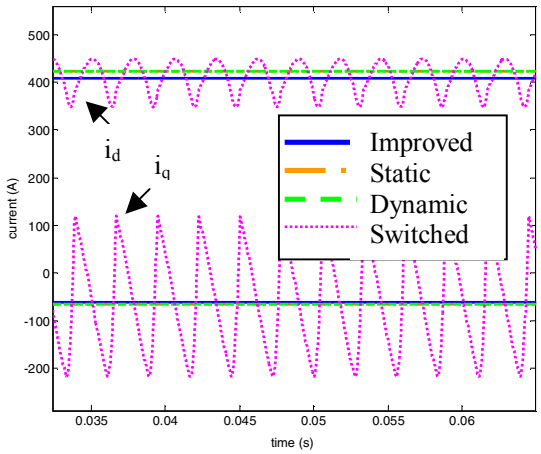
This phenomenon is not the same for the nine-phase diode rectifier as it is for the three-phase diode rectifier. For all average models, the error will change with the load condition and the line frequency. This is because the feeder's inductance and resistance are approximated to the averaged value in the improved model, and they are subject to the load condition.



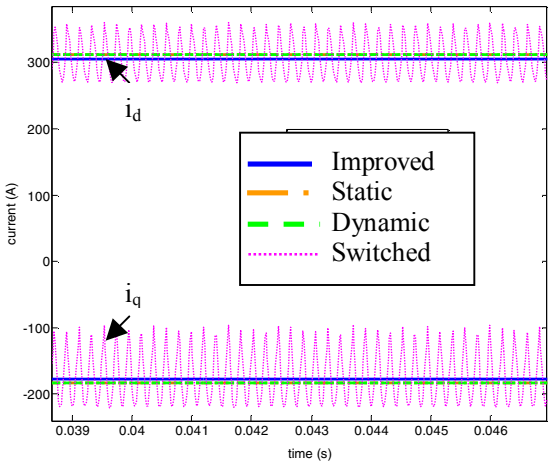
(a) Vdc (three-phase) **(b) Vdc (nine-phase)**

Figure 4-5. Quantified comparison result for dc output voltage @ steady state

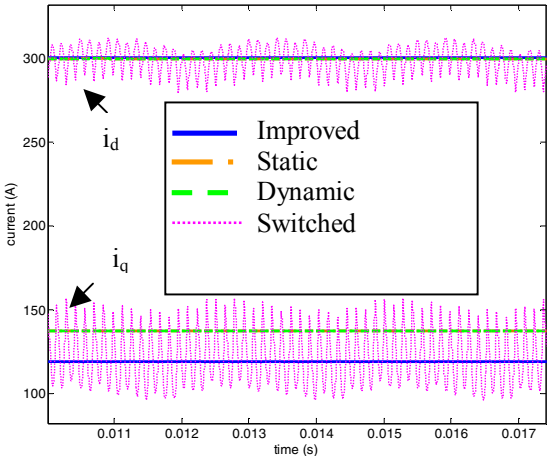
The typical waveforms of the ac currents in *dq*-axes for the three-phase diode rectifier are given in Figure 4-6 (a) (b), while Figure 4-6 (c) (d) shows the waveforms for the nine-phase diode rectifier. The complete quantified comparison results are given in Figure 4-7.



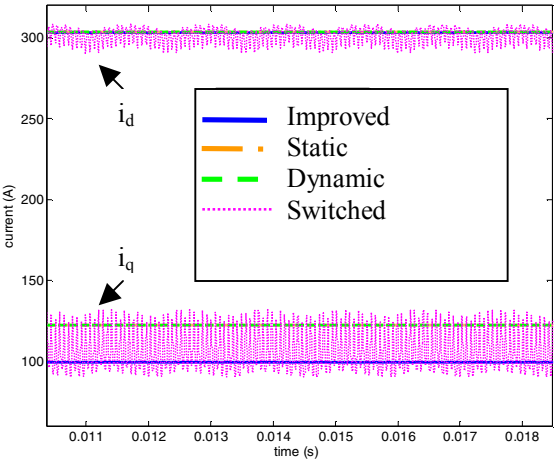
(a) idq @ 60Hz, full load (three-phase)



(b) idq @ 800Hz, full load (three-phase)

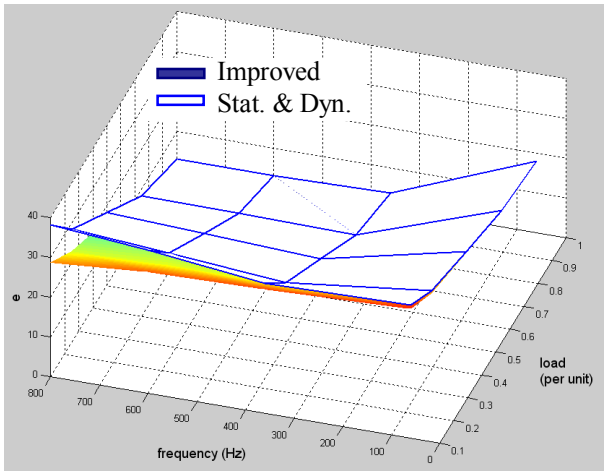


(a) idq @ 400Hz, full load (nine-phase)

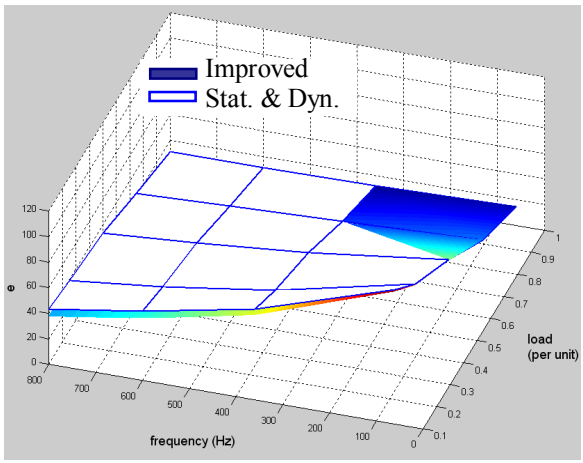


(b) idq @ 800Hz, full load (nine-phase)

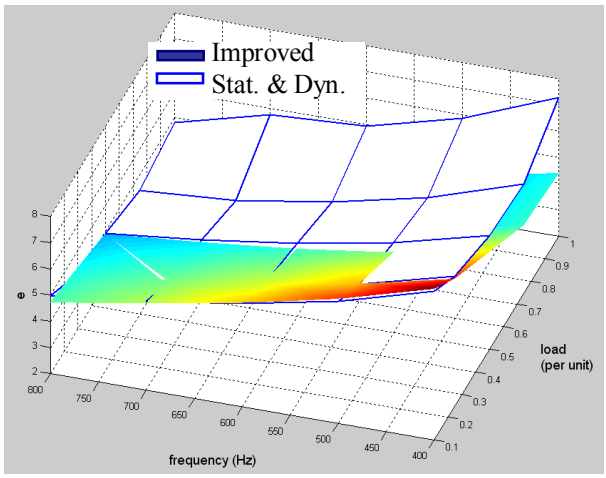
Figure 4-6. AC line current for the nine-phase diode rectifier @ steady state



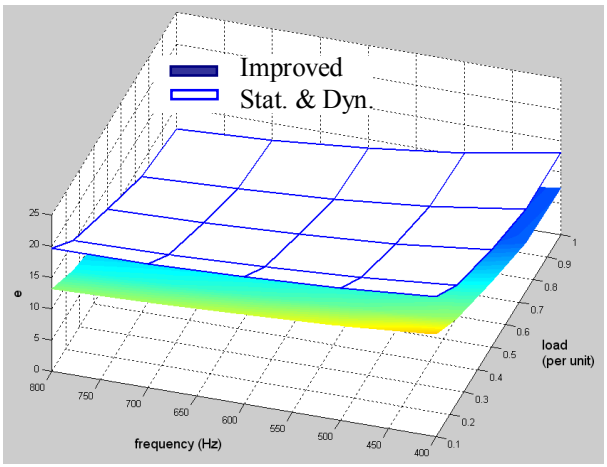
(a) id (three-phase)



(b) iq (three-phase)



(c) id (nine-phase)



(d) iq (nine-phase)

Figure 4-7. Quantified comparison result for ac currents in *dq*-axes @ steady state

It can be seen that the improvement of the improved model is limited for the three-phase diode rectifier at the steady state, while the improvement is significant for the nine-phase diode rectifier. The reason for this is that neglecting the feeder's inductance when calculating the commutation inductance in the nine-phase diode rectifier causes significant steady state error for the average model.

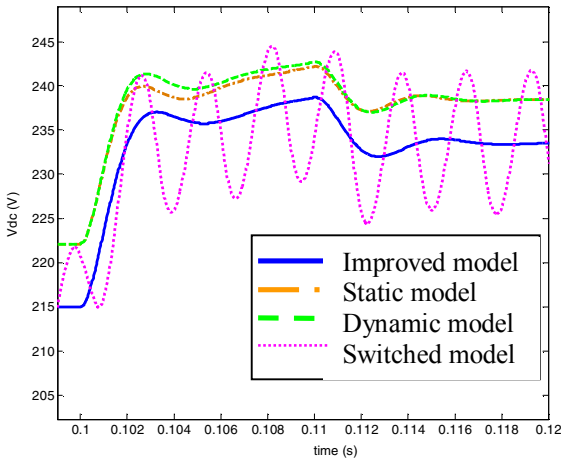
Working from the above statement, , the following can serve as guidance to make the trade-off between the different average models: when the average model is used in the

system simulation to reduce the simulation time or make the system simulation converge, the static model is enough for the three-phase diode rectifier if the steady state error requirement is not strict. For the nine-phase diode rectifier, the improved model should be chosen to achieve the precision in the modeling work.

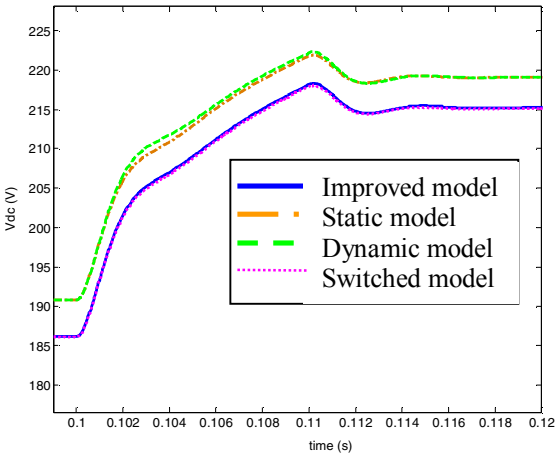
4.4.3. Transient evaluation

In the steady state evaluation, the effect of the parasitic parameters on the average models is discussed. The major difference between the three models, however, lies in modeling the load current in different ways, which changes the rectifier's dynamic response. In this section, the transient behavior of the three average models is compared.

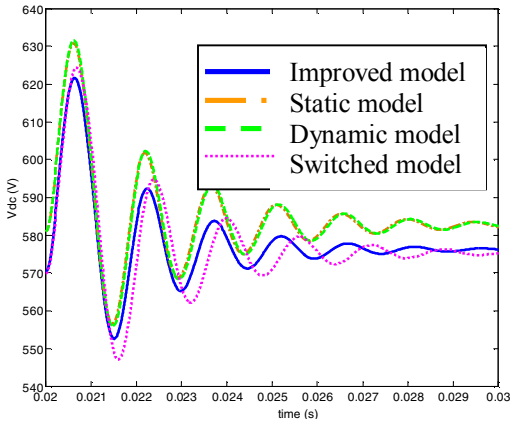
Typical waveforms showing the transient behavior of all average models are given in Figure 4-8 for the dc output voltage and Figure 4-9 for ac line currents in *dq*-axes. During the transient, the load changes from full-load to half-load conditions within 10ms for the three-phase diode rectifier and within 1ms for the nine-phase diode rectifier.



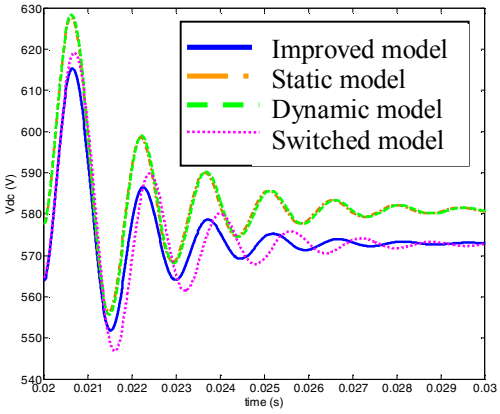
(a) Vdc @ 60Hz (three-phase)



(b) Vdc @ 800Hz (three-phase)

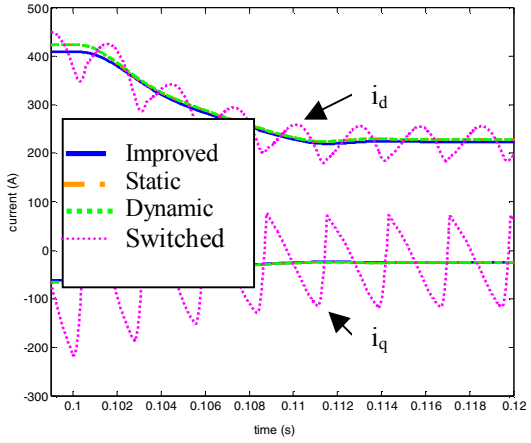


(c) Vdc @ 400Hz (nine-phase)

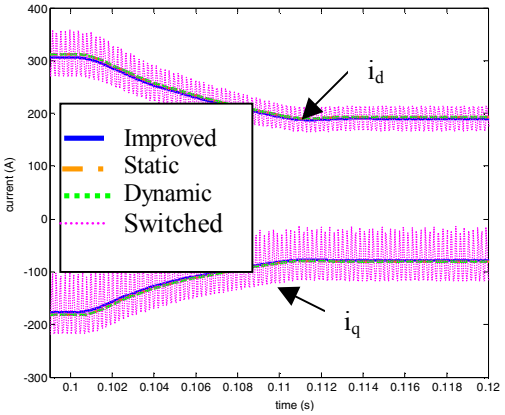


(d) Vdc @ 800Hz (nine-phase)

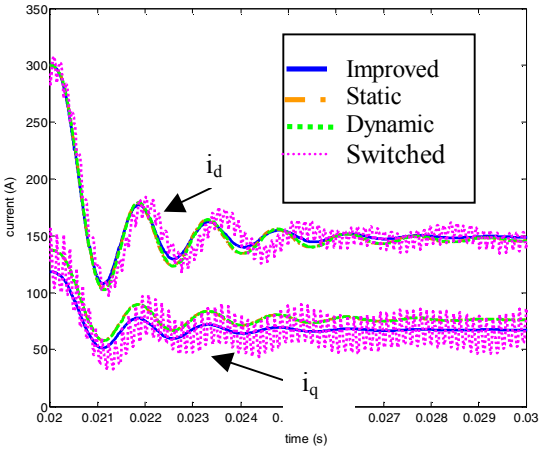
Figure 4-8 DC output voltage @ transient



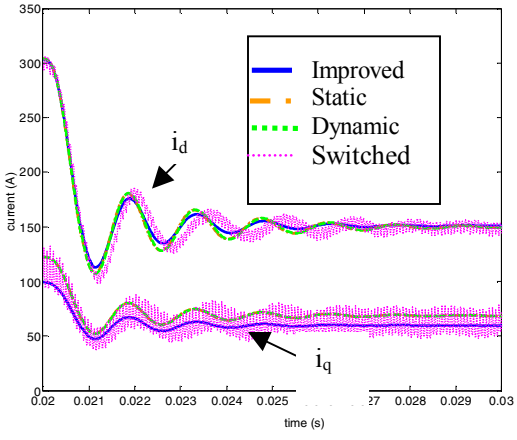
(a) idq @ 60Hz (three-phase)



(b) idq @ 800Hz (three-phase)



(c) idq @ 400Hz (nine-phase)



(d) idq @ 800Hz (nine-phase)

Figure 4-9. Ac line current for nine-phase diode rectifier @ full load to half load

These figures show that the improved model best matches the switching model. However, for the nine-phase diode rectifier, there is still some discrepancy between the improved model and the switching model. The reason for this discrepancy is that the equivalent commutation inductance of the diode rectifier is calculated as the averaged equivalent secondary inductance of the autotransformer when deriving the average model. In other words, in the average model it is assumed that the commutation angle is the same for every switching period. In the switching model, the commutation angle is different due to the feeder's inductance. To prove this, another switching model is developed in Saber by modeling the total equivalent commutation inductance on the secondary side of the autotransformer. In the new switching model, the feeder's inductance is set to be zero, and the secondary inductance is the summation of the autotransformer's secondary leakage inductance and the equivalent averaged feeder's inductance referring on the secondary side. Figure 4-10 gives comparison results between the average model, the new and the original switching models. The discrepancy between the average model and the new model reduces significantly. It can be concluded that the discrepancy between the average model and the switching model exists mostly because of the approximation of the equivalent commutation inductance in the average model.

More simulations are performed on the models to give a comprehensive comparison among the models during the transient. For both the three-phase and the nine-phase diode rectifier, a transient occurs in which the load changes from full load to 10%, 25% and 50% load respectively (noted as 0.1, 0.25 and 0.5 in following figures) within 10ms (three-phase diode rectifier) or 1ms (nine-phase diode rectifier). The time span for calculating the square error between each average model and the switching model should

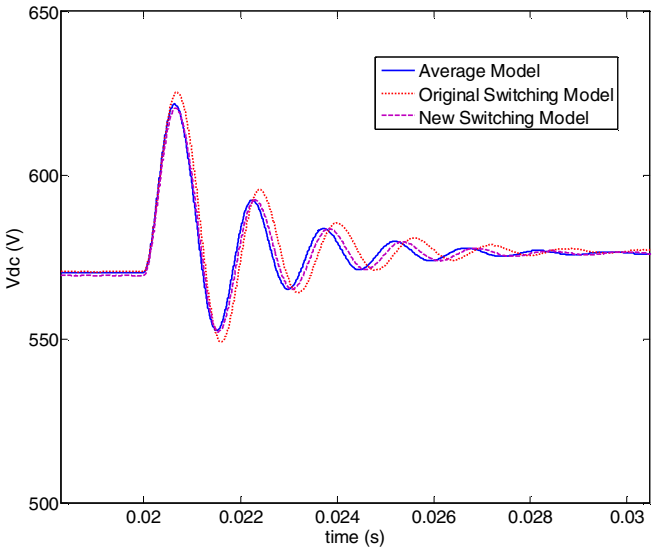
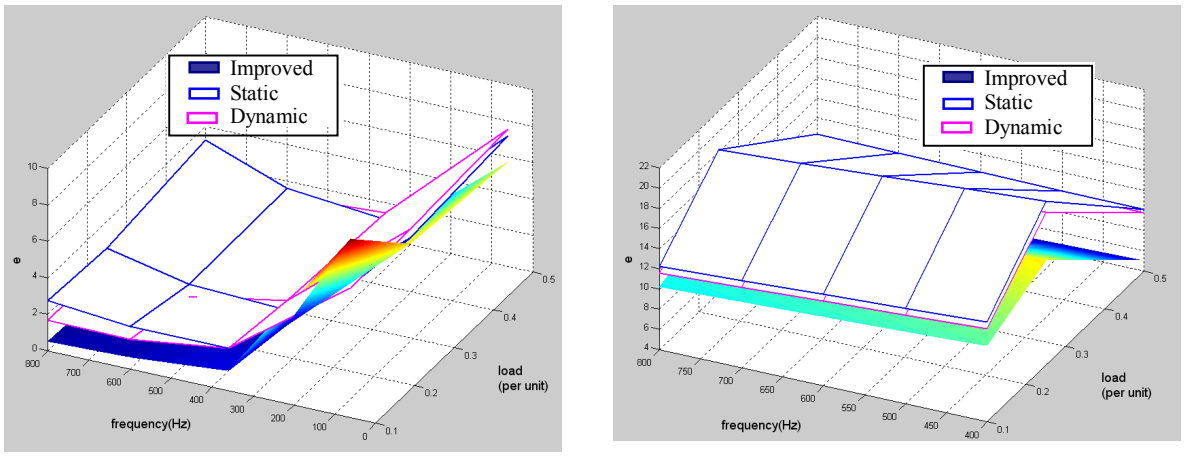


Figure 4-10. Approximation effect of the secondary inductance of autotransformer

be long enough so that the system transient responses are fully included into the calculation. According to the system parameters in this work, the time span is 0.02s for the three-phase diode rectifier and 0.01s for the nine-phase diode rectifier.

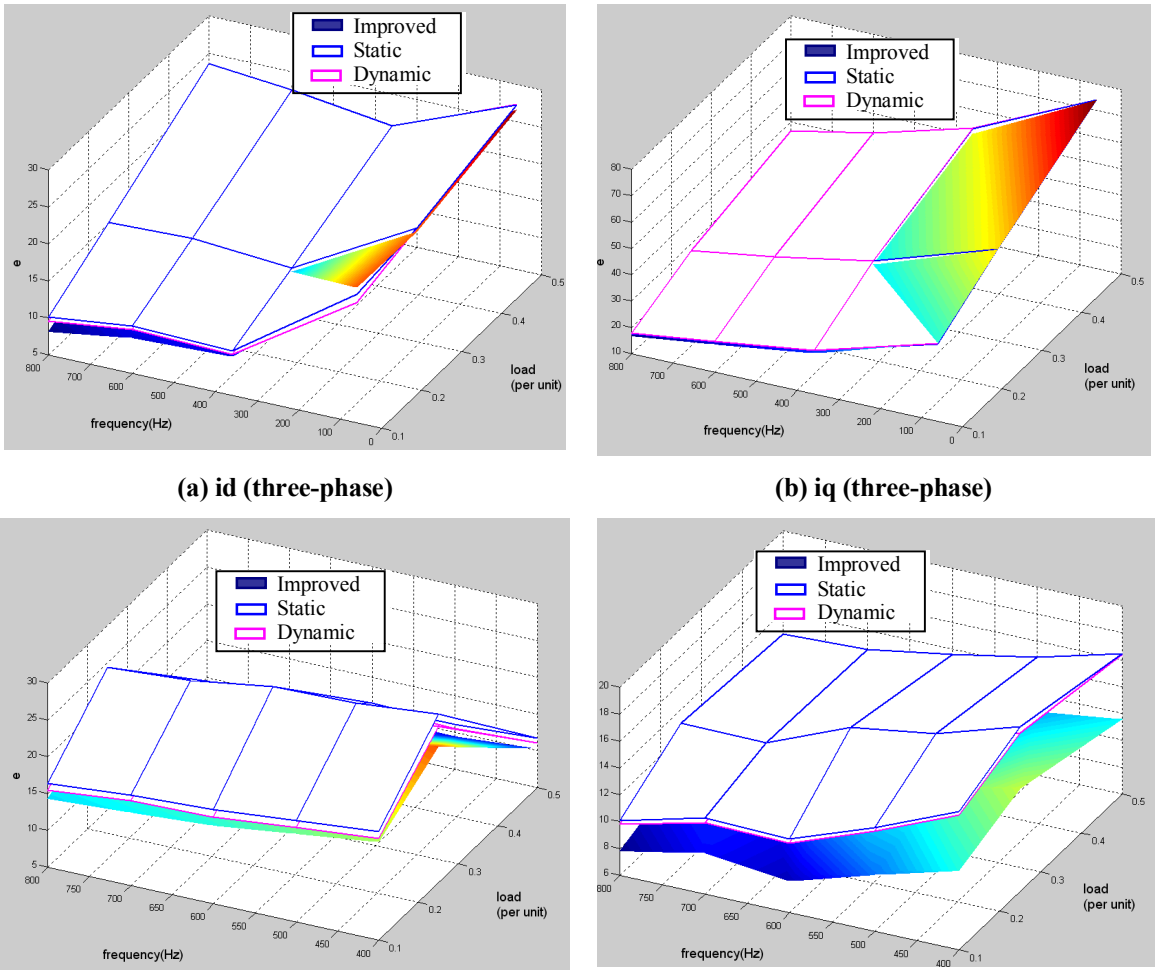
The quantified comparison results for dc output voltage during the transient are given in Figure 4-11.



(a) Vdc (three-phase) **(b) Vdc (nine-phase)**

Figure 4-11. Quantified comparison result for dc output voltage @ full load to half load

The improved model has the least square error among the three average models. The dynamic model improves the transient behavior of the static model but very limited.



(a) id (three-phase) **(b) iq (three-phase)**

(c) id (nine-phase) **(d) iq (nine-phase)**

Figure 4-12. Quantified comparison result for ac currents in *dq*-axes @ transient

Similar to the steady state condition, the improved model for the nine-phase diode rectifier during the transient has more effect on the model's precision than it does for the three-phase diode rectifier. There are two reasons for this: 1) the feeder's inductance of the autotransformer cannot be ignored, which is the same at the steady state; 2) the ratio between the commutation and conduction period in the nine-phase diode rectifier is usually higher than in the three-phase diode rectifier. This means that modeling the

dynamics in the commutation mode using the improved model becomes more important in the average modeling procedure.

Based on the analysis of the comparison among the models under both the steady state and the transient conditions, the static model could be used for the three-phase diode rectifier when the system modeling does not require very high precision for the average model. However, for the nine-phase diode rectifier, the improved model is necessary.

4.5. Experimental validation

A 2kW nine-phase diode rectifier with lower power rating is built for hardware verification, as shown in Figure 4-13. The diode rectifier is composed by MUR1520. To prevent the transformer core from saturating, the input voltage is limited up to 65V RMS. The average model is modified to have the same parameters for comparison.

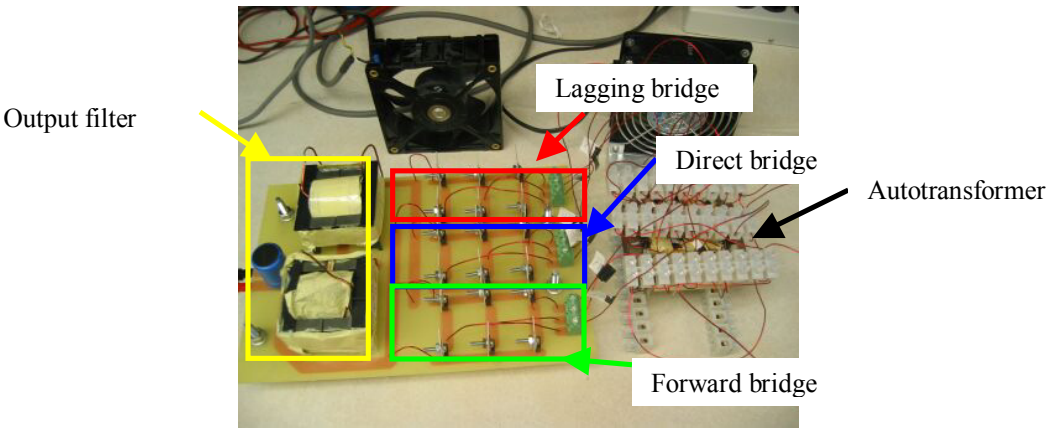
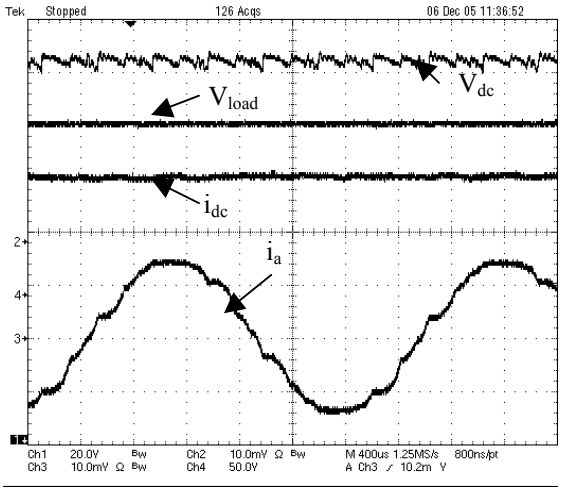


Figure 4-13. Prototype of the nine-phase diode rectifier

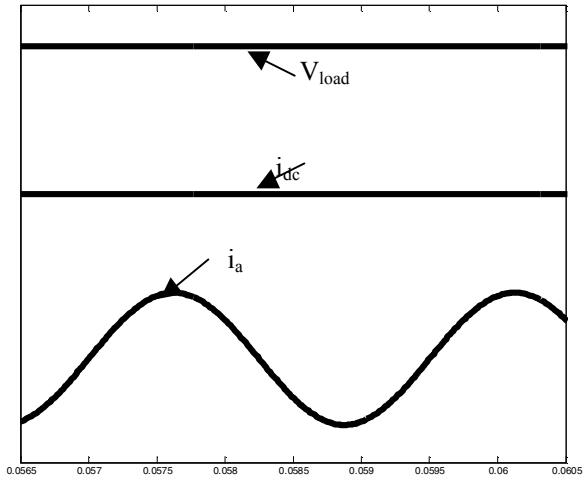
The system parameters for experiments are listed in Table 4-1. The input voltage is generated by an HP6834B ac power supply, and it is adjustable. MCT488 is used as the load, which is programmable equipment especially suitable for transient experiments.

Table 4-1 Hardware system parameters

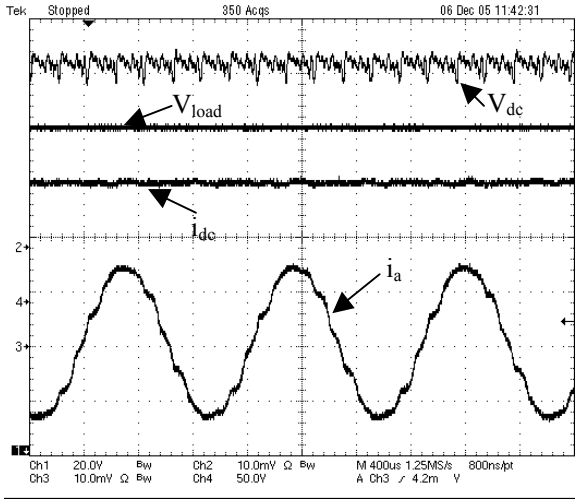
V_{in} (RMS)	L_c	R_{Lc}	L_{dc}	R_{dc}	C	R_{load}
65V	130μH	0.1Ω	3.6mH	240mΩ	470μF	22Ω



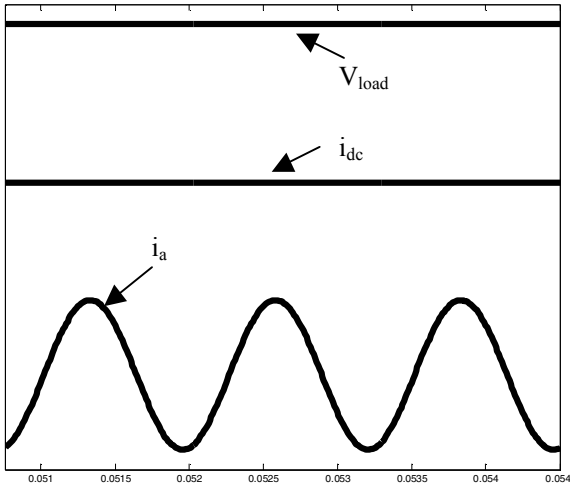
(a) hardware @ 400Hz



(b) improved model @ 400Hz



(c) hardware @ 800Hz



(b) improved model @ 800Hz

Figure 4-14. Hardware v.s. Improved model @ steady state

The nine-phase diode rectifier is tested under 400Hz and 800Hz. The results of a comparison of the hardware and the average model are given in Figure 4-14. In these two steady states, the output dc voltage V_{dc} is lower at 800Hz than at 400Hz. When the line

frequency goes higher, the equivalent commutation impedance becomes larger, resulting in more voltage drop.

From the above figures, it can be seen that the output dc voltage from the experiment is a little higher than the voltage from the average model. The primary leakage inductor of the autotransformer existing in the hardware causes the discrepancy, which is ignored in the average model. When the primary leakage inductance of the autotransformer exists, the commutation time is different for every current transfer instance because the current that is transferred are not the same. Figure 4-15 gives the current in each winding for one leg. We can see that the current change between every two switching periods is different. Fortunately, according to the strict harmonics requirement in the aircraft power system, the primary leakage inductance must be very small. Therefore, it can be ignored for average modeling.

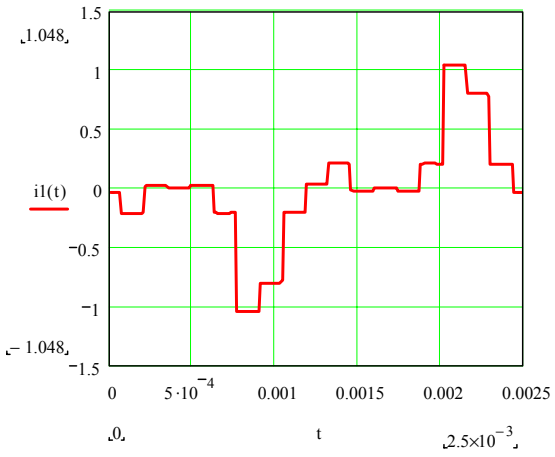
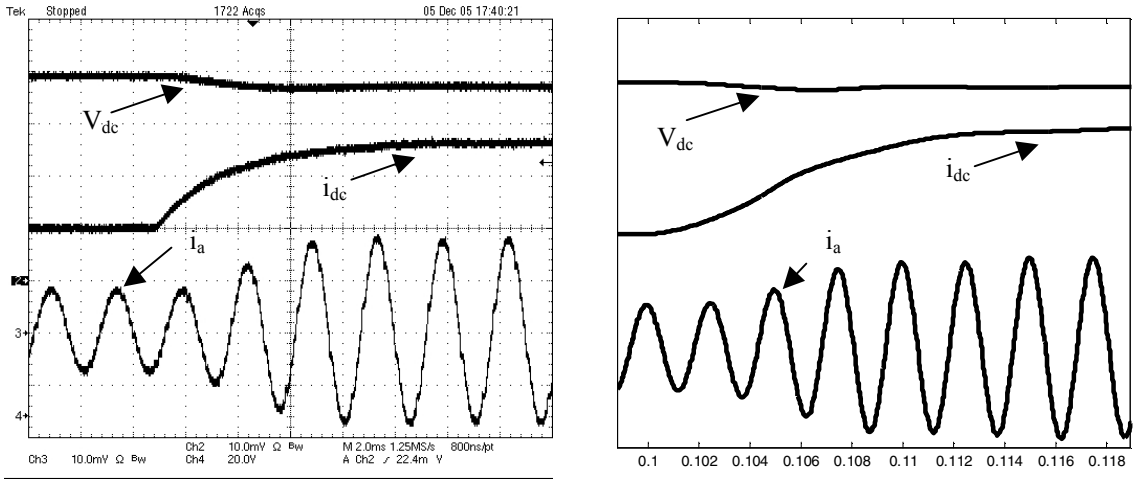


Figure 4-15. Winding current for one leg

To verify the transient responses, the load resistance changes from 10Ω to 4Ω. The line frequency is 400Hz. Figure 4-16 shows the results the close resemblance between the waveforms of the hardware and the improved model.



(a) hardware **(b) improved model**

Figure 4-16. Hardware vs. Improved model @ transient

4.6. Summary

Three average models of the nine-phase diode rectifier based on different load current assumptions, the static model, the dynamic model and the improved model, are compared under steady state and transient operating conditions in this chapter. The detailed switching model is developed in Saber to serve as the benchmark for comparison. Interpolation is applied to generate quantified comparison results. Under all conditions, the improved model is better than the other two. Modeling the load current variation is more important for the nine-phase diode rectifier than for the three-phase diode rectifiers. From the comparison results, the effect of parasitic parameters is discussed. Modeling the feeder's inductance into the average model can improve steady state and transient behavior.

The average model is verified by using a prototype of the nine-phase diode rectifier under steady state and transient operating conditions. When using actual hardware, the primary leakage inductance of the autotransformer makes the commutation period

different for each switching period, which is in conflict with the assumption made in the average model derivation, but this error is small enough to be neglected.

CHAPTER 5 FREQUENCY DOMAIN ANALYSIS OF AVERAGE MODEL FOR DIODE RECTIFIER

5.1. Introduction

In Chapter 4, the evaluation of the average model has been discussed in detail. This provides guidance for applying the average model application in time domain simulations. Meanwhile, another primary application of the average model of the diode rectifier is to obtain the small-signal model, especially the output impedance, for system-level study in the frequency domain. In this chapter, the average model is linearized to get the output impedance for the nine-phase diode rectifier as an example, followed by the discussion of the model's validation in the frequency domain. The feeder's and the generator's impedance are considered when deriving the output impedance.

The small-signal model validation in the frequency domain has been investigated for PWM converters in the past [56-60]. Past research has shown that the small-signal model is only valid below half of the switching frequency, which is explained using sampling theory [56]. The sampling effect is not as obvious for line-commutated diode rectifiers as for PWM converters because diode rectifiers have no controlled duty cycles. However, within one "switching period", the equivalent topology of the rectifier is different during the commutation and conduction modes. The commutation angle can be seen as an equivalent duty cycle in the rectifier, yet it is a non-linear function depended on circuit

parameters and operating points. The impetus to investigate the frequency domain validation of the average model arises from this.

In this chapter, Fourier analysis is applied to study the sampling effect on the voltage and current of the diode rectifier. In this way, the approximation of the average model in the frequency domain can be revealed.

An experiment is performed to complement and verify the validation. The output impedance of the nine-phase diode rectifier is measured using the hardware, the switching model and the average model.

5.2 Output impedance for nine-phase diode rectifier

5.2.1 Output impedances from different average models

The average model for the nine-phase diode rectifier developed in Chapter 3 is a time-invariant, non-linear model. The nonlinear effect comes from the commutation angle, which depends on the circuit parameter, average load current during commutation and the input voltage. The averaged model is rewritten as

$$\begin{aligned}\mu &= a\cos\left(1-\frac{\omega\cdot L_c\cdot i_{dc}}{V\cdot\sin\left(\frac{\pi}{9}\right)}\right)\\ V_{dc} &= \frac{18}{\pi}\cdot V\cdot\sin\left(\frac{\pi}{9}\right)\cdot\left(1+(R_c+R_{on})\cdot\frac{-\mu+\sin\mu}{2\cdot\omega L_c}\right)-\left[\frac{9}{\pi}\cdot\omega L_c+(R+R_{on})\cdot\left(2-\frac{9\mu}{\pi}\right)\right]\cdot i_{dc0}\\ &\quad-\frac{di_{dc}}{dt}\cdot\left[L_c\cdot\left(2-\frac{9\mu}{2\pi}\right)+\frac{(R_c+R_{on})}{\omega}\cdot\left(\frac{\pi}{9}-\mu+\frac{9}{\pi}\cdot\frac{\mu^2}{4}\right)\right]-2\cdot V_{on}.\end{aligned} \tag{5-1}$$

The small-signal model can be constructed based on the equation above. In order to derive the output impedance, a superimposed small ac variation is added to the quiescent operating point of the load current as

$$i_{dc} = i_{dc0} + \hat{i} \,. \tag{5-2}$$

Because the commutation angle is determined by the load current, it also has a superimposed small ac variation. According to the nonlinear expression of the commutation angle, its Taylor series expansion is used to perform linearization:

$$\mu = a\cos\left(1 - \frac{\omega \cdot L_c \cdot i_{dc}}{V \cdot \sin\left(\pi/9\right)}\right) \approx \frac{\pi}{2} - 1 + \frac{\omega \cdot L_c \cdot i_{dc}}{V \cdot \sin\left(\pi/9\right)}. \tag{5-3}$$

Inserting equation (5-2) into (5-3), the variation of the commutation angle is

$$\hat{\mu} = \frac{\omega \cdot L_c \cdot \hat{i}_{dc}}{V \cdot \sin\left(\pi/9\right)}. \tag{5-4}$$

Substituting equation (5-2) and (5-4) into (5-1), the variation of the dc output voltage is

$$\begin{aligned} \hat{V}_{dc} = &-\left[\frac{9}{\pi} \cdot \omega L_c + \left(R_c + R_{on}\right) \cdot \left(2 - \frac{9\mu}{\pi}\right)\right] \cdot \hat{i} - \frac{d\,\hat{i}}{dt} \cdot \left[L_c \cdot \left(2 - \frac{9 \cdot \mu}{2\pi}\right)\right. \\ &\left. + \frac{\left(R_c + R_{on}\right)}{\omega} \cdot \left(\frac{\pi}{9} - \mu + \frac{9}{\pi} \cdot \frac{\mu^2}{4}\right)\right] + \left(R_c + R_{on}\right) \cdot \frac{9 \cdot \omega \cdot L_c}{\pi \cdot V \cdot \sin\left(\pi/9\right)} \cdot \hat{i} \end{aligned} \tag{5-5}$$

From equation (5-5), it can be seen that the output impedance of the nine-phase diode rectifier is composed of an equivalent resistor and inductor in series, which is

$$\begin{aligned} R_{out} &= \frac{9}{\pi} \cdot \omega L_c + \left(R_c + R_{on}\right) \cdot \left[2 - \frac{9}{\pi} \cdot \left(\mu + \frac{\omega \cdot L_c \cdot i_{dc0}}{V \cdot \sin\left(\pi/9\right)}\right)\right]. \\ L_{out} &= L_c \cdot \left(2 - \frac{9 \cdot \mu}{2\pi}\right) + \frac{\left(R_c + R_{on}\right)}{\omega} \cdot \left(\frac{\pi}{9} - \mu + \frac{9}{\pi} \cdot \frac{\mu^2}{4}\right) \end{aligned} \tag{5-6}$$

The average model is simulated in Simulink/MATLAB to get the operating point at the full-load condition as shown in Table 3-1. At this operating point, the commutation angle is 0.221*rad/sec* and the load current is 271.4A. The calculated output impedance is

$$R_{out} = 0.0384\Omega, \qquad L_{out} = 6.756\mu H \ . \tag{5-7}$$

The output impedance of the nine-phase diode rectifier can also be obtained by auto-linearization of the software, which is given in Figure 5-1.

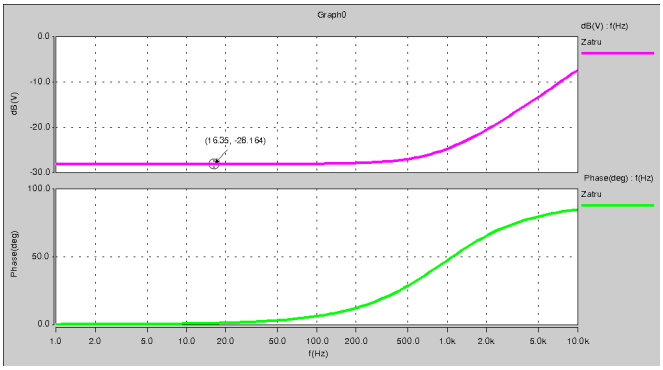


Figure 5-1 Output impedance from the average model

The equivalent impedance can be calculated from Figure 5-1 as

$$R_{out} = 0.039\Omega, \qquad L_{out} = 6.746\mu H \ . \tag{5-8}$$

The results of equations (5-7) and (5-8) show that the derivation result is very close to the result obtained from the auto-linearization procedure. This output impedance is useful for system-level study, such as stability of the system.

Usually the output filter of the nine-phase diode rectifier is connected on the dc terminal. The output impedance including both the rectifier and the output filter is shown in Figure 5-2. The impedance of the output filter itself is also plotted in this figure simultaneously in order to show its effect. Figure 5-2 shows that the output filter is the

main factor in determining the resonance frequency of the impedance. The reason is that the inductance of the output filter is much larger than the equivalent inductance of the diode rectifier. However, the equivalent resistance of the diode rectifier is important to the system behavior. According to (5-7), the equivalent resistance is usually larger than the parasitic resistor of the output filter, and the equivalent resistance will determine the damping factor of the system.

The output impedance of the nine-phase diode rectifier shown in (5-7) is based on the improved model. In Chapter 4, another two average models of the diode rectifier by different assumptions of the load current are introduced. The output impedances derived from these average models are different from the impedance in (5-7).

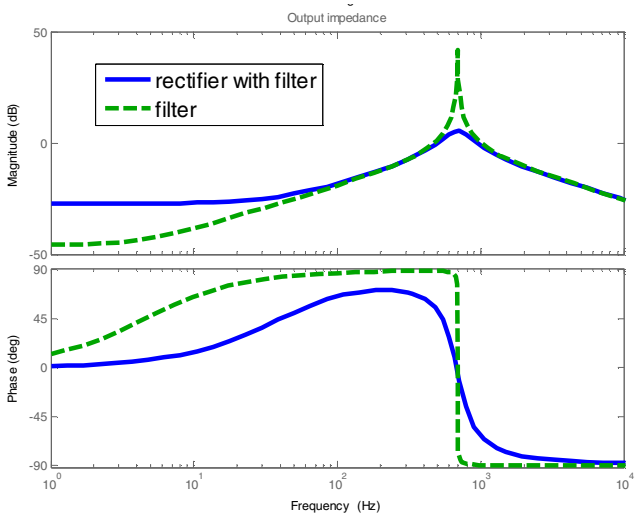


Figure 5-2 Output impedance including output filter

For the static model, the output impedance only has an equivalent resistor for the diode rectifier, which is

$$R_{eq} = \frac{9}{\pi} \cdot \omega \cdot L_c \,. \tag{5-9}$$

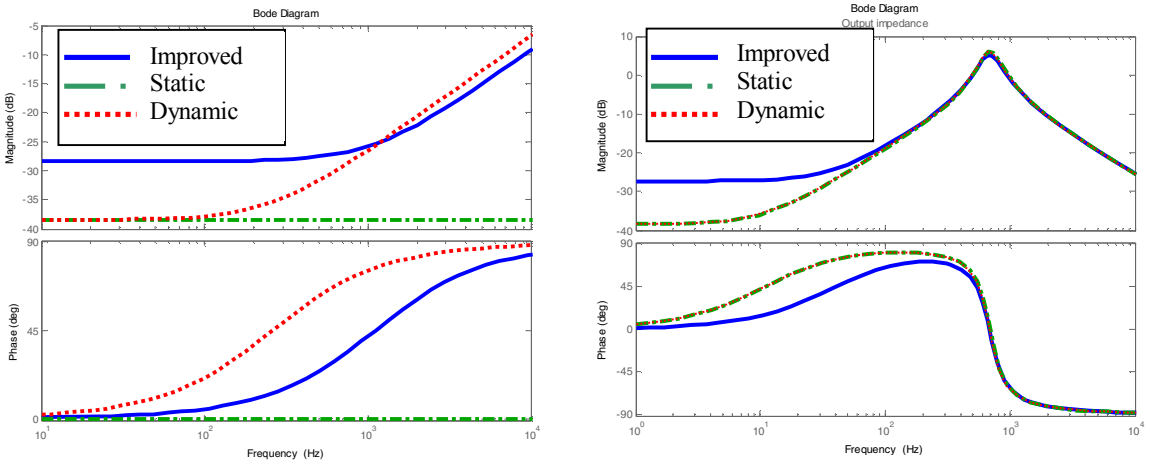
Since the static model does not model any dynamic in the rectifier, the equivalent inductance will be zero.

The output impedance of the dynamic model is composed of an equivalent resistor and inductor as

$$\begin{aligned} R_{eq} &= \frac{9}{\pi}\cdot\omega\cdot L_c \\ L_{eq} &= 2\cdot L_c \end{aligned}. \tag{5-10}$$

The output impedances from the static model and dynamic model are linear. They do not change with the operating point, while the impedance from the improved model does change.

Figure 5-3 (a) gives the output impedances of the diode rectifier only from different average models and Figure 5-3 (b) shows the impedances with the output filter. Since the inductor of the output filter L_{dc} (176 μH) is much larger than the equivalent inductance of the diode rectifier L_{eq} (5μH), the resonance frequency is almost the same for the three models. At the low frequency for the model (below 100Hz here), the equivalent resistor R_{eq} is dominated, so the difference of the impedances becomes significant.



(a) diode rectifier **(b) diode rectifier with output filter**

Figure 5-3 Output impedance of nine-phase diode rectifier

5.2.2 Output impedances with feeder's impedance

It has been pointed out that the feeder's impedance L_p in front of the autotransformer influences the commutation time. In Chapter 3, to obtain the equivalent commutation inductance L_c, L_p is referred to the secondary side of the autotransformer by the current transfer function derived with the non-sinusoidal secondary current, namely nonlinear relationship. Nonetheless, this transfer function is not valid any more when modeling the output impedance from the dc side.

The linearization procedure to obtain the output impedance is inserting a small sinusoidal waveform into the circuit. Therefore, L_p should be referred to the secondary side of the autotransformer multiplied by $n_v \cdot n_i$, namely linear relationship. The output impedance considering the feeder's impedance becomes

$$\begin{aligned} R_{out} &= \frac{9}{\pi}\cdot\omega L_c + (R+R_{on})\cdot\left[2-\frac{9}{\pi}\cdot\left(\mu+\frac{\omega\cdot L_c\cdot i_{dc0}}{V\cdot\sin(\pi/9)}\right)\right] + R_p\cdot n_v\cdot n_i \\ L_{out} &= L_c\cdot\left(2-\frac{9\cdot\mu}{2\pi}\right)+\frac{(R+R_{on})}{\omega}\cdot\left(\frac{\pi}{9}-\mu+\frac{9}{\pi}\cdot\frac{\mu^2}{4}\right)+L_p\cdot n_v\cdot n_i \end{aligned} \quad (5\text{-}11)$$

A user-defined software is developed in Saber to model the output impedance directly using the switching model [65]. This software provides us the possibility to compare the output impedance from the average model and from the switching model. The system in Figure 5-4 is used to verify the output impedance derivation. In order to emphasize on the feeder's impedance, the feeder's impedance is increased to 35μH and the inductance of the output filter is reduced to 50μH. This system is also used for system-level study in the next chapter.

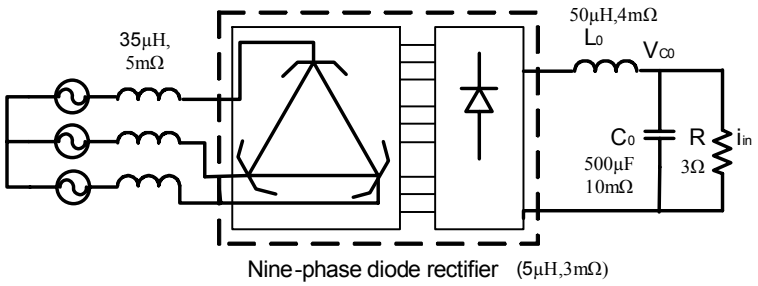


Figure 5-4 System schematic to measure the output impedance

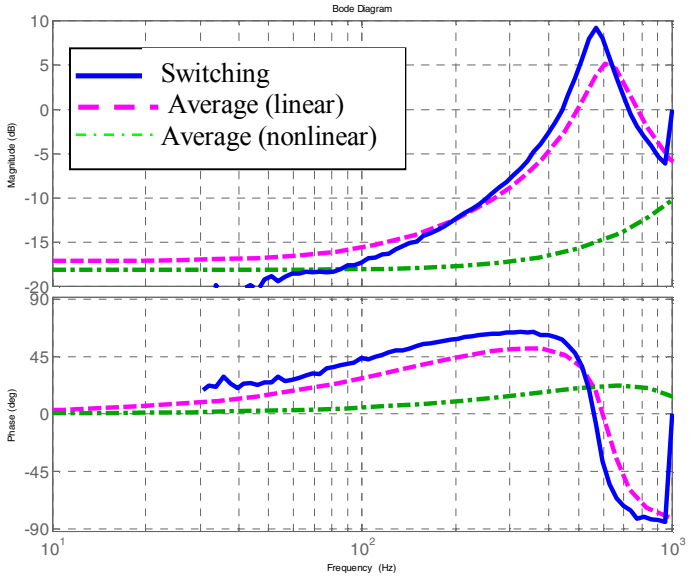


Figure 5-5 Comparison of output impedance of diode rectifier with filter

The output impedances from the switching model and the average model are given in Figure 5-5. There are three curves in this figure: one is from the switching model; the other two are from the average model by modeling the feeder's inductance with linear and nonlinear relationships. We can see that the linear relationship should be used when modeling the feeder's impedance. Nonetheless, there is some discrepancy between the results from the average model and from the switching model. The discrepancy comes from both of these two models. For the output impedance from the switching model, the

user-defined software in Saber has intrinsic errors. In [65], it is pointed out that this software has 10% error with unknown reason. For the output impedance from the average model, the averaging process of the rectifier model has some approximation, which has described in Chapter 4. This also brings the error into the output impedance of the average model.

5.2.3 Output impedances with generator's impedance

Similar to the feeder, the generator's output impedance also influence the commutation time and then the system behavior. In [42], the open-loop subtransient impedances of the generator, L_d'' and L_q'', are used to derive the average model of a generator and a three-phase diode rectifier. The generator flux is used instead of the voltage to derive the differential equations, which combines the generator and the diode rectifier together. The conclusion is that the static commutation inductance L_{ss} is L_d'' for the diode rectifier and it causes the voltage drop on the output dc voltage. When calculating the equivalent commutation inductance of the rectifier, L_{ss} should be added to L_p and the new commutation inductance L_c' is

$$L_c' = L_c + L_{ss} \cdot n_v \cdot n_i' . \tag{5-12}$$

where L_c and n_i' have the same definition as in Chapter 3.

In [43], the dynamics are considered and the transient commutation inductance L_t is derived as $0.5 \cdot L_d'' + 1.5 \cdot L_q''$. L_t only influences the system dynamics, corresponding to the equivalent inductance of the output impedance. The output impedance of the generator and the diode rectifier is

$$R_{out} = \frac{9}{\pi}\cdot\omega L_c' + (R+R_{on})\cdot\left[2-\frac{9}{\pi}\cdot\left(\mu+\frac{\omega\cdot L_c'\cdot i_{dc0}}{V\cdot\sin\left(\pi/9\right)}\right)\right] + R_p\cdot n_v\cdot n_i$$
$$L_{out} = L_c'\cdot\left(2-\frac{9\cdot\mu}{2\pi}\right) + \frac{(R+R_{on})}{\omega}\cdot\left(\frac{\pi}{9}-\mu+\frac{9}{\pi}\cdot\frac{\mu^2}{4}\right) + (L_p+L_t)\cdot n_v\cdot n_i \quad (5\text{-}13)$$

When the generator exists, it is difficult to apply the user-defined software to obtain the output impedance directly from the switching model due to the software limitation. Instead, this output impedance is verified in the next chapter when the average model is applied to the system resonance study.

5.3 Frequency domain analysis of the average and linearized models

The output impedance of the diode rectifier is used mostly for system-level study, such as stability and resonance. The classical control theory for a linear time-invariant system (LTI) can be easily applied to such problems. It is well-known that the linearized model of PWM converters is limited in the frequency domain because of the sampling theorem, yet little effort has been made on this issue for the line-commutated diode rectifier. In this section, the frequency domain validation of the average and linearized model of the diode rectifier is discussed.

5.3.1 Averaging theory for PWM converters

The basic averaging method for switching converters is to average the state space equations in one switching period. Two main averaging methods, state-space averaging and circuit averaging, are developed [40]. The small signal model is obtained by

perturbing the average model at the equilibrium point, which could utilize the classical control theory, such as Bode plot and Nyquist stability criteria [39].

During the averaging process and linearization, approximation is used in the switching model. Much research has been done so far focusing on the validation of the average and small-signal model of PWM converters in the frequency domain and they are summarized as below.

The relationship between the averaging method for switching converters and the mathematical theory of the averaging procedure is revealed in [60]. The standard form of time-varying equations can be expressed mathematically as

$$\dot{x} = \varepsilon \cdot F(t,x), \qquad \varepsilon << 1, \quad x(t_0) = x_0 . \tag{5-14}$$

with *F(t,x)* continuous as a function of *t* and *x*. The time average of the right-hand-side (RHS) of equation (5-11) is defined as

$$G(\bullet) \equiv \lim_{T\to\infty} \frac{1}{T} \cdot \int_0^T F(s,\bullet) ds . \tag{5-15}$$

When the function is periodic or almost periodic, a limitation will exist. In much literature in power electronics, it is usually written as

$$x(t) = \frac{1}{T} \cdot \int_{t-T}^{t} x(\tau) \cdot d\tau . \tag{5-16}$$

The choice of the small parameter ε in (5-11) determines an upper bound on the closeness of trajectories of the average model and the actual system. For example, ε can be the product of the switching frequency and the largest eigenvalue of the system. A smaller ε generates an average model that is closer to the switching model.

A similar conclusion is given in the appendix of [32]. When averaging PWM converters, two different state equations are derived first when the switch is on or off and then is averaged within one switching period as

$$\begin{aligned} \dot{x} &= d \cdot \left(A_1 \cdot x + b_1 \cdot V_g\right) + d' \cdot \left(A_2 \cdot x + b_2 \cdot V_g\right) \\ y &= \left(d \cdot C_1{}^T + d' \cdot C_2{}^T\right) \cdot x \end{aligned} \tag{5-17}$$

where x stands for state variables, A_1 and A_2 for matrices of state space equations, d for the duty cycle, V_g for the input voltage and y for the output variables. Reference [32] points out that the approximation of the averaging in one switching period T is due to

$$e^{d'A_2T} \cdot e^{dA_1T} \approx e^{\left(dA_1 + d'A_2\right) \cdot T} \tag{5-18}$$

Therefore, the state-space averaging model is valid as long as the small ripple condition is satisfied and the switching frequency is much higher than the natural frequency of the circuit, which corresponds to a small ε in the mathematic explanation.

A close-loop buck circuit is presented here as an example, as shown in Figure 5-6.

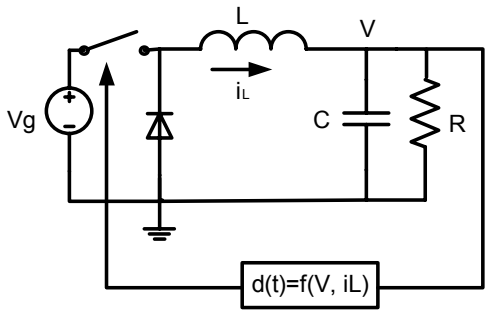


Figure 5-6 Buck circuit

The state equation of the inductor's current in the average model is

$$L \cdot \frac{d\overline{i_L}}{dt} = d(t) \cdot \overline{V_g(t)} + d'(t) \cdot \overline{V(t)}, \tag{5-19}$$

where i_L, V_g, and V are the averaged values within one switching period.

At this point, the sampling effect does not play a role in the averaging process and the average model is meaningful regardless of the switching frequency for the dc-dc converter. The nonlinear nature of the original model is preserved when multiplying two time-varying vectors.

Since the sampling effect does not exist in the average model, the frequency limitation for the small-signal model is generated from linearization. Some new models have been developed to improve the model's precision in frequency domain. A hybrid model for current-controlled PWM dc-dc converters, which mixes the average model of the power stage and the discrete model in the control loop, is presented in [57]. Instead of averaging the circuit first, the linearized model is developed using the *Z*-transform to represent the controller. Another new model is to model the sampling effect as a transfer function from the derivation of the *Z*-transform in [58]. The accuracy of the small-signal model is improved by adding the sampling effect, and the open-loop subharmonic oscillation in the peak current control method can be predicted.

But this small-signal model is still limited in the frequency domain. When comparing the model with the hardware experiments using network analyzers, they usually agree with each other because they both only consider fundamental frequencies. With reference to the effects of the replicas in sampling and hold, the agreement between the measurement and the model is not sufficient to predict the close-loop stability using the LTI theory when the control perturbation is a high frequency. In [59], the simulation results show that the small-signal model of a PWM converter is valid only well below the

switching frequency. As an example, for the boost circuit, the small-signal model should be used up to one tenth of the switching frequency.

5.3.2 Averaging theory for line-commutated diode rectifier

Although the averaging theory has been studied intensively for the dc-dc PWM converters, little study has been done on the sampling theorem for the ac-dc diode rectifiers. For a PWM converter, the sampling effect exists in the small-signal model because of the modulator, while no such block exists in diode rectifiers. Since the topology of the diode rectifier changes between the commutation and conduction period, the commutation angle behaves similar to the duty cycle for the average model. The commutation angle is not an independent variable, and it depends on the circuit parameters and operating point. Therefore, the rectifier can be treated as a close-loop circuit with nonlinear control for the commutation time.

In [48], an average model for the three-phase diode rectifier is developed using the transfer function method. It says that the model is only valid below half of the switching frequency, but gives no further analysis. Nonlinear theories, such as the Poincare map and bifurcation, have been applied to the diode rectifier in [62], but this study focuses on the stability issue of the rectifier itself with no discussion of system-level stability, which is beyond the scope of this work.

The sampling effect is studied for the average model of the line-commutated diode rectifier to give the frequency domain validation. Equation (5-1) is the average model of the nine-phase diode rectifier, and the only nonlinear effect is the calculation for the commutation angle. This equation is derived by averaging the voltage at the output side

of the switching network and it is time-invariant, nonlinear. This is different than the average model of the buck circuit in (5-19), which is a time-variant, nonlinear model. Hence, the average model of the diode rectifier is between the average and switching model of the buck converter.

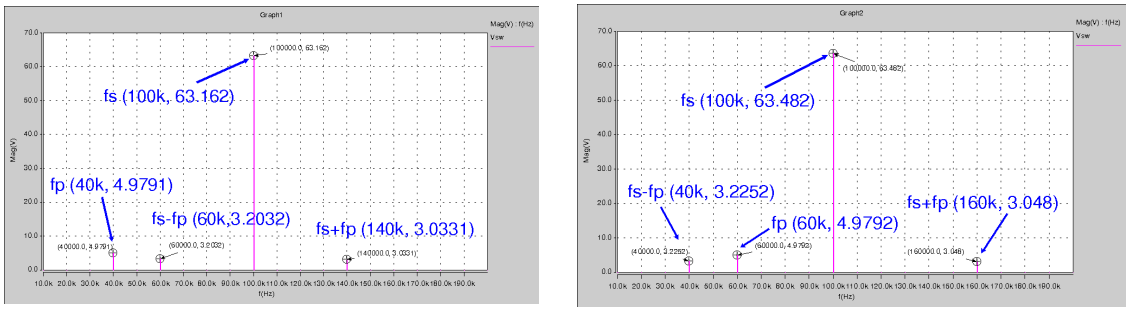
Buck circuit is analyzed to illustrate this problem. Its average model is defined as (5-19), and the harmonics of the system is remained by the production of the duty cycle *d(t)* and the averaged input voltage <*Vg(t)*>, and the sampling effect does not take place in the average model. However, when applying the same averaging method to the buck circuit as the method applied for the diode rectifier, the averaged voltage of the switching node, V_{sw}, is

$$\overline{V_{sw}} = \overline{d(t) \cdot V_g(t)} . \tag{5-20}$$

When the duty cycle is assumed to be constant, the new average model of the buck circuit becomes

$$\overline{V_{sw}}' = D \cdot \overline{V_g(t)} = \overline{d(t)} \cdot \overline{V_g(t)} . \tag{5-21}$$

Fourier analysis is used to analyze the sampling effect in the models. Figure 5-7 shows the Fourier analysis of V_{sw} for the switching model for the case in which a small ac signal with the frequency f_p is added into the input voltage source $V_g(t)$ and the switching frequency of the switch f_s is 100kHz. According to the sampling theorem, the harmonics generated by the switching network is f_s-f_p. When f_p exceeds half of the switching frequency, lower harmonics than f_p exists in V_{sw}, which the output filter cannot filter out. The average model in (5-21) only contains the component of f_p, and the component of f_s-f_p does lose in this average model due to sampling theorem.

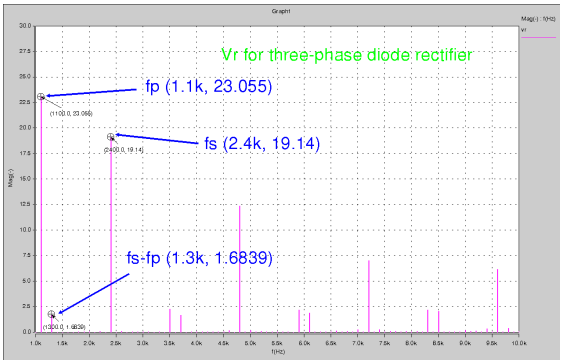


(a) $f_p = f_s/2$-10kHz **(b)** $f_p = f_s/2$+10kHz

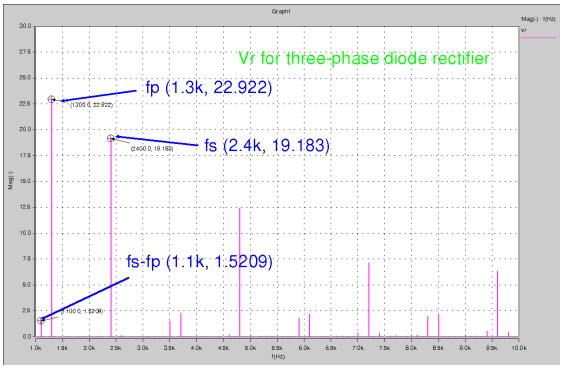
Figure 5-7 Fourier analysis of V_{sw}

The average models of the three-phase and nine-phase diode rectifiers have the same derivation procedure as the procedure in (5-21). If the harmonic introduced by the nonlinear equation of the commutation angle is trivial, only the component at the perturbation frequency is remained in the average models. As illustrated above, the sampling information of the topology changing even in the average model is lost.

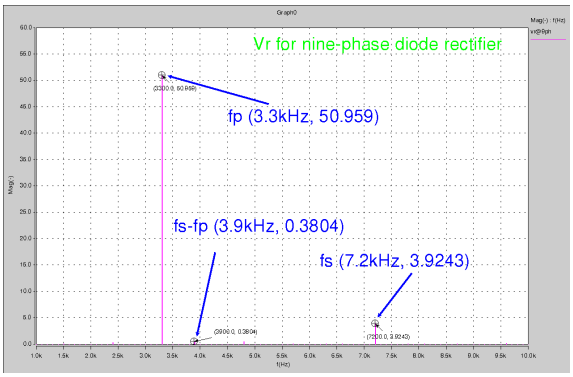
Fourier analysis is applied to the output dc voltage right after the switching network V_{dc} for switching models. Since the average model of the diode rectifier is in the *dq*-axes, the perturbation of the input voltage is added into its *d*-axes V_d while V_q stays zero. The inversed Park transformation is then used to generate the voltage in the *abc*-axes for switching models with a line frequency of 400Hz. The switching frequency is 2400Hz for the three-phase diode rectifier and 7200Hz for the nine-phase diode rectifier. The amplitude of the perturbation is set to be 10% of the peak voltage. The perturbation frequencies are set 1100Hz and 1300Hz for the three-phase diode rectifier, while they are 3300Hz and 3900Hz for the nine-phase diode rectifier. Figure 5-8 gives the simulation results.



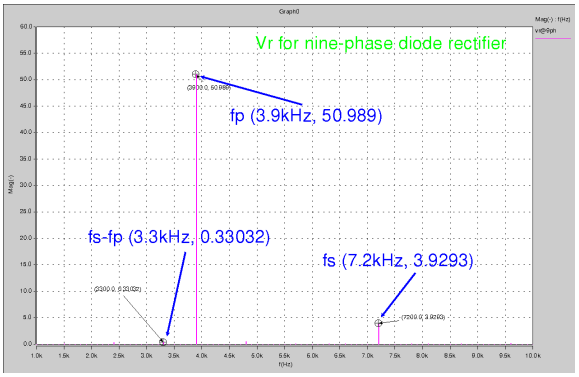
(a) f_p @1100Hz for three-phase



(b) f_p @ 1300Hz for three-phase



(c) f_p @ 3300Hz for three-phase

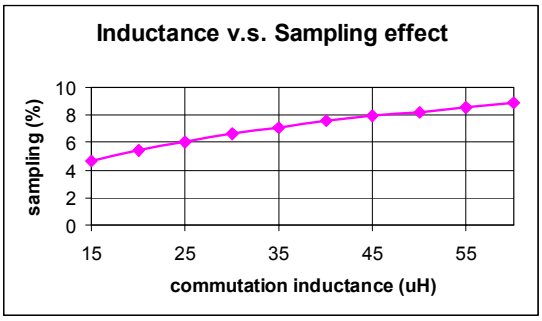


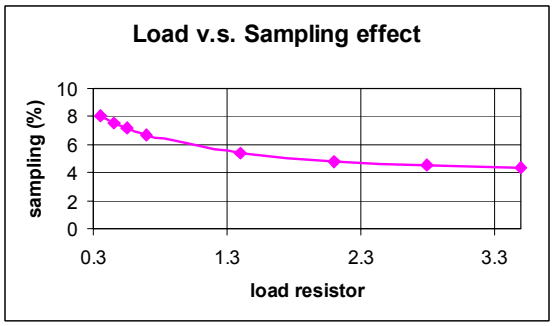
(d) f_p @ 3900Hz for nine-phase

Figure 5-8 Fourier analysis for three-phase and nine-phase diode rectifier

In Figure 5-8, the component at f_s-f_p exists in the output voltage of the diode rectifier, which proves that the sampling theorem is effective in the switching model of the line-commutated diode rectifier. The product of the commutated inductance and load current plays an important role in the sampling issue: it acts as the duty cycle in a buck converter. In a buck converter, if the duty cycle is 1, there will be no sampling effect in the circuit because the switch is always om. In a line-commutated diode rectifier, if there is no commutation inductor, the circuit topology stays the same and thus there is no sampling action at all. Here we define the ratio $R_{s\text{-}p}$ of the component at f_s-f_p to the component at f_p. When the line inductance or the load current increases, $R_{s\text{-}p}$ becomes larger. Figure 5-9 gives the quantified result for the nine-phase diode rectifier. Figure 5-9 (a) shows the

results when changing the commutation inductance and the simulation results with different load resistors are given in (b). The ratio between the voltage magnitude at f_s-f_p and f_p is calculated. The perturbation frequency is chosen to be 3900Hz. This means that when the ommutation period becomes longer, the sampling effect becomes more significant for the circuit, and cannot be ignored any longer.





(a) inductance effect **(b) load current effect**

Figure 5-9 Influence of commutation inductance and load current on sampling issue

From the above statement, it can be concluded that the average model of the diode rectifier is only valid for half of the switching frequency.

The small-signal model of the diode rectifier is used only to perform linearization of the commutation angle's function, while other equations are already linear differential equations. Due to the limitation of the average model in the frequency domain, the small-signal model cannot be used beyond half of the switching frequency.

The output impedance of the diode rectifier is therefore theoretically valid within half of the switching frequency. However, when the line commutation inductance is much smaller than the inductor of the output filter, the output impedance can be used into the high-frequency range because the filter's output impedance will dominate the output impedance, which is the usual case in an aircraft system.

5.4 Experiment for output impedance

The output impedance of the diode rectifier can be measured using the hardware. The system under test has the same parameters for time domain verification as given in Table 4-1 and the load is 10Ω. Figure 5-10 shows the measurement of the output impedance.

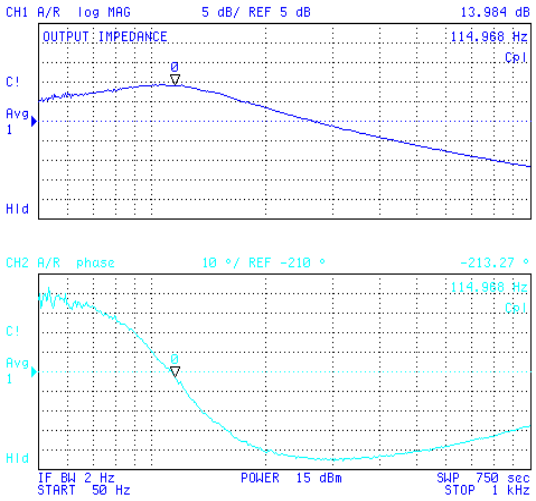


Figure 5-10 Measurement of output impedance (nine-phase diode rectifier with output filter)

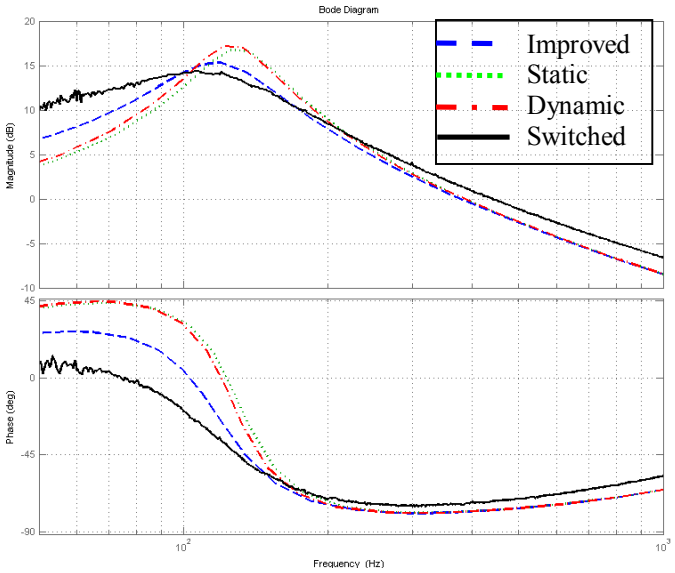


Figure 5-11 Output impedance comparison (nine-phase diode rectifier with output filter)

The impedance from the hardware measurement is compared with the impedance derived from different average models in Figure 5-11. It is shown clearly that the output impedance from the improved model best matches the impedance from the experiments.

5.5 Summary

The frequency domain validation of the average and small-signal models of the diode rectifier is discussed in this chapter. The output impedance of the nine-phase diode rectifier is derived first, with the validation of the hardware experiment. After reviewing the literature of the average theory for PWM converters, it is concluded that the sampling effect does not affect the average model of PWM converters. However there is some difference between the average model of the diode rectifier and the average model of the PWM converter. Fourier analysis shows that the average model of the diode rectifier loses the sampling information, which limits the model to below half of its switching frequency. The small-signal model of the rectifier is based on the average model, which also has this limitation. Nevertheless, when the output filter inductor is much larger than the equivalent commutation inductor, the output impedance is mainly dependent on the output filter and it can be applied to the high-frequency range.

CHAPTER 6 SYSTEM HARMONIC RESONANCE STUDY

6.1 Introduction

With the development of power semiconductor, more switching equipment is applied into aircraft power systems for better performance. While switching equipment is lighter and consumes less power, its nonlinear behavior introduces harmonics into systems. Harmonic resonance will occur when the system natural frequency equals the harmonic frequency, which might cause catastrophic problems. Study of harmonic resonance becomes a necessity when a nonlinear load exists in the system [66-68].

The harmonic resonance problem has been studied intensively in industrial power systems, yet not much has been done for the rectifier-inverter power system. In such systems, the resonance usually occurs between the inductor and the dc bus capacitor, which influences the system behavior significantly. A detailed modeling approach to predict the resonance in such systems is proposed in this chapter. This approach could provide the system design guidance in order to avoid the resonance problem.

Two main aspects determine the resonance in a system: when the resonance will happen and how much it will affect the system. Therefore, it is important to render an accurate model to predict the resonance frequency, the harmonic source and the damping ratio. In previous research, the switching blocks are modeled as ideal current or voltage sources representing harmonic sources, depending on the load type [69]. The nonlinear

blocks are eliminated from the system and classical control theory can be applied. The transfer function is derived to determine the resonance frequency and the amplification.

The system under study in this dissertation is a simplified rectifier-inverter aircraft power system. The nine-phase diode rectifier with generator and voltage-source-inverter motor drive (VSI-MD) are the two blocks that generate harmonics. Unlike previous work, we do not model the rectifier and the inverter as ideal sources only. Instead, they are modeled by Norton's and Thevenin's equivalent circuits for resonance study. Modeling the equivalent impedance is important when the impedances of the rectifier and inverter are not trivial compared to the filters in the system.

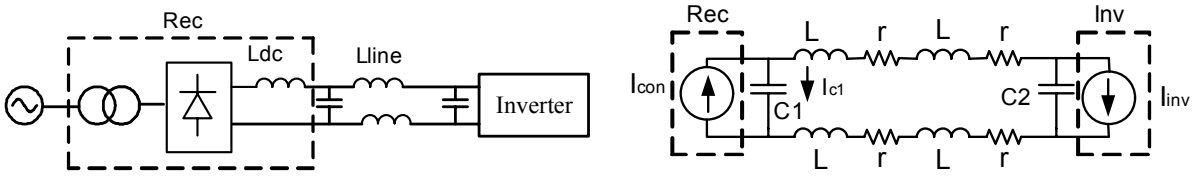
The average model is used to derive the equivalent impedance of the circuit, and the harmonic source can be obtained through open-circuit and short-circuit simulation of the switching models. The system becomes linear with equivalent circuits and transfer function and superposition are adopted to study the resonance phenomenon in this system.

The equivalent circuit is verified through the comparison of transfer functions from the equivalent circuit and the detailed switching model. Some resonance issues, such as the relationship between stability and resonance, as well as the influence on resonance by the controllers of the motor drive and the generator, are also discussed in this chapter.

6.2 System modeling for resonance study

6.2.1 Overview of previous research

The typical dc power system is a rectifier-inverter system with bus capacitors to stabilize dc voltage, which is shown in Figure 6-1 (a). The line inductance L_{line} and the bus capacitors might cause resonance in this system.



(a) System schematic **(b) Equivalent circuit diagram**

Figure 6-1 Typical rectifier-inverter power system

The harmonic resonance in this system has been studied in [78]. The equivalent circuit diagram is shown in Figure 6-1 (b). It is assumed that the output filter inductor of the rectifier, L_{dc}, is so large ($100mH$) that the rectifier can be treated as a current source nonlinear load (CSNL) type [69]. The inverter is also a CSNL because of its inductive characteristic. The inverter and the rectifier are modeled as ideal current source I_{inv} and I_{con}, and their values can be measured from the hardware. The transfer function from I_{inv} to the bus capacitor's current I_{c1} is used to analyze the resonance phenomenon. From the gain of that transfer function, the resonance frequency and the amplification at each frequency are shown clearly. The harmonics from the rectifier side are ignored because the large L_{dc} filters out the harmonics from the rectifier side and I_{con} is modeled as a constant dc current.

6.2.2 System modeling

The system for resonance study in this work is similar to the system in Figure 6-1, representing a simplified aircraft power system. The system block diagram is shown in Figure 6-2, which is composed of a synchronous generator, a nine-phase diode rectifier, its output filter, a voltage source inverter as the motor controller and a permanent magnet synchronous machine (VSI-MD), with another input filter in front of it, as the load.

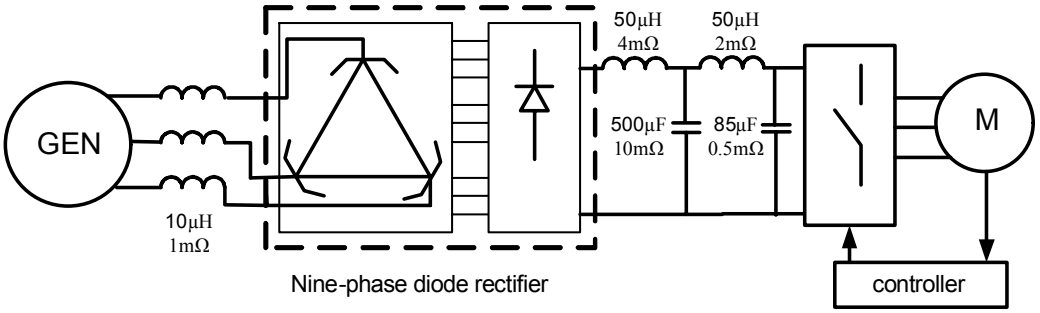


Figure 6-2 Simplified aircraft power system

The generator with the nine-phase diode rectifier and the VSI-MD are two nonlinear blocks in this system. Because of their input/output interface, the VSI-MD is a CSNL and the rectifier is a voltage source nonlinear load (VSNL). Instead of using ideal current and voltage source for equivalent circuit, Norton's and Thevenin's equivalent circuits are derived for these blocks respectively, modeling the blocks' impedances as well. The linearized system is shown in Figure 6-3. The harmonic sources in the system generated from two blocks are modeled as I_{in} and V_d. They usually become large in the system under abnormal operating conditions. The impedances Y_{in} and Z_s vary with the operating point. The system becomes linear with the equivalent circuits, so the linear theory can be used.

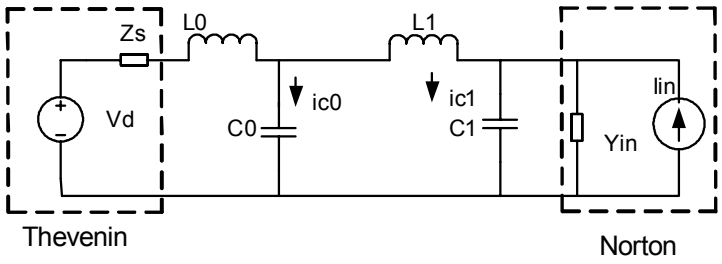


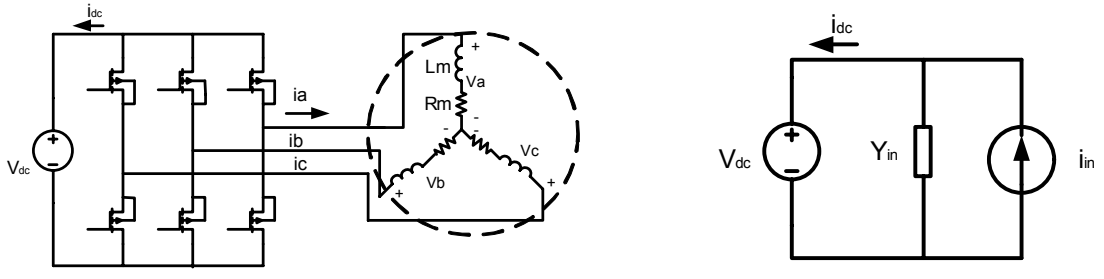
Figure 6-3 Equivalent circuit of the system for resonance study

In the following sections, Norton's and Thevenin's equivalent circuits are derived in detail along with the discussion of parameter influence on the resonance behavior. Superposition is utilized in order to simply the study. The harmonics from the VSI-MD side and the rectifier side are investigated separately.

6.2.3 Norton's equivalent circuit for motor drive

6.2.3.1 PWM and motor drive model

Both the switching and the average models are needed to obtain Norton's equivalent circuit for the VSI-MD. The switching model of the VSI-MD is given in Figure 6-4 (a) and its Norton's equivalent circuit is in Figure 6-4 (b), including an equivalent source and admittance.



(a) Switching model **(b) Norton's equivalent circuit**

Figure 6-4 Inverter and motor drive model

The average model of VSI-MD in Figure 6-5 is derived by averaging the PWM inverter along with the motor drive equations within one switching period in *dq*-axes [37]. The PWM inverter is controlled by the line currents in *dq*-axes and the speed of the motor drive. The current loop control is the inner loop, and the outer loop is the speed loop control, all of which are PI controllers. The controller parameters are designed to eliminate the poles and zeros in the power stage. Therefore, theoretically the motor's dynamics depends only on the controller's bandwidth. The current control loop bandwidth is denoted as ω_i and speed loop as ω_s. The motor is designed to make ω_i always be 10 times ω_s.

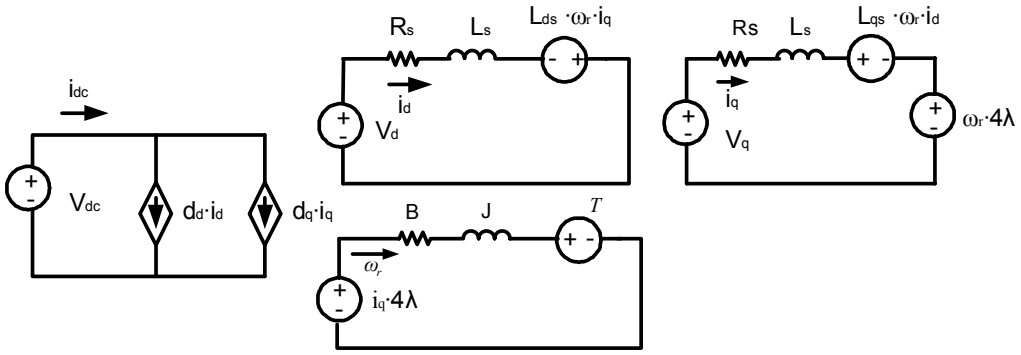


Figure 6-5 Average model of VSI-MD

6.2.3.2 Norton's equivalent circuit derivation

The Norton's equivalent circuit is composed of the current source and its equivalent input admittance of VSI-MD. The input admittance of VSI-MD can be obtained through its average model in Figure 6-5 using auto-linearization of the simulation software. It can also be derived using mathematical derivation. The coupling block in the average model is assumed to be totally compensated by the controller. The input current $i_{dc}(t)$ of PWM inverter is

$$i_{dc} = \left(D_d + \tilde{d}_d \right) \cdot \left(I_d + \tilde{i}_d \right) + \left(D_q + \tilde{d}_q \right) \cdot \left(I_q + \tilde{i}_q \right) \cdot \tag{6-1}$$

The current I_d is usually controlled to be zero, which gives the expression of the input admittance as

$$Y_{in} = \frac{\tilde{i}_{dc}}{\tilde{V}_{dc}} = D_d \cdot \frac{\tilde{i}_d}{\tilde{V}_{dc}} + D_q \cdot \frac{\tilde{i}_q}{\tilde{V}_{dc}} + I_q \cdot \frac{\tilde{d}_q}{\tilde{V}_{dc}}, \tag{6-2}$$

where D_d, D_q and I_q are steady-state values.

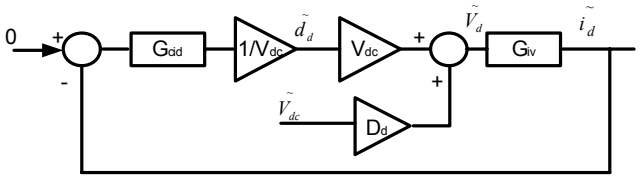
The input voltages to currents in dq-axes are

$$\begin{aligned} \tilde{V}_d &= \left(V_{dc} + \tilde{V}_{dc} \right) \cdot \left(D_d + \tilde{d}_d \right) = V_{dc} \cdot \tilde{d}_d + \tilde{V}_{dc} \cdot D_d = \left(s \cdot L_m + R_m \right) \cdot \tilde{i}_d \\ \tilde{V}_q &= \left(V_{dc} + \tilde{V}_{dc} \right) \cdot \left(D_q + \tilde{d}_q \right) = V_{dc} \cdot \tilde{d}_q + \tilde{V}_{dc} \cdot D_q = \left(s \cdot L_m + R_m \right) \cdot \tilde{i}_q \end{aligned} . \tag{6-3}$$

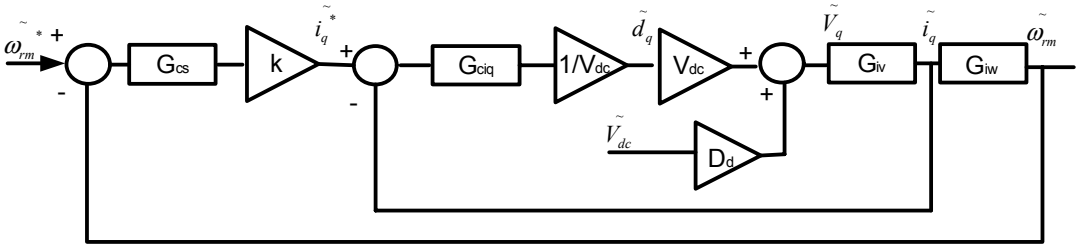
Since the coupling effect is eliminated in the controller, the transfer function of the motor drive G_{iv} can be written as

$$G_{iv} = \frac{\tilde{i}_d}{\tilde{V}_d} = \frac{\tilde{i}_q}{\tilde{V}_q} = \frac{1}{s \cdot L_m + R_m} \cdot \tag{6-4}$$

Other transfer functions are defined in a similar way: G_{iw} is i_q to speed ω_r; G_{cid} and G_{ciq} is the current loop compensator in d/q-axes; G_{cs} is the speed loop compensator. The control block diagram is given in Figure 6-6.



(a) d-axis



(b) q-axis

Figure 6-6 Control block diagram

From the above figure, the following equations are derived as

$$D_d \cdot \frac{\tilde{i}_d}{\tilde{V}_{dc}} = \frac{D_d \cdot G_{iv}}{1 + G_{iv} \cdot G_{id}} = D_d \cdot \frac{1}{sL_m + R_m} \cdot \frac{1}{1 + \frac{1}{sL_m + R_m} \cdot \frac{\omega_i}{s} \cdot (sL_m + R_m)} = D_d \cdot \frac{1}{sL_m + R_m} \cdot \frac{s}{s + \omega_i}$$

$$D_q \cdot \frac{\tilde{i}_q}{\tilde{V}_{dc}} = \frac{D_q \cdot G_{iv}}{1 + G_{iv} \cdot G_{cid} \cdot (1 + k \cdot G_{cs} \cdot G_{iw})} = D_q \cdot \frac{1}{sL_m + R_m} \cdot \frac{s^2}{s^2 + w_i \cdot (s + w_s)} \quad (6\text{-}5)$$

$$I_q \cdot \frac{\tilde{d}_q}{\tilde{V}_{dc}} = -\frac{I_q}{V_{dc}} \cdot G_{ciq} \cdot (1 + k \cdot G_{cs} \cdot G_{iw}) \cdot \frac{\tilde{i}_q}{\tilde{V}_{dc}} = -\frac{I_q}{V_{dc}} \cdot D_q \cdot \frac{w_i \cdot (s + w_s)}{s^2 + w_i \cdot (s + w_s)}$$

The input impedance Z_{in} (reciprocal of Y_{in}) of VSI-MD using (6-5) is plotted in Figure 6-7.

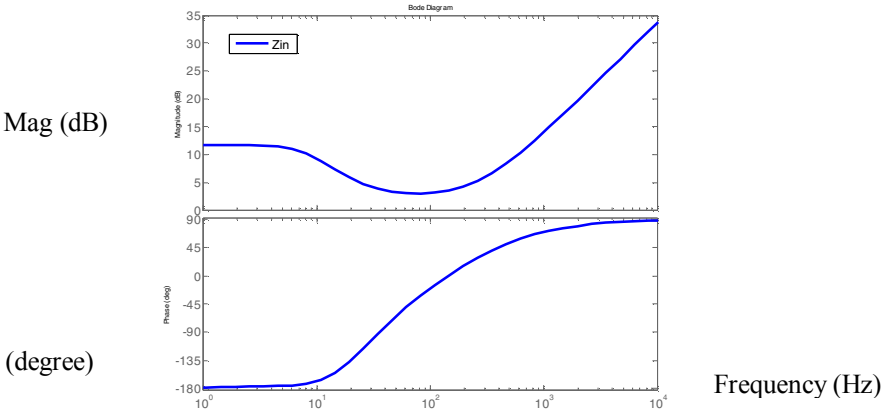


Figure 6-7 Input impedance of VSI-MD

From Figure 6-7, it can be seen that the input impedance at low frequency is determined by the power of the motor drive, $-V_{dc}/I_d \cdot D_q$. Because the VSI-MD is a constant power load, the negative sign means that it is a negative resistance in the small-signal sense. In the high frequency range, the impedance behaves like an inductor. In the middle, Z_{in} depends on both controller and motor parameters, where the resonance might occur. Therefore, the controller has a close relationship with system resonance, which is discussed in detail in section 6.3.2.

It should be noted that the input impedance is valid only within half of the switching frequency because of the average model limitation in the frequency domain.

The current source in Norton's equivalent circuit represents the harmonics generated from the VSI-MD block, which can be obtained through the switching model by short-circuit test. An ideal dc voltage source is connected with the VSI-MD to provide the desired operating condition. The harmonic source could be measured from the input current of VSI-MD. There is no current sharing of the harmonics by Y_{in} because the ideal voltage source has zero ac impedance. In other words, the input current i_{dc} has both dc and ac components. The dc component is the input voltage divided by the equivalent dc resistor of VSI-MD. The ac component is the harmonics existing in this block, which is equal to the harmonic source in Norton's equivalent circuit, i_{in}. The current source i_{in} will not flow through the equivalent admittance Y_{in} because the voltage source would short-circuit in other frequencies except for the dc frequency. Therefore, performing the Fourier analysis for i_{dc} can provide a model of the harmonic source in Norton's equivalent circuit i_{in}.

6.2.3.3 Norton's equivalent circuit verification

A detailed switching model is used to verify the Norton's equivalent circuit derived from the average model. Instead of measuring Y_{in} from the switching model directly, a transfer function including Y_{in} is derived in a linear network in Figure 6-8. The equivalent source in the Norton's circuit is ignored when verifying Y_{in} because the harmonics are little under normal operating conditions.

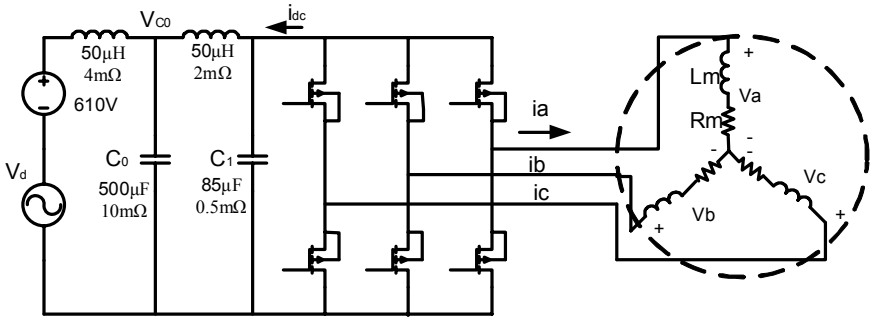


Figure 6-8 Verification of Y_{in}

There are two methods to obtain the transfer function. One method is to derive the transfer function from average model with Y_{in}. If the Norton's equivalent circuit proves correct for resonance study and the harmonic source can be ignored during normal operation, the transfer function V_{c0}/V_d is

$$\frac{V_{c0}}{V_d} = \frac{(Z_{c1} // Z_{in} + Z_{L1}) // Z_{c0}}{(Z_{c1} // Z_{in} + Z_{L1}) // Z_{c0} + Z_{L0}}. \tag{6-6}$$

The other way to get this transfer function is to simulate the switching models with perturbation under different frequencies. As shown in Figure 6-8, this can be achieved by changing the frequency of V_d and doing Fourier analysis of V_{C0} at each corresponding frequency. The verification result is given in Figure 6-9.

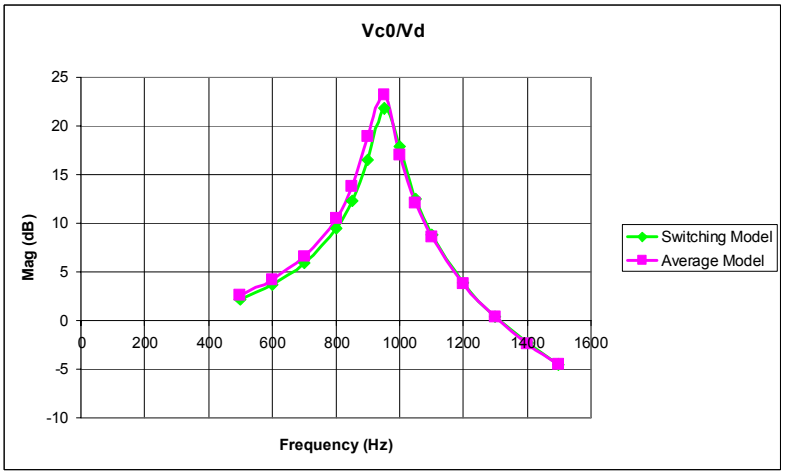


Figure 6-9 Verification result of Y_{in}

The two transfer functions match well in Figure 6-9, which verifies the accuracy of the equivalent admittance of the Norton's equivalent circuit Y_{in} for resonance study.

The transfer function method is also applied to verify the harmonic source. In contrast with Y_{in}, I_{in} is modeled from the switching model directly. Under normal operation, its Fourier component is so small that Saber software cannot get an accurate simulation result. A three-phase balanced current source at frequency f_p is inserted into this block to solve this problem as shown in Figure 6-10. The harmonics in this block are at the frequency of f_p-f_{line}, where f_{line} is the line frequency of the PWM inverter.

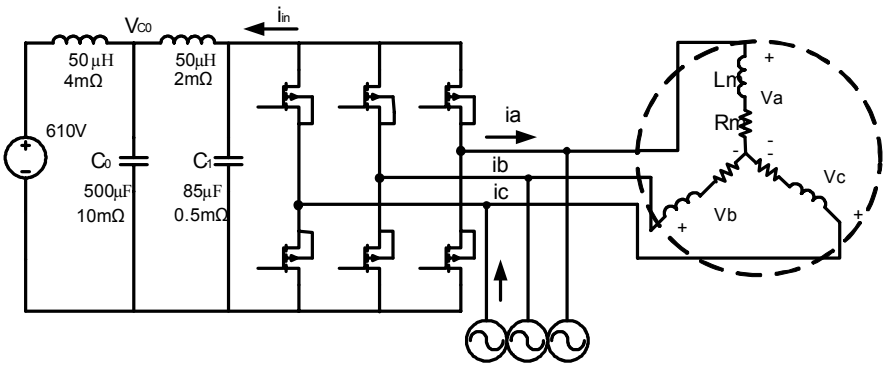


Figure 6-10 Verification of I_{in}

After obtaining the harmonic source I_{in} when the VSI-MD is connected with the ideal voltage source directly, the transfer function of V_{C0}/ I_{in} is plotted by two methods. The first method is to derive the transfer function using the Norton's equivalent circuit as

$$\frac{V_{c0}}{i_{in}} = \frac{Z_{c1} // Z_{in}}{Z_{L1} + Z_{L0} // Z_{c0} + Z_{C1} // Z_{in}} \cdot Z_{L0} // Z_{C0} \cdot \tag{6-7}$$

The second method is to plot the transfer function by changing f_p and doing Fourier analysis of V_{C0} using the switching model. Because Y_{in} has already been proven to be correct, the model of I_{in} can be verified if these two transfer functions are the same. The verification result is given in Figure 6-11.

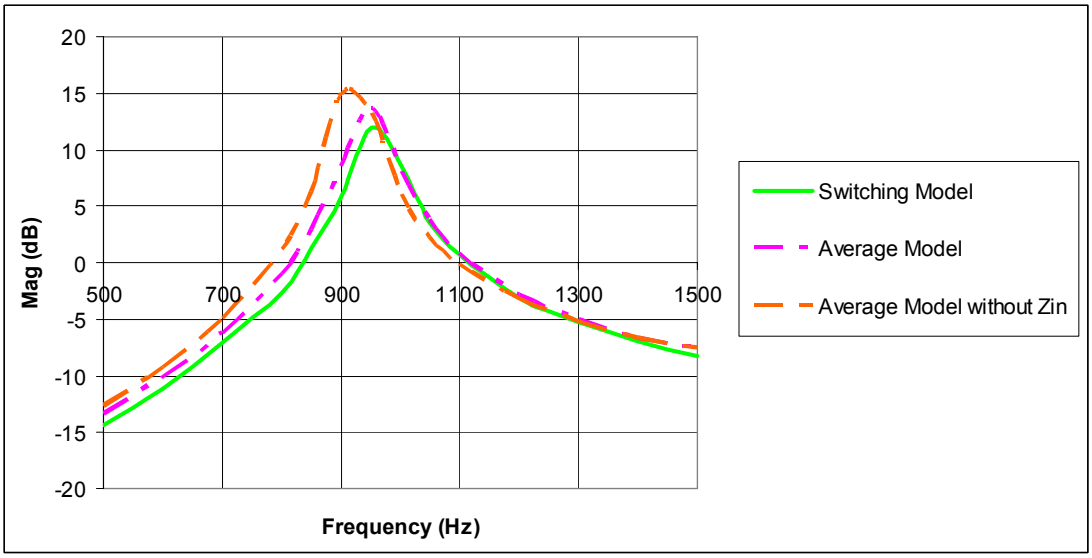


Figure 6-11 Verification result of I_{in}

The transfer functions from the switching model and the Bode plot match well in this figure. It is proven that the source model in the Norton's equivalent circuit can be obtained by doing Fourier analysis of the dc current of the VSI-MD in short-circuit.

Another curve is given in the same figure to show Y_{in}'s effect. In most resonance studies, Y_{in} is ignored. Y_{in} can be neglected only when it is large enough in comparison

with the filter parameters. In Figure 6-11, Y_{in}'s influence on system resonance behavior is clearly shown. The resonance frequency and damping factor change when modeling Y_{in} into the system. Since the equivalent impedance of VSI-MD can be approximately calculated as an inductor in series with a resistor, it can damp the system resonance.

During this verification, the resonance that might be caused by the harmonics from VSI-MD is analyzed at the same time. The resonance frequency and corresponding amplification can be determined from the gain of the transfer function in Figure 6-11.

6.2.4 Thevenin's equivalent circuit for diode rectifier and generator

6.2.4.1 Generator and nine-phase diode rectifier model

A synchronous generator is used in this system, which is a linear model described by a set of differential equations. The exciter is modeled as a voltage source for simplicity. There is a three-loop controller for this generator shown in Figure 6-12. The output voltage of the generator stays constant by an outer loop – a voltage-loop PI controller and an inner loop – a current-loop PI controller, while the line frequency can be varied from 360Hz to 800Hz by the speed loop control. The feeders are modeled as inductance and resistance for each phase.

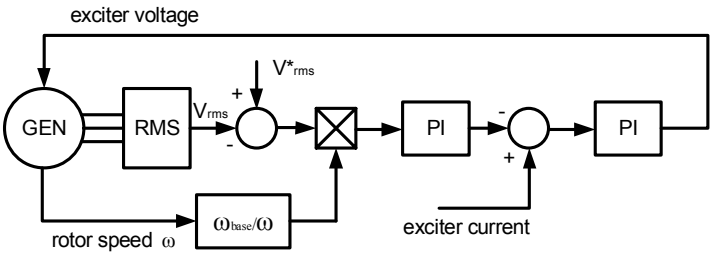
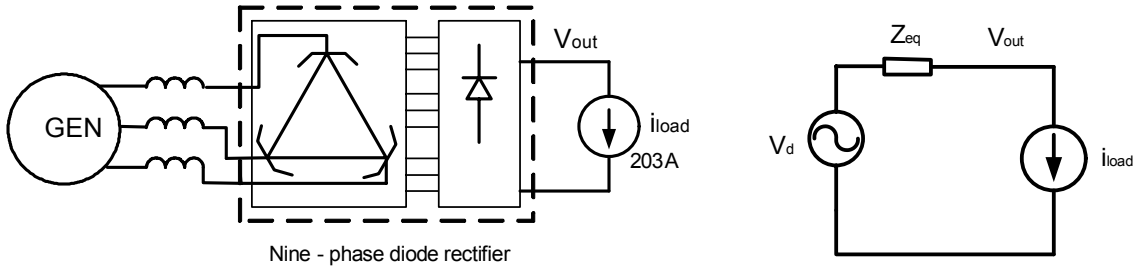


Figure 6-12 Generator controller

6.2.4.2 Thevenin's equivalent circuit derivation

The method to obtain the Thevenin's equivalent circuit for the generator and rectifier is similar to the derivation of the Norton's equivalent circuit for the VSI-MD.

Open-circuit simulation is performed to get the harmonic source V_d from the switching model, using the dc current source as the load in Figure 6-13. The harmonics generated from this block V_d is the voltage on the output side V_{out} in ac signal.



(a) Switching model **(b) Thevenin's equivalent circuit**

Figure 6-13 Generator and rectifier model

The average model is used to get the equivalent output impedance Z_{eq}. In Chapter 5, the equivalent output impedance of the generator and nine-phase diode rectifier Z_{eq} has been derived. It includes the leakage inductance of the autotransformer, the feeders and the generator open-loop subtransient inductances. The result is given in Figure 6-14, including both Z_{eq} and L_{dc}. The generator's dynamics is ignored.

The output impedance Z_{eq} can be calculated from the above figure. The dc gain is the total resistor R_{total}, which is the sum of the parasitic resistor of the output filter's inductor and the resistor of Z_{eq}. The total inductance L_{total} can be calculated from the zero of this output impedance. The equivalent inductor of Z_{eq} is equal to L_{total} minus the output filter inductance L_{dc}. From Figure 6-14, Z_{eq} is

$$R_{eq} = -15.3dB - 0.004 = 0.1718 - 0.004 = 0.1678\Omega$$
$$L_{eq} = 83.797\mu H - 50\mu H = 33.797\mu H \tag{6-8}$$

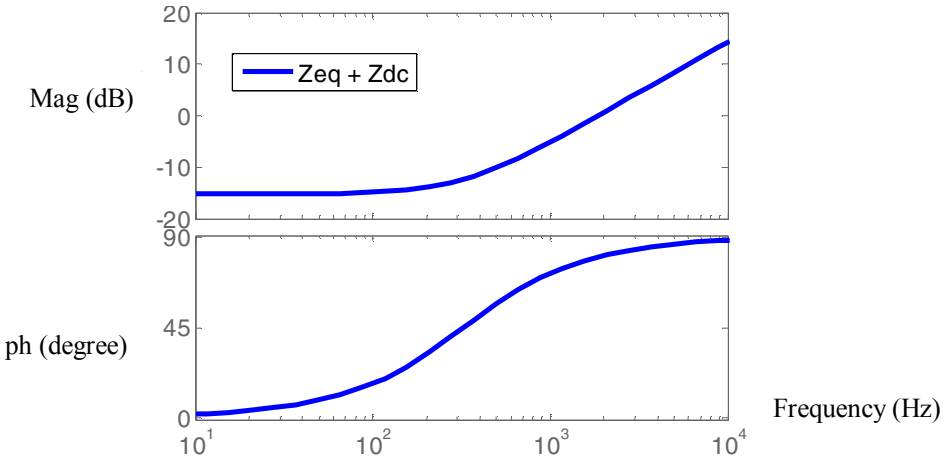


Figure 6-14 Output impedance of generator and rectifier with output filter inductor

The Thevenin's equivalent circuit is ready to use for resonance study when the harmonic source and its impedance are obtained.

6.2.4.3 Thevenin's equivalent circuit verification

The verification of the Thevenin's equivalent circuit is similar to that of the Norton's equivalent circuit for the VSI-MD. The equivalent impedance Z_{eq} is first verified by plotting the transfer function of the dc bus voltage to the harmonics from load side as

$$\frac{V_{c0}}{i_{in}} = \left(Z_{eq} + Z_{L0}\right) // \, Z_{c0} \cdot \frac{R}{\left(Z_{eq} + Z_{L0}\right) // \, Z_{c0} + R} \cdot \tag{6-9}$$

The verification system is given in Figure 6-15. To focus on the rectifier, the VSI-MD is substituted by a resistive load to eliminate the nonlinear behavior of the load. An ideal current source with frequency f_p is in parallel with the load to stand for the load

harmonics inserted into the system. A three-phase ideal voltage source is used here instead of the generator in order to verify the method itself.

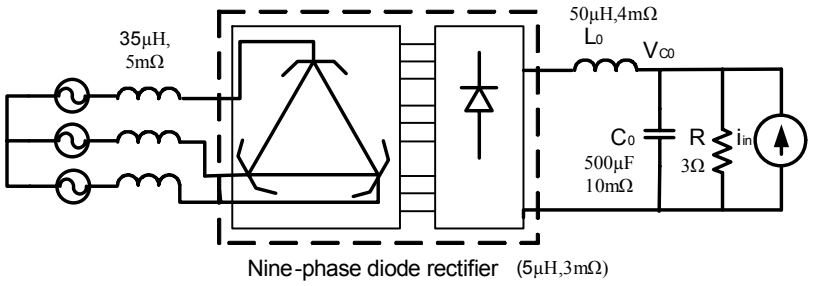


Figure 6-15 Verification of Z_{eq}

By changing the frequency f_p of the harmonic source i_{in} in the detailed switching model, the transfer function of V_{CO}/i_{in} can be obtained. It can also be derived from a linear system by substituting the input voltage source and the diode rectifier with Z_{eq}. The model of Z_{eq} for resonance is valid if two transfer functions match each other.

Figure 6-16 gives the verification result. Four curves are compared in this figure to show Z_{eq}'s effect on the transfer function. Besides the transfer function from the switching model, the other three curves are all derived from the average model but with different modeling of Z_{eq}. The first curve is derived from getting Z_{eq} directly from the switching model by the user-defined software method. In this case, the transfer function predicted by the average model and the switching model are exactly the same. The second curve is from deriving Z_{eq} by using the linear relationship of the transformer to model the feeder inductance. There is some discrepancy between this curve and the transfer function from the switching model, but the two transfer functions still match well enough. The error of Z_{eq} from mathematical derivation has been analyzed in Chapter 5. The third curve is derived from modeling the feeder's inductance by the nonlinear current

relationship of the autotransformer, which has been adopted to derive the equivalent commutation inductance. In Figure 6-16, there is a large discrepancy in this case. Obviously, the last model of Z_{eq} is not correct. This further proves the method to model the feeder inductance in the small-signal model of the diode rectifier in Chapter 5.

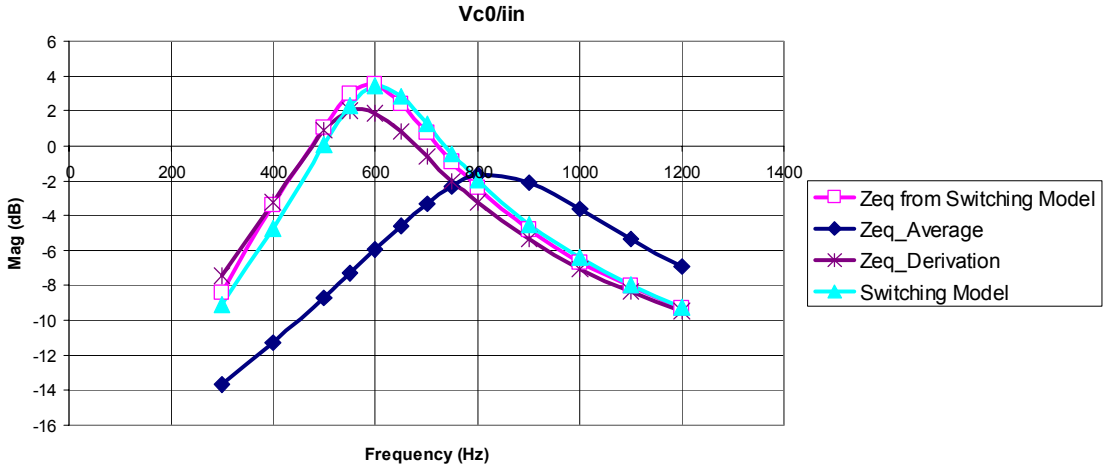


Figure 6-16 Verification result of Z_{eq}

When modeling Z_{eq}, the generator's dynamics are ignored and its subtransient impedance is added into the feeder's inductance. Figure 6-17 gives the simulation result when the input voltage source is the generator and its subtransient impedances are used to model the equivalent output impedance. The simulation result shows that the subtransient impedances are good approximations to model the impedance.

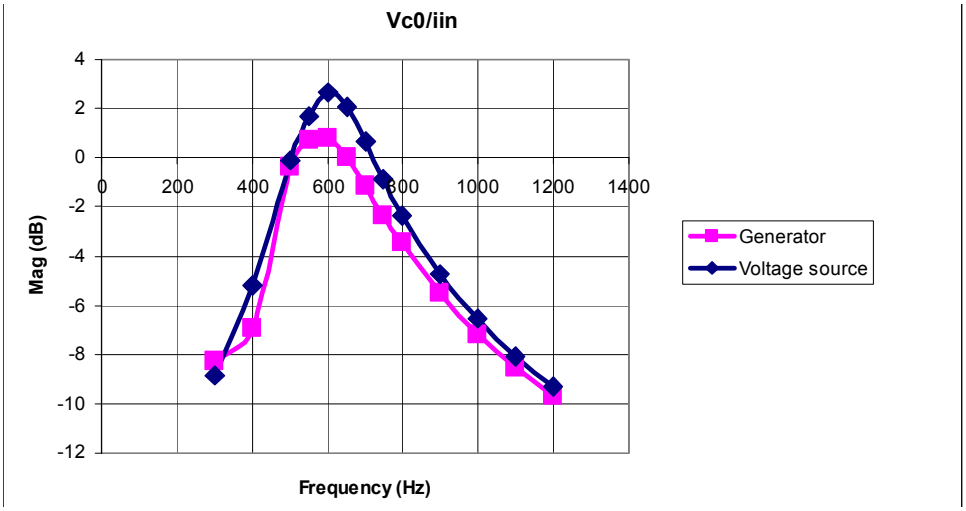


Figure 6-17 Generator vs. Voltage source

After Z_{eq}'s verification, the modeling method for the equivalent source in the Thevenin's circuit, V_d, is verified. V_d is usually trivial under normal operating conditions, which is the same as I_{in} in the Norton's equivalent circuit of the VSI-MD. In order to test the validation of the modeling method, a three-phase voltage source with frequency f_p is added into the system. It is in series with the original voltage source to represent the possible harmonics in this block. The harmonic source V_d from the rectifier side is modeled by open-circuit method in Figure 6-13. Doing Fourier analysis of V_{out} gives the harmonics from the rectifier side.

The system in Figure 6-18 is used to verify the harmonic source model. The transfer function of V_{C0}/V_d is obtained from both the mathematical derivation and the switching model. For the mathematical derivation, the transfer function from the Thevenin's equivalent circuit is

$$\frac{V_{c0}}{V_d} = \frac{Z_{c0} // R}{Z_{eq} + Z_{L0} + Z_{c0} // R}. \tag{6-10}$$

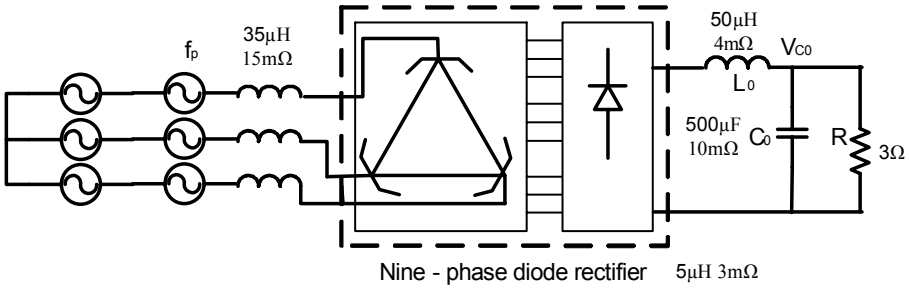


Figure 6-18 Verification of V_d

In (6-10), Z_{eq} from the switching model is used here to minimize its error on this validation. The transfer function from the switching model is obtained by changing f_p in Figure 6-18 and doing Fourier analysis of V_{C0}. The generator is replaced with a three-phase voltage source to minimize the error of Z_{eq}. When the harmonic source V_d are determined under each f_p, the transfer function can be plotted. The model of V_d is valid if these two transfer functions match with correct Z_{eq}. The verification result is given in Figure 6-19. Two transfer functions match well enough for resonance study.

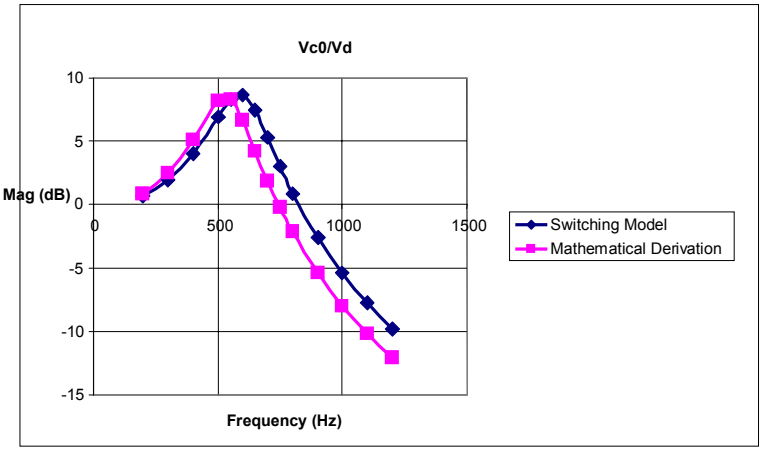


Figure 6-19 Verification result of V_d

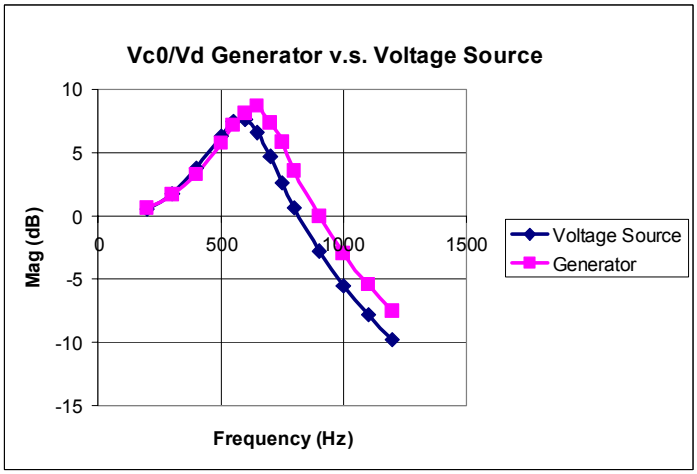


Figure 6-20 Verification result of V_d

The transfer function with a generator is plotted for completeness of the work. It is compared with the transfer function with the voltage source and 10μH, 1mΩ line impedance in Figure 6-20.

Concurrently with this verification procedure, the system resonance that might be caused by the generator and the rectifier is investigated. The resonance frequency and amplification can be figured out in Figure 6-19.

6.3 Resonance study

With the Norton's and Thevenin's equivalent circuits, the system is linearized as Figure 6-3. Two main aspects determine whether the resonance in a system should be considered or not: when the resonance will occur and how much it will affect the system. It depends both on the system characteristics, including the damping factor and the resonance frequency, and the existence of the harmonic source. When the harmonic

frequency is equal or close to the system resonance frequency and the damping factor is not large enough, resonance can cause a catastrophic result.

In above sections, the gain of transfer functions is used to study the resonance as well as to verify the model's correctness for each individual block. It is known that the transfer function is also utilized for the stability study in dc distribution power system. The relationship between the resonance and stability is investigated in this section.

Another study undertaken here is to show the variation of equipment parameters effects on system resonance. The dynamics of the motor drive and the generator are discussed in terms of resonance.

6.3.1 Relationship between resonance and stability

Most resonance studies are only concerned with the gain of transfer functions, which can provide sufficient information, such as the resonance frequency and its amplification, while the phase plot is not necessary. But sometimes, this can lead to confusion of stability with the resonance problem. One example is given below.

A simple circuit is given in Figure 6-21. The load Z is the input impedance of the VSI-MD in Figure 6-7, representing the constant power load. Two different sets of parameters for the filters are listed in Table 6-1. The resistors are the parasitic parameters of the inductors and capacitors. When there are no such parasitic resistors, the system has a peak on its gain plot of the transfer function V_{C0}/V_{in} in both cases. While adding those parasitic resistors in, that peak is well-damped. The corresponding transfer functions are plotted in Figure 6-22.

Table 6-1 Filter parameters for simple linear system

	L_0	R_{L0}	C_0	R_{C0}
set I	20mH	200mΩ	1.5F	150mΩ
set II	20μH	200mΩ	0.15F	150mΩ

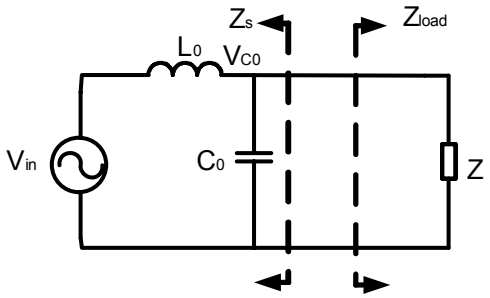
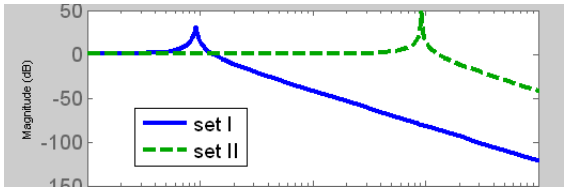
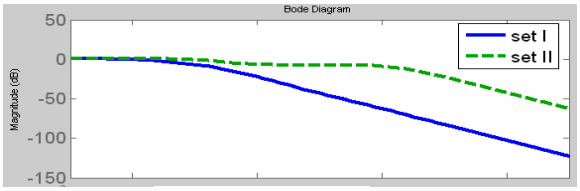


Figure 6-21 Simple linear system schematic



Frequency (Hz)

(a) No parasitic resistors



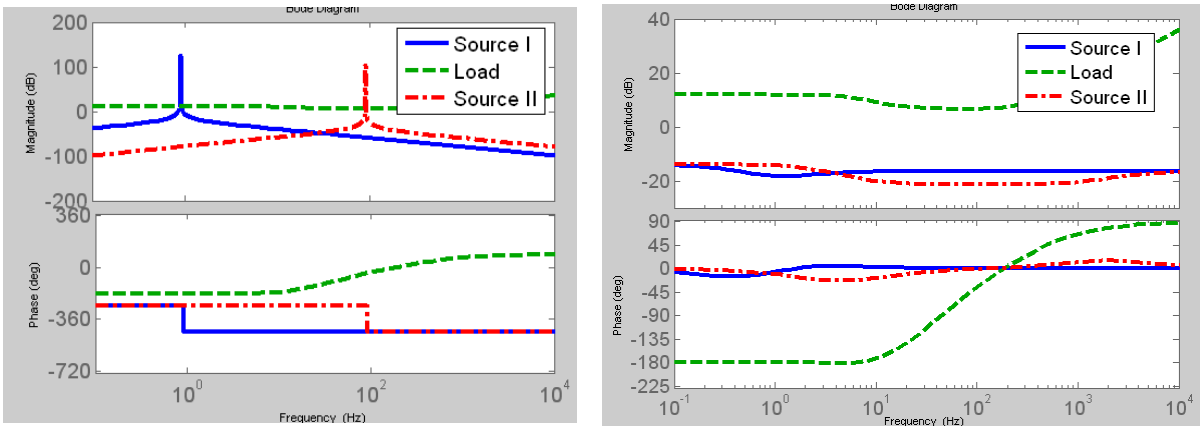
Frequency (Hz)

(b) With parasitic resistors

Figure 6-22 Gain of V_{C0}/V_{in}

Although these cases both look like a resonance problem for this linear system, they are actually different issues. For convenience, the impedance $L_0//C_0$ is denoted as Z_s and Z_{load} is Z. For the first case, Figure 6-23 (a) shows that Z_s and Z_{load} interfere with each other at -180°, which makes the system unstable. In the second case, although Z_s and Z_{load} interfere, there is some phase margin and the system is stable. Therefore, the second case is the resonance in the system, while the first case is the stability problem. If only the

gain of the transfer function is taken into consideration in the resonance study, the system stability has to be investigated prior to the resonance study.



(a) No parasitic resistors **(b) With parasitic resistors**

Figure 6-23 Stability study of Z_s and Z_{load}

By the definition of Z_s and Z_{load}, the transfer function of the above system can be expressed as

$$\frac{V_{C0}}{V_{in}} = \frac{1}{1+Z_s/Z_{load}} \cdot \frac{1}{1+Z_{L0}/Z_{C0}} = G_{stability}(s) \cdot G_{filter}(s) \tag{6-11}$$

There are two terms in (6-11). The first term, $G_{stability}(s)$, is the stability criterion for dc power system, while the second term, $G_{filter}(s)$, is related to the filter parameters. The resonance behavior of the system depends on both of them.

To verify this relationship between stability and resonance in the rectifier-inverter system in Figure 6-2, stability criterion must be modified because it has two dc nodes [83]. The system can be represented by a generic schematic in Figure 6-24, which involves a two-port network for the filters denoted as C-converter, a source block denoted as S-converter and a load block denoted as L-converter.

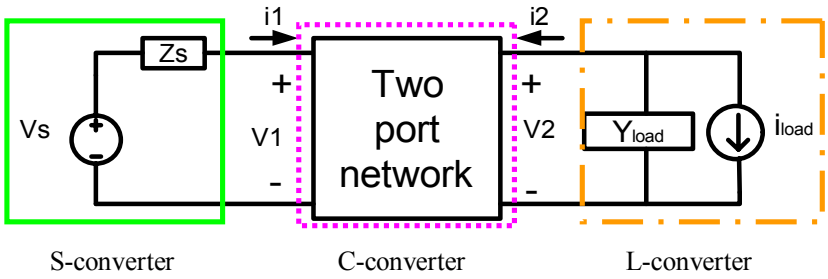


Figure 6-24 DC power system with two-port network

The impedances of these blocks are defined as

$$Z_s = \frac{V_s}{i_1}, \qquad Y_L = \frac{V_2}{i_{load}}, \qquad \text{and} \qquad \begin{bmatrix} V_2 \\ i_1 \end{bmatrix} = \begin{bmatrix} a_{11} & a_{12} \\ a_{21} & a_{22} \end{bmatrix} \cdot \begin{bmatrix} V_1 \\ i_2 \end{bmatrix}. \tag{6-12}$$

In order to study the stability of this system, two converters should be combined together, either S- and C-converter or C- and L-converter. When S- and C-converter are combined together, the new equivalent source impedance becomes

$$Z_{seq} = a_{12} - a_{11} \cdot Z_s \cdot \frac{a_{22}}{1 + a_{21} \cdot Z_s}. \tag{6-13}$$

The stability criterion of the system is

$$1 + Z_{seq} \cdot Y_L = \frac{1 + (a_{12} \cdot a_{21} + a_{11} \cdot a_{22}) \cdot Y_L \cdot Z_s + a_{12} \cdot Y_L + a_{21} \cdot Z_s}{1 + a_{21} \cdot Z_s}. \tag{6-14}$$

If combines the C- and L-converter, the new load impedance is

$$Y_{Leq} = a_{21} - a_{22} \cdot Y_L \cdot \frac{a_{11}}{1 + a_{12} \cdot Y_L}, \tag{6-15}$$

and the stability criterion becomes

$$1 + Z_s \cdot Y_{Leq} = \frac{1 + (a_{12} \cdot a_{21} + a_{11} \cdot a_{22}) \cdot Z_s \cdot Y_L + a_{12} \cdot Y_L + a_{21} \cdot Z_s}{1 + a_{12} \cdot Y_L}. \tag{6-16}$$

Comparing equations (6-14) and (6-16), it can be seen that the poles that determine the system stability are the same regardless of the combination.

Based on this statement, our system can combine either the source and the filter or the filter and the load, which are defined in Figure 6-25 as

$$\begin{aligned} Z_{s0} &= (Z_{L0} + Z_{eq}) // Z_{C0}, & Z_{s1} &= Z_{C1} // (Z_{L0} // Z_{C0} + Z_{C1}) \\ Z_{loaad0} &= Z_{L1} + Z_{in} // Z_{C1}, & Z_{load1} &= Z_{\text{in}} \end{aligned} \tag{6-17}$$

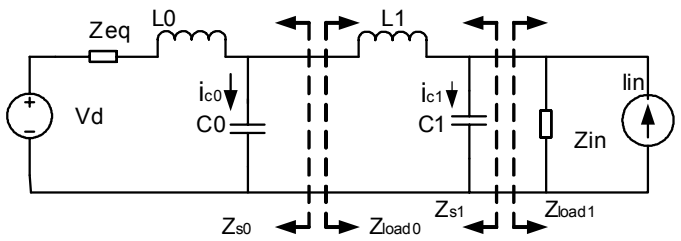


Figure 6-25 Impedance definition of rectifier-inverter system

Transfer functions from harmonic sources to bus capacitors are derived for resonance study. When considering the harmonic source from the rectifier side V_d, it is assumed that I_{in} does not exist. The transfer function of the dc bus voltage to V_d is expressed as

$$\begin{aligned} \frac{V_{c0}}{V_d} &= \frac{1}{\frac{Z_{L0}+Z_{eq}}{Z_{c0}}+1} \cdot \frac{1}{1+\frac{Z_{s0}}{Z_{load0}}} = G_{stability}(s) \cdot G_{filter}(s) \\ &= \frac{(Z_{L0}+Z_{eq}+Z_{C0}) \cdot (Z_{L1} \cdot Z_{C1} + Z_{L1} \cdot Z_{in} + Z_{C1} \cdot Z_{in})}{(Z_{L0}+Z_{eq}+Z_{C0}) \cdot (Z_{L1} \cdot Z_{C1} + Z_{L1} \cdot Z_{in} + Z_{C1} \cdot Z_{in}) + (Z_{L0}+Z_{eq}) \cdot Z_{C0} \cdot (Z_{C1}+Z_{in})} \cdot \frac{Z_{C0}}{(Z_{L0}+Z_{eq})+Z_{C0}} \end{aligned} \tag{6-18}$$

In (6-18), the additional poles from the "filter part" $G_{filter}(s)$ are cancelled by the zeros in $G_{stability}(s)$, which means that the resonance frequency of the system only depends on the poles of $G_{stability}(s)$. The filter parameters will introduce additional zeroes into the transfer function, which changes the damping factor.

For other transfer functions, like V_{C0}/I_{in}, the same conclusion is reached. Therefore, the stability has a close relationship with resonance in this system. This relationship can

be summarized as follows: 1) in order to use the gain of the transfer function for resonance prediction, stability has to be investigated before the resonance study; 2) the poles in stability study determines the resonance frequency of the system; and 3) the filter parameters along with the Norton's and Thevenin's equivalent impedances are needed to predict the amplification at the resonance frequency.

6.3.2 Bandwidth of VSI-MD on system resonance

When deriving the Norton's equivalent circuit, it is found that the input impedance of the VSI-MD will influence the system resonance significantly. In this section, this topic is discussed in detail, while considering the harmonics from the rectifier side. The system to verify Y_{in} (Figure 6-8) is used here.

The dynamic behavior of a closed-loop VSI-MD is determined by the bandwidth of the control loop. The impedance of the Norton's equivalent circuit Z_{in} has a close relationship with ω_s and ω_i, which can be seen clearly from equation (6-5). Since ω_i is 10 times ω_s, we use ω_s to refer to the bandwidth in this work. The Z_{in}'s variation with different ω_s is plotted in Figure 6-26. If ω_s is very high, the converter behaves like an ideal constant power load (CPL), given in Figure 6-26 as the blue dashed line. For stability study, the source impedance Z_{sn} is plotted in the same figure as the green dashed curve, which is composed of two *LC* filters.

The transfer function for resonance study changes with different Z_{in}. If the harmonics are from the rectifier side, the Bode plot of V_{C0}/V_d is given in Figure 6-27 while ω_s changes from 3Hz to 70Hz. ω_s is set as 1kHz to represent an ideal CPL.

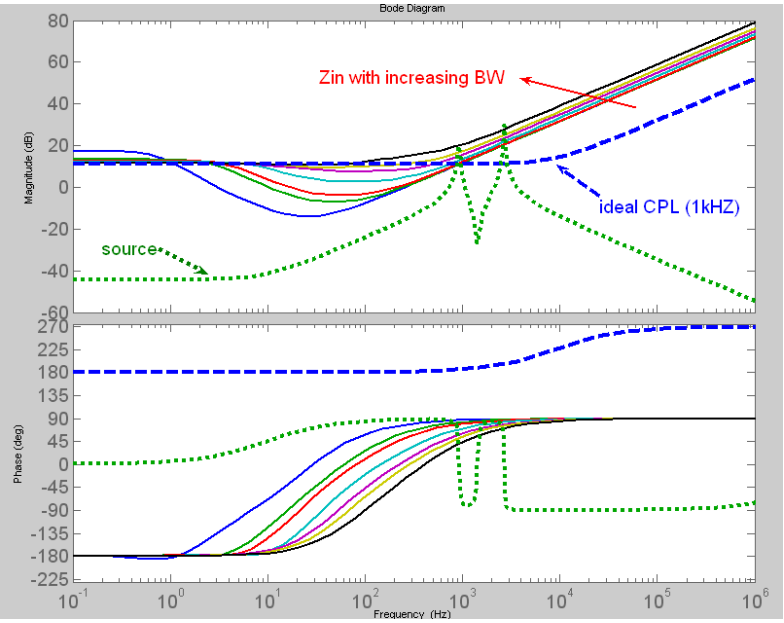


Figure 6-26 Impedance of VSI-MD variation with control bandwidth

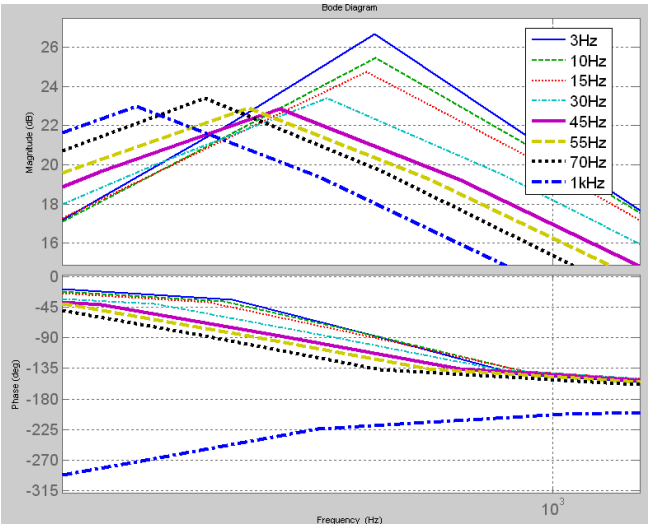
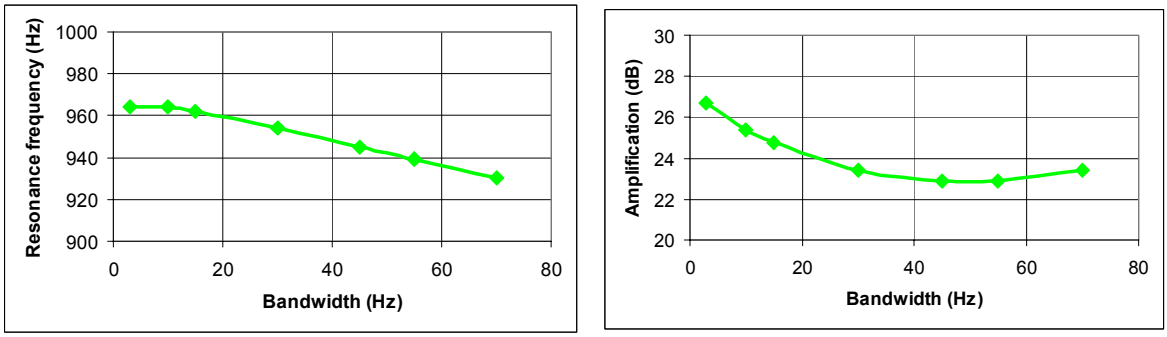


Figure 6-27 Bode plot of V_{C0}/V_d with different Z_{in}

The resonance frequency increases when ω_s decreases, but the variation is limited. The damping factor does not change monotonously. The resonance frequency and the corresponding amplification for different Z_{in} are shown in Figure 6-28. Under this set of system parameters, the amplification of the harmonics at the resonance frequency reaches

the minimum value when ω_s is 45Hz. The resonance of the system might become severe other than this bandwidth. If the system parameters are changed, an optimum bandwidth for minimum amplification still exists, although it might be a different number.

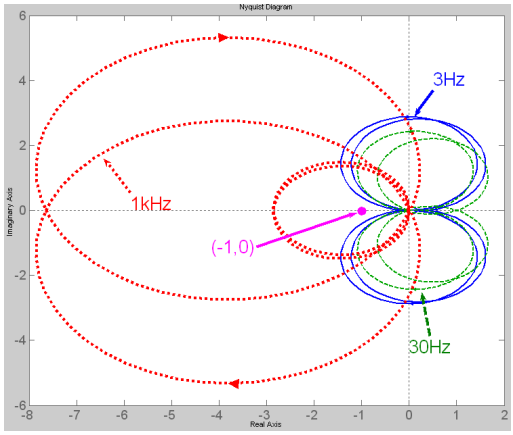


(a) resonance frequency v.s. bandwidth **(b) corresponding amplification v.s. bandwidth**

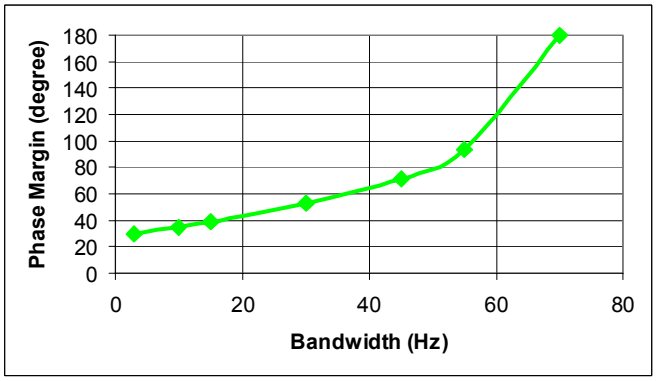
Figure 6-28 Control Bandwidth influence on resonance

In Figure 6-26, the interaction between the source and the load impedance changes with different controller bandwidth, which influences the stability. The stability criterion of this system is the transfer function of $Z_{sn} \cdot Y_{in}$, where Z_{sn} is the source impedance and Y_{in} is the load admittance. Two Nyquist plots of $Z_{sn} \cdot Y_{in}$ are shown in Figure 6-29 (a) where ω_s is 3Hz, 30Hz and 1kHz. When ω_s is 1kHz, the system will be unstable, which is also predicted in Figure 6-26. Figure 6-29 (b) gives the variation of the phase margin of $Z_{sn} \cdot Y_{in}$ with ω_s . The phase margin becomes higher with increasing bandwidth.

It can be concluded that the controller bandwidth of this VSI-MD should be designed around 45Hz to get minimum amplification of the harmonics. However, the phase margin does not reach its maximum value under this bandwidth. In other words, a more stable system does not guarantee that this system will have less resonance. The system resonance phenomenon cannot be predicted through stability study only.



(a) **Nyquist plot**



(b) **Phase margin**

Figure 6-29 Control Bandwidth influence on stability

6.3.3 Generator's dynamics on system resonance

When modeling the equivalent impedance Z_{eq} in the Thevenin's equivalent circuit for the generator and the nine-phase diode rectifier, it is difficult to give the mathematical derivation of Z_{eq} that includes a close-loop generator. Instead, the generator's open-loop subtransient impedance is used for approximation. This approximation is investigated in this section.

To have different controller's bandwidth, the zero in voltage control loop transfer function has four different values, which are 1/100 (controller 1), 1/50 (controller 2), 1/150 (controller 3) and 1/500 (controller 4) respectively. The open-loop transfer functions of the generator RMS voltage to its exciter's voltage for corresponding controllers are given in Figure 6-30, whose bandwidth is from 38Hz to 105Hz.

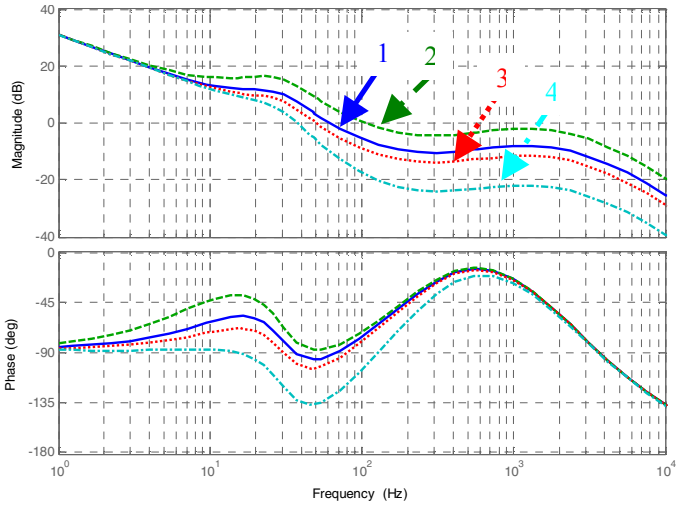
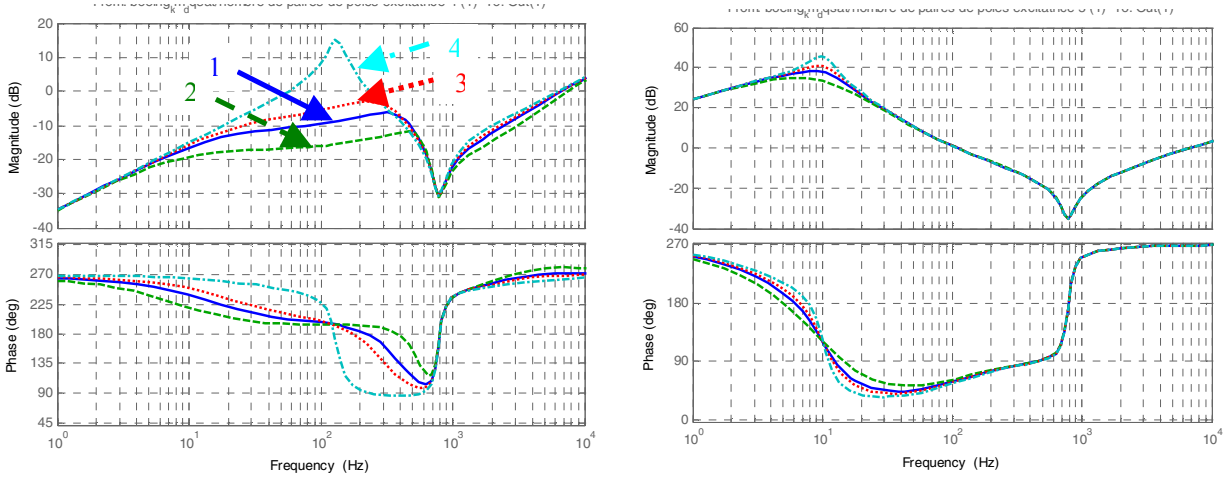


Figure 6-30 Generator open-loop transfer function V_{rms}/V_{ex}

The output impedances of the generator in *dq*-axes are given in Figure 6-31.



(a) Z_{dd} **(b) Z_{qq}**

Figure 6-31 Generator close-loop output impedance

To observe the generator's controller influence, the transfer function for resonance study is obtained using the switching model. The method for Z_{eq}'s verification in Figure 6-15 is used here. Figure 6-32 shows the results with different generator controllers compared with the result using an ideal voltage source. To compare them fairly, the

feeder's inductance in series with the generator is reduced to 10μH in order to keep their summation the same as the feeder's inductance with ideal voltage source 35μH. From Figure 6-32, we can see that the transfer functions are almost the same with different controllers of the generator. This means that the generator's controller does not affect the system resonance behavior, which is different from the motor drive. Therefore, it is valid to use generator's open-loop subtransient impedance as the approximation for system resonance study.

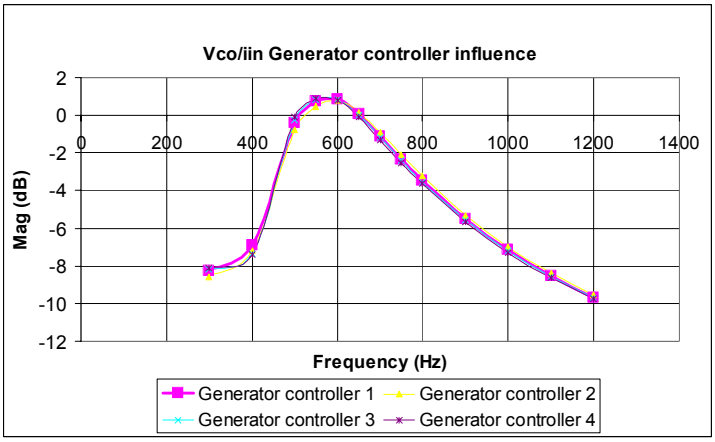


Figure 6-32 Generator controller's influence on the resonance

6.4 System simulation

The resonance of each individual block has been investigated in previous sections. To verify the resonance for the entire system, this section includes Saber simulations for the system in Figure 6-2. The controller bandwidth of the VSI-MD is chosen to be 30Hz here.

The transfer functions V_{c0}/V_d and V_{c0}/i_{in} from equivalent circuits are given in Figure 6-33. If there is a 600Hz harmonic source either from the rectifier or the VSI-MD side,

the dc bus will experience resonance. When the harmonic frequency becomes 2.7kHz, the dc bus will have resonance if it comes from the VSI-MD side, while it will not have such a problem if the harmonics come from the rectifier side.

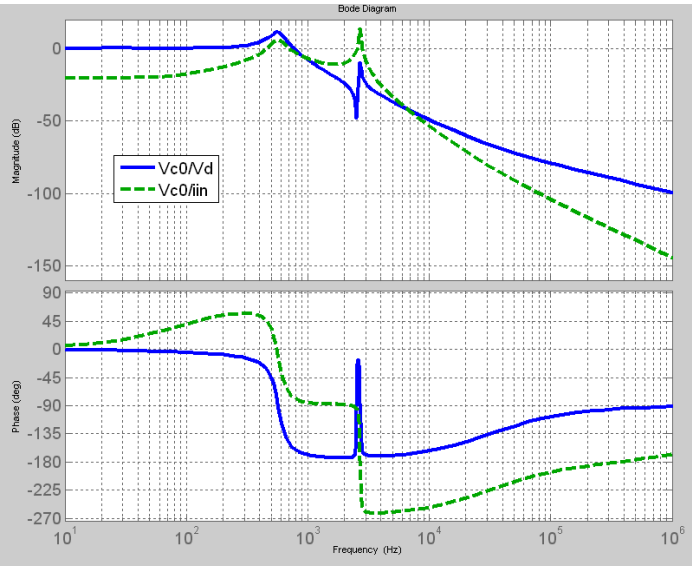
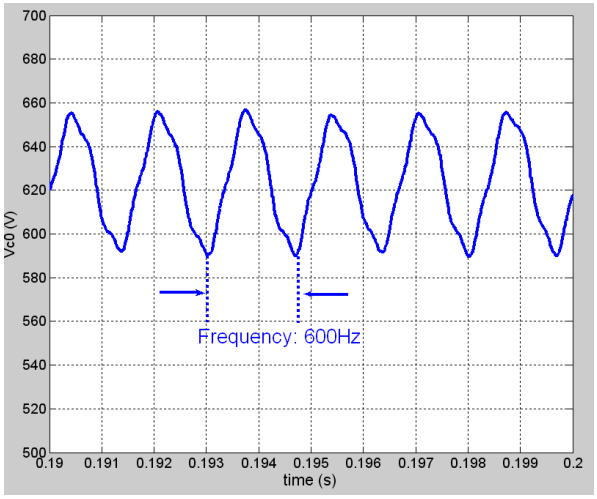


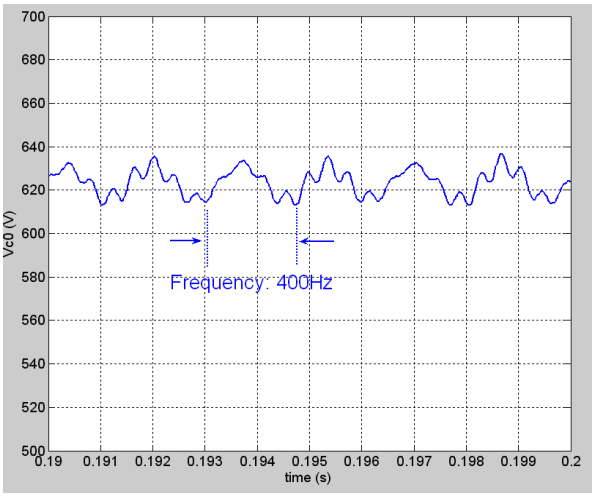
Figure 6-33 Transfer functions of entire system

Several simulation scenarios are given to verify the predictions. A three-phase voltage source with 5V amplitude is in series with the generator to represent the harmonics from the rectifier side, similar to the system in Figure 6-18. Using the method in section 6.2.4, the magnitude of the equivalent voltage source in the Thevenin's model is around 9V. From Figure 6-34 (a) and (b), it can be seen that resonance will occur on the dc bus at 600Hz. There is no resonance on the dc bus voltage at 2.7kHz except for the ripples. The harmonics from the VSI-MD are verified in the same way. The magnitude of the equivalent current source in the Norton's equivalent circuit is 9A when the amplitude of the inserted current source is 15V. The corresponding dc voltage at 600Hz and 2.7kHz waveforms are given in Figure 6-34 (c) and (d).

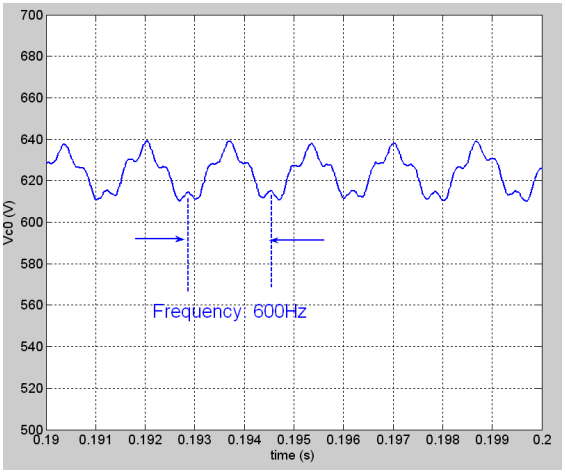
The figure shows that the harmonics at 600Hz from the rectifier side have a more severe effect on the system resonance than the harmonics from the inverter side. It can be concluded that the linearized system can predict the resonance in such a system well. This prediction provides design guidance for system parameter selection, especially for the filter design.



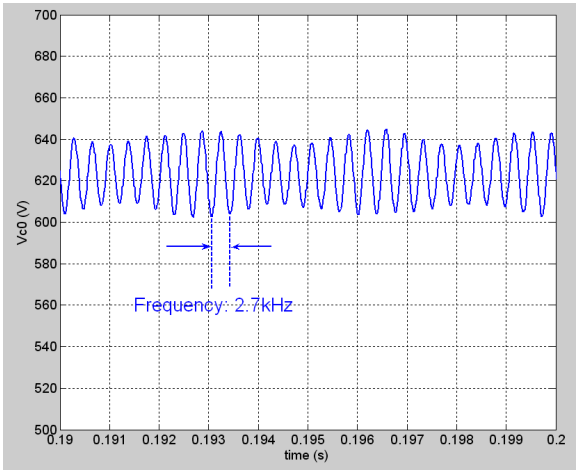
(a) 600Hz harmonics from the rectifier



(b) 2.7kHz harmonics from rectifier



(c) 600Hz harmonics from VSI-MD



(d) 2.7kHz harmonics from VSI-MD

Figure 6-34 DC bus voltage V_{C0} under different conditions

6.5 Summary

The resonance problem is studied for a system that includes a generator, a nine-phase diode rectifier and a VSI-MD. The nonlinear blocks of the rectifier and the VSI-MD are modeled using the Thevenin's and the Norton's equivalent circuits. The equivalent impedances can be derived using average models, and the equivalent sources are simulated from switching models in Saber through either short- or open-circuit. The transfer function from the harmonic sources to the dc bus voltage is derived based on the linearized system to predict the resonance phenomenon. Simulation results using the detailed switching model verify the prediction.

Stability has to be investigated before resonance in a dc system. A more stable system does not guarantee more damping of the harmonics. In this system, the bandwidth of the motor controller influences the resonance significantly, while the generator's controller does not influence much. There exists an optimum controller bandwidth of the motor drive to have minimum amplification of harmonic sources.

CHAPTER 7 SYSTEM OPTIMIZATION

7.1 Introduction

In Chapter 6, the average model of the diode rectifier was applied into system resonance study, where the impedance of the converter is required. Another aspect of the average model application is given in this chapter, which is for system optimization.

For an aircraft power system, it is required that each component in the system be as smaller and lighter as possible. Traditional design relies mostly on the designer's experience and intuition, which may result in a sub-optimal design. Adopting mathematical optimization can help to achieve a better design. The average model of the switching power converter is necessary for optimization because the power converters have to be expressed by equations required by commercial optimization software.

The nine-phase diode rectifier includes an autotransformer, a diode rectifier and its output filter. Mathematical optimization of the power transformer has been proposed in [92], and the optimization for the filter is given in [90]. They can be applied to our system with no difficulty. However, in an aircraft system, optimization involving both the electronics circuit and the load is more important than optimizing the converter itself. The diode rectifier usually provides the bus voltage of the power system, which does not interact with the load directly. Therefore, instead of optimizing the rectifier, a switching power amplifier with a piezoelectric (PZT) actuator as its load is chosen to show the optimization procedure.

The optimization can be classified as continuous optimization or discrete optimization in terms of the design variables' type. To make the optimization more realistic, discrete optimization is chosen in this work to allow the choice of the components off the shelf. Genetic algorithm (GA), one of the discrete optimization methods, is used for the optimization. The choice of objective function, design variables and calculation of constraints are proposed for the first time. The average model of the power amplifier is developed in MATLAB/Simulink, along with the PZT model for optimization.

7.2 System modeling

A simple system in Figure 7-1 is studied to show the optimization procedure. PZT is a material that can change its shape in response to an electric field. When the output voltage of the amplifier varies, the movement of the PZT actuator will pass to the mechanical structure. The sensor gets the feedback signal from the structure. The controller generates the switching signals needed for the amplifier to amplify the reference signal, which should be high enough for the maximum deflection of the PZT actuator.

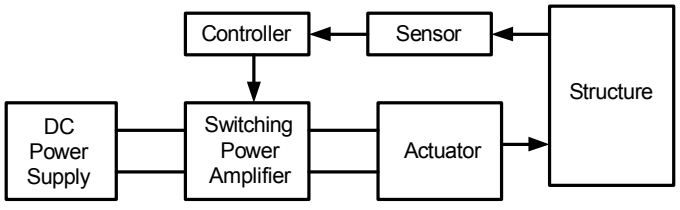


Figure 7-1 Optimization system

Before system optimization, both the driving amplifier and the actuator need to be modeled. To be executable with optimization software, the models are described using

mathematical equations. For the switching power amplifier, an average model is developed to meet this requirement. The system models are developed using MATLAB/ Simulink for optimization. This model is valid when the frequency is below half of the switching frequency, which is the case in this work.

7.2.1 Switching power amplifier

The PZT actuator has capacitive characteristics, so it is simplified as a 12.15μF capacitor when designing the driving amplifier circuit. The output voltage required by the actuator is a sinusoidal waveform with the magnitude of 100V.

In [88], a buck circuit is proposed for a switching power amplifier to drive a PZT actuator. This method is not feasible when the input dc voltage is lower than the output voltage of the power amplifier. In such cases, a two-stage circuit topology is proposed [89]. The first stage of the circuit is to boost the dc voltage and the second stage is the power amplifier. For the first stage, two common step-up power converters are the boost circuit and the flyback circuit. The boost circuit is not chosen here because its efficiency drops rapidly when the duty cycle is high, which limits the circuit application. In addition, the flyback circuit can provide multiple outputs using a minimum number of parts. This is a notable advantage for our design, because the first-stage circuit must provide both the high dc bus voltage and the ±15V voltage for chips of the second-stage circuit. The complete circuit topology is given in Figure 7-2. To give sufficient margin for the buck converter, V_{dc} is controlled to be 300V.

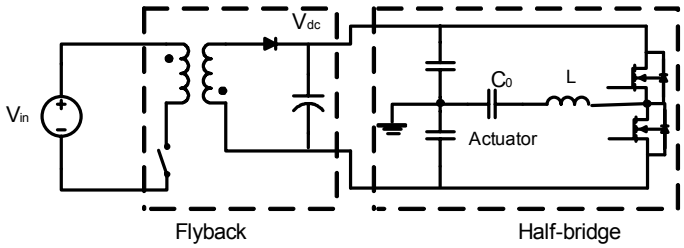


Figure 7-2 Power amplifier circuit topology

Here, the flyback circuit is designed to operate in the discontinuous-current-mode (DCM). In the DCM, all the energy stored in the primary winding of the transformer during the on time is completely delivered to the secondary side before the next cycle, resulting in small transformer size. The switching frequency of the flyback circuit is chosen to be 100kHz, which is a typical value. There are two main designs in the flyback circuit: the transformer and the control loop for the duty cycle. These two designs will affect the amplitude and the stability of the output voltage of the flyback circuit.

The transformer of the flyback circuit should be designed first. The detailed design procedure is referred to [89]. The turns ratio of the transformer is designed to be 25, and its magnetizing inductance is 10μH. For the controller, a dual loop control scheme is adopted: a voltage control loop as the outer loop and a peak current control loop as the inner loop, shown in Figure 7-3. This control can have current-limiting as well as output voltage control.

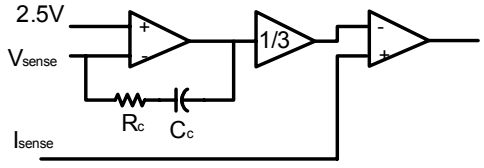


Figure 7-3 Control loop for flyback converter

The second stage is a buck circuit to amplify the reference signal. Since the output voltage varies between negative and positive, the original buck circuit cannot be used. A half-bridge circuit is used instead in this design for fewer switching components and less power consumption.

In this topology, the energy can flow back to the flyback circuit through the diodes in parallel with the switches. The energy is then stored in the output capacitor of the flyback circuit. The resonant tank, which is composed of L and C_0, has a role of storing the energy temporally. Then a large amount of reactive power can be sent back to the dc power supply, resulting in higher efficiency than the linear amplifier [87].

The switching frequency of the half-bridge circuit is set to be 100kHz. Compared with that, the frequency of the reference signal is so low that the reference signal can be treated as a dc signal in each switching period. When the half-bridge circuit is averaged within one switching period, its equivalent circuit is the same as the buck converter, which is shown in Figure 7-4. This model is developed in MATLAB/Simulink for optimization.

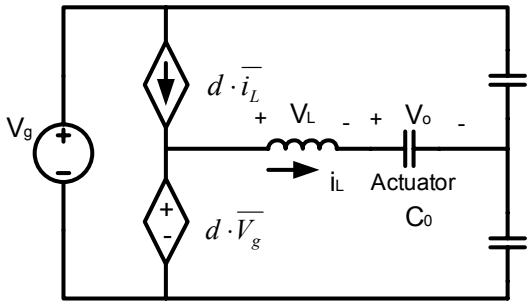


Figure 7-4 Average model of half-bridge circuit

The small-signal model of the half-bridge circuit is derived from the average model using the standard perturbation procedure [89]. The control loop for the half-bridge

circuit is designed based on the small signal model. It is a dual loop with average current control as the inner loop, as shown in Figure 7-5.

The bandwidth of the controller is required to be 10 Hz for the load. A sinusoidal signal with a magnitude of 3.3V is chosen to represent the reference signal.

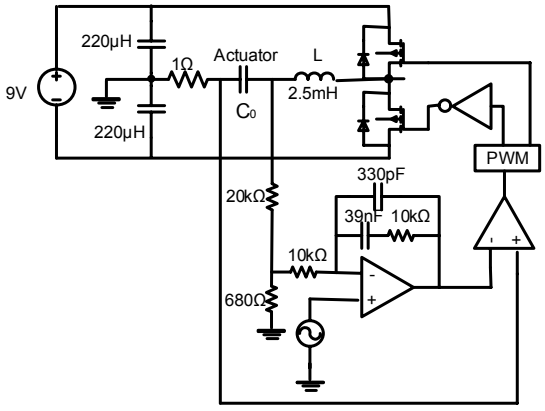
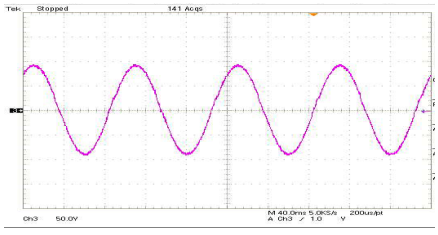
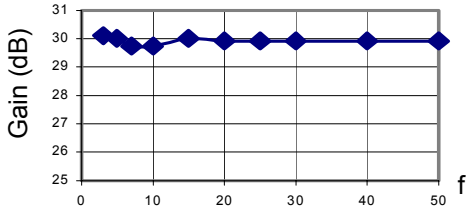


Figure 7-5 Half-bridge circuit with controller

The flyback circuit and the half-bridge circuit are fabricated and tested. Using a 9V dc power supply as the input, 12.15μF capacitor as the PZT actuator, and a 10Hz sinusoidal signal with a magnitude of 3.3V as the reference signal, the output voltage waveform of the power amplifier is shown in Figure 7-6 (a). Figure 7-6 (b) shows the frequency response for this switching amplifier. The gain is 30 well beyond the required bandwidth.



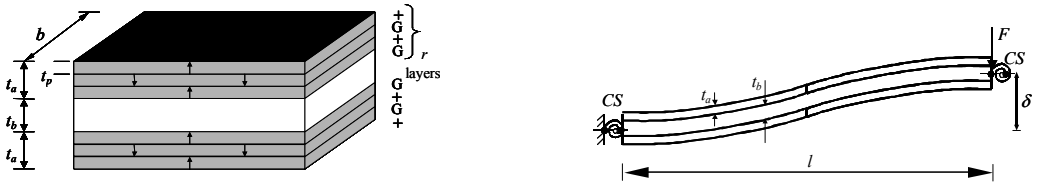


(a) Output voltage **(b) Frequency response**

Figure 7-6 Average model of half-bridge circuit

7.2.2 PZT actuator model

A Recurve actuator is designed as the load. The basic element of the actuator is a cantilever beam that includes one or more active layers of piezoelectric materials. The dimensions of the Recurve cross section are shown in Figure 7-7 (a). Because of a unique electroding/poling scheme, the active layers on either side of the neutral axis strain in the opposite directions over each half of the beam. This causes the beam to bend with positive curvature up to the mid-span and with negative curvature over the other half, producing a relative displacement of the ends of the beam in a direction perpendicular to the beam axis without relative rotation of the ends, as shown in Figure 7-7 (b).



(a) Cross section **(b) Movement**

Figure 7-7 Recurve actuator

When connected with the circuit in Simulink, the actuator is expressed by its transfer function of the output voltage to the electric charge q. A comprehensive description of the finite element model of the Recurve actuator is given in [101]. The assembled system of equations takes the form

$$\begin{aligned} M \cdot \ddot{u} + C_d \cdot \dot{u} + K \cdot u &= q \cdot B + f \\ V &= \frac{1}{C_t} \cdot q - B \cdot u \end{aligned}, \tag{7-1}$$

where M is bending moment, f is the external load vector, C_d is the structural damping matrix, K is the open-circuit stiffness matrix, and C_t is the sum of element capacitances.

The combined system is developed in Simulink/MATLAB. For simplicity, only the half-bridge circuit is considered for optimization because it connects to the load directly. Figure 7-8 gives the schematic including the average model of the half-bridge circuit with its controller and the transfer function of PZT actuator.

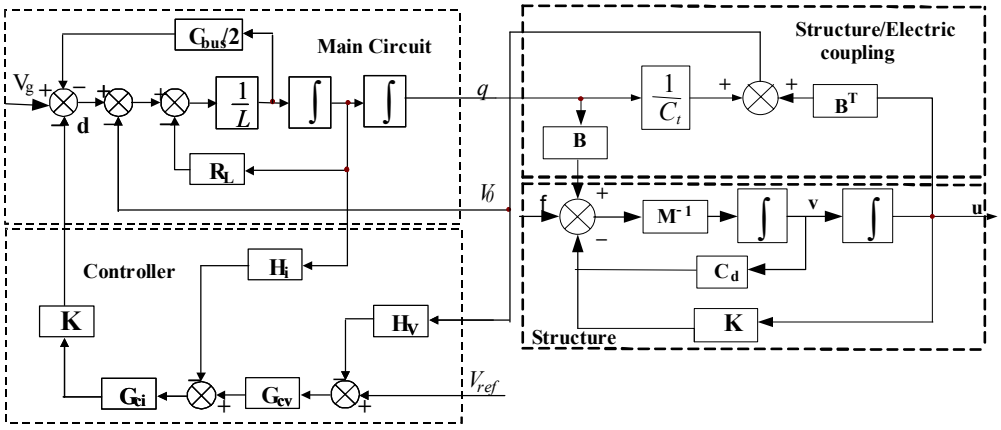


Figure 7-8 System model in Simulink

7.3 Circuit optimization

In this work, the circuit is optimized first. When the PZT actuator has been designed and the value of its equivalent capacitance is obtained, the circuit optimization can design the parameters of the driving amplifier, taking the PZT actuator as a capacitive load. Although it results in a sub-optimal design, the circuit can be studied carefully during the process of the optimization. This process is particularly useful for engineers who are not familiar with power electronics.

7.3.1 Objective function

The design of the driving amplifier for smart actuators presents special challenges when the efficiency, size and weight of the circuit are critical. The weight of the inductor and capacitor, as well as the power dissipation of the circuit has been proposed for this circuit in previous research [96, 97] respectively. These results show that the switching frequency f_s greatly influences the circuit performance. Here it is assumed that the inductor's weight and value are proportional. When the objective function is to minimize the inductor's weight, the inductor value should be minimized. For a fixed peak current, the inductance is proportional to $1/f_s$. If f_s is one of the design variables, it will reach to its allowable maximum value. However, the power dissipation of the circuit will increase almost linearly with f_s due to more power dissipation by MOSFETs. When the objective function is to minimize the power dissipation, f_s is fixed at 100kHz [97]. In order to make a sensible trade-off between the weight and the efficiency in terms of switching frequency, a more suitable objective function is needed.

In hardware development, when the objective function is only the inductor weight, the power dissipation for each MOSFET exceeds 2.75W. Adding a heat sink into the circuit will allow the circuit to operate safely for a long time. Since the weight of the heat sink has a relationship with both the circuit weight and the power dissipation of the MOSFETs, the total weight of the circuit; including the inductor, the bus capacitor and the heat sink for the MOSFET; is a good compromise between the inductor weight and the power dissipation. If f_s goes higher, a larger heat sink is necessary due to greater power dissipation of the MOSFETs, which means the weight of the heat sink will increase. If f_s goes lower, the weight of the inductor will become higher. Therefore, when

the trade-off between the weight and the power dissipation is considered, the proper objective function should be derived as

$$\text{Objective function} = \text{weight of } (\text{inductor} + 2 \times \text{bus capacitor} + 2 \times \text{heat sink}). \quad (7\text{-}2)$$

7.3.2 Design variables

There are two basic types of design variables in the optimization: continuous design variables and discrete design variables. Continuous design variables are real valued variables that are allowed to take on any value between the upper and lower bounds. An example of a continuous design variable is the switching frequency of a switch. Discrete design variables, in contrast, are variables that are only permitted to take on certain pre-specified values. In previous research, continuous variable optimization was applied to this circuit [102]. However, this approach has two shortcomings: first, it can only deal with one type of MOSFET at a time; second, the sizes of the optimized inductor and heat sink are not standard, which may make the hardware development very difficult and expensive. To overcome this, a discrete variable optimization procedure is utilized in this work. Many of the discrete design variables are indices into lists of electronic components.

The half-bridge circuit is comprised of an inductor, two bus capacitors, two MOSFETs with two heat sinks, one dual-loop PI controller, the source and the load. The design variables (both the continuous and discrete) are derived from a consideration of these components. The switching frequency of the MOSFET is also a design variable as illustrated above.

It is assumed that the inductor uses an EE core, whose shape has standard values specified by manufacturers. Each EE core has parameters, such as cross-sectional area A_c, bobbin winding area, mean length per turn, magnetic path length l_m and inductor weight. They will be used when deriving the constraints and objective function. In contrast with the continuous optimization, in which the weight was estimated based on simple assumption, the inductor core weigh is explicitly known. The accuracy of the objective function is therefore improved.

The inductor wire design variable is characterized by its cross-sectional area and the wire weight per unit length. The data are taken from the American Wire Gauge (AWG) specification. The number of turns of the wire is treated as a continuous design variable along with the air gap length of the transformer core.

The dc bus capacitance is a discrete design variable to allow its choice from standard components. Here, we chose the radial lead aluminum electrolytic *M* series capacitors manufactured by Panasonic. The value ranges from 1.0uF to 470uF.

Three different MOSFETs are chosen for the optimization: IRFI740GLC, IRF720 and IRFI734, whose drain-to-source voltages are high enough for the circuit. The corresponding parameters can be found in their datasheets.

The heat sink has many different shapes. In order to simplify the problem, a standard extruded heat sink is used here. The different types of the extrusion heat sink cross sections are set as discrete design variables. Here, we chose from five different types of heat sink cross sections. For each type, the thermal resistance (for 150mm length) and weight per unit length are given in datasheets. The length of the heat sink was considered to be a continuous design variable. The weight of a heat sink is linearly proportional to its

length, but the thermal resistance R_{sa} changes nonlinearly with the length because of the change in the convection coefficient. Figure 7-9 provides a correction factor to calculate the thermal resistance for different fin lengths [105]. A curve fitting to Figure 7-9 was used to compute the correct thermal resistance for arbitrary heat sink length, which is

$$\text{correction_factor} = 3.269 - 0.0263 \cdot length + 8.94 \times 10^{-5} \cdot length^2 - 1.026 \times 10^{-7} \cdot length^3 . \quad (7\text{-}3)$$

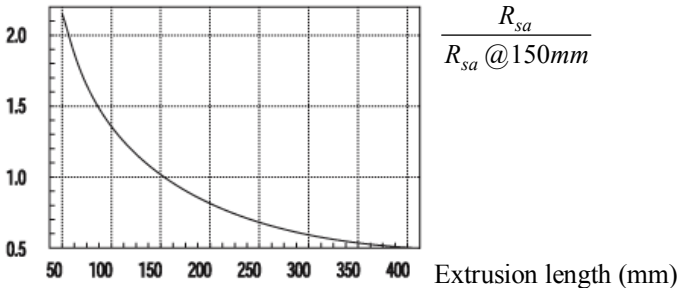


Figure 7-9 Correction factor for R_{sa}

The controller's parameters are continuous design variables. Table 7-1 gives the summary of all the design variables.

Table 7-1 Design variables of circuit optimization

continuous design variables		discrete design variables	
l_g	Airgap length for inductor	L_type	EE core type
n	Number of wire turns for inductor	C_{bus}	Bus capacitance
h_o	Voltage controller gain	AWG	Wire type
ω_z	Voltage controller zero	*SW*	Switch type
ω_p	Voltage controller pole	Heat sink	Heat sink type
h_{ii}	Current controller proportional gain		
f_s	Switching frequency		
len	Length of the heat sink		

7.3.3 Constraints

The constraints for optimizing the half-bridge circuit can be subdivided into four categories: physical constraints of the inductor EE core, performance constraints, system stability constraints, and thermal constraints. All these constraints are necessary and sufficient for this driving amplifier circuit design and are explained below.

1) Physical constraints: The inductor design has limitations due to the available window area of the EE core. Also, the current density of the wire needs to be below the allowable value for copper. To prevent the inductor from saturating, the flux density of the core also should be smaller than 0.3T. The inductance in the circuit is calculated with its parameters as

$$L = \mu_0 \cdot \frac{n^2 \cdot A_c}{l_g + \frac{l_m}{\mu_r}}, \tag{7-4}$$

where μ_0 is the vacuum permeability and μ_r is the relative permeability.

2) Performance constraints: Circuit performance must meet the design's specifications. The bus voltage variation, which determines the output voltage to drive the piezo actuator, must be within 4V. The inductor current ripple is also limited to avoid large peak currents for the inductor. In the frequency domain, the circuit needs a fast response to the disturbance. Since the frequency of the reference signal is less than 10Hz, the crossover frequency of the whole system should be in the range between 10Hz and one-fifth of the switching frequency. Meanwhile, the inductor and the capacitive load can be seen as a low-pass output filter, whose cutoff frequency should be over ten times the reference signal frequency.

3) System stability: This issue needs to be considered when the controller parameters are included in the design variables. Similar to the general system design problem, the phase margin must be over 60° and the gain margin should be over 3dB.

4) The thermal constraints: To make the MOSFET operate safety, the junction temperature T_j of the MOSFET cannot exceed the allowable maximum temperature T_{jmax} [11], which means

$$T_j = T_a + P_{loss} \cdot \left(R_{sa} + R_{jc}\right) < T_{j\max}, \tag{7-5}$$

where P_{loss} is the MOSFET power dissipation and T_a is the ambient temperature. Here, T_a is set to 40°C and T_{jmax} is *100°C*. R_{jc} is the thermal resistance of the MOSFET in its datasheet. R_{sa} is the thermal resistance of the heat sink, which can be calculated using equation (7-3). The calculation of the power loss of the MOSFET can be referred in [97].

7.3.4 Optimization result

The traditional gradient-based optimization is widely used, but it is limited to continuous optimization problem. The stochastic approaches such as genetic algorithms (GA) have been successfully applied to solve both continuous and discrete design variable problems [98].

GAs are probability-based algorithms that utilize the processes of natural selection, and have been experimentally proven to be robust in their application to many search problems [100]. A population of individuals is used to simulate the breeding environment, with each individual representing a single design that is coded using a bit string. In addition to discrete variables, the genetic algorithm used in this work also has the

capability of handling a small number of continuous variables. Continuous variables are modeled directly by using a single real value, and specifying a lower and upper bound for each design variable. Specialized genetic operators are used to manipulate the continuous variable values from each parent design to produce a new value for the resulting child design. Besides of its capability to deal with the integer and continuous number, the stochastic nature of GA increases the possibility of converging to the global optimum design.

Fortran99 is used to realize the GA algorithm with design variables, constraints and objective function. The average half-bridge circuit model modeled in MATLAB has an interface with Fortran99. The actuator is replaced with a 12.15uF capacitor as the load of the amplifier. Table 7-2 gives the optimization result.

Table 7-2 Circuit optimization result

Design variables	optimized value	design variables	optimized value
l_g	21nm	L_type	EE12
N	30	C_{bus}	220μF
h_o	25864	AWG	29
ω_z	810	*SW*	IRF720
ω_p	1,319,905	Heat sink	HS2144
h_{ii}	4.313	Inductance	0.88mH
f_s	261kHz		
Len	10mm		

The optimized circuit has a weight of 4.64 g, which is much lighter than the original circuit. However, in hardware development it is difficult to fabricate such a small inductor. The inductor could be re-designed following the standard magnetic design procedure [39]. The core should be as small as possible, while the inductance value stays the same. This optimization provides a useful guidance for circuit design.

7.4 System optimization

Although circuit optimization can reduce the weight and power dissipation, without consideration of the interaction between the circuit and the load it is still a sub-optimal design. Additionally, the actuator must be designed first so that its equivalent capacitance can be used in circuit optimization. System optimization can solve these problems by optimizing the circuit and the actuator design at the same time. In system optimization, the PZT actuator uses its detailed transfer function instead of a pure capacitor.

7.4.1 Objective function

The inherent trade-off between force and displacement in the design of a Recurve actuator suggests that an energy-related metric should be an appropriate objective function for studying the interaction between the actuator and the circuit. Furthermore, the energy is the direct relationship for the actuator and its driving circuit. The objective function related to the energy is then proposed for the combined optimization. Because the circuit and actuator subsystems are coupled, the energy required by the system cannot be computed separately for each subsystem. Optimization allows for the design of the circuit and actuator simultaneously.

Because of the capacitive characteristic of the actuator, there is both real power and reactive power circulating in the system. The definition of the reactive power Q_e is the maximum value of the product of the input voltage and current. Assuming that the input voltage from the power supply stays constant, the peak input current will determine the reactive power of the system, so the size of the power supply can be reduced by

minimizing the overall reactive power in the combined system. On the other hand, the power dissipation in the system P_{loss} should be reduced as well to achieve high efficiency. Here, the power dissipation occurs only in the drive amplifier, neglecting the power loss in the actuator.

The choice of objective function is important in this type of complicated design problem and the presence of conflicting objectives necessitates a multi-objective approach. In a multi-objective approach, instead of giving preference to one objective, a weighted summation of the different objectives of a min-max approach is employed. The objective function is formulated as a convex combination of the two objectives as

$$f_{obj} = \alpha \cdot P_{loss} + (1-\alpha) \cdot Q_e . \tag{7-6}$$

where α is a scalar weighting factor that can vary between 0.0 and 1.0.

This approach has the advantage of providing the designer with a range of optimal solutions. It also provides the trade-off information between the objectives, which is discussed in the optimization result (Section 7.4.4).

7.4.2 Design variables

The design variables for the driving amplifier are the same as those in Table 7-1, with additional design variables given for the actuator in Table 7-3. A basic feature of the Recurve actuator is its ability to connect a number of basic block elements in parallel and/or in series to tailor the design.

Table 7-3 Design variables for actuator

Continuous design variables		Discrete design variables	
L_b	Recurve length	*n_a*	Number of series Recurve elements
b	Recurve width	*m*	Number of parallel Recurve elements
t_b	Beam substrate thickness	*R*	Number of piezo layers
t_p	Individual piezo layer thickness		

7.4.3 Constraints

The constraints for the half-bridge circuit in the system optimization are the same as the constraints for circuit optimization, which is described in section 7.3.3.

The packaging and performance constraints chosen for the actuator represent typical values for those near-static applications. There are four constraints for the actuator:

1) The minimum free blocked force F_b of the actuator should be larger than user-specified blocked force F_b^*, which is

$$F_a = \frac{F_b}{F_b^*} \geq 1. \tag{7-7}$$

2) The minimum displacement of the actuator δ_f should be larger than the user-specified free displacement δ_f^*, which is

$$\delta_a = \frac{\delta_f}{\delta_f^*} \geq 1. \tag{7-8}$$

3) The actuator is also contained within a user-specified volume. This constrain is expressed as

$$\begin{aligned} L_a &= \frac{2ml}{L^*} \le 1, \quad b_a = \frac{b}{b^*} \le 1 \\ h_a &= \frac{n\left(2 \cdot r \cdot t_p + t_b\right) + \left(n-1\right) \cdot t_s}{h^*} \le 1 \end{aligned} . \tag{7-9}$$

where L^*, b^*, and h^* are user-specified maximum length, width, and height, respectively. The spacing between two series Recurve elements is denoted as t_s, and is assumed to be twice the maximum displacement of an individual Recurve element,

$$t_s = 2 \cdot \delta_f \big/ n . \tag{7-10}$$

4) The piezoelectric material cannot become saturated. The maximum electric field that can be applied to the piezoelectric material without losing its poling characteristics is E_c, which is a material property. For a given applied voltage V, this constraint limits the maximum thickness $t_{p,}$ of the individual PZT layers. This constraint can be expressed in non-dimensional form as

$$E_a = \frac{V}{E_c \cdot t_p} \le 1 . \tag{7-11}$$

7.4.4 Optimization result

Running GA with the entire system model in MATLAB gets the optimization results. In contrast with the circuit optimization, the actuator uses its own model, as illustrated in section 7.2.2. The optimization study results indicate that the singular use of power loss or reactive power as objective function is not appropriate. The trade-off between P_{loss} and Qe circulating in the system is shown in Figure 7-10.

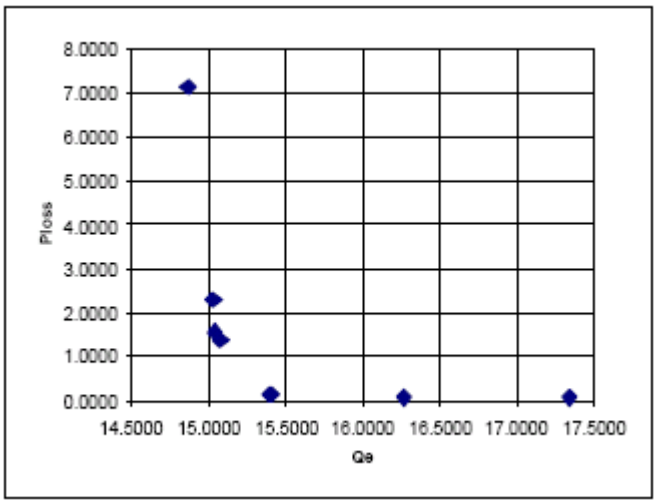


Figure 7-10 Pareto-optimal curve: trade-off between P_{loss} and Q_e

It is evident from the Pareto-optimal curve that if the reactive power circulating in the system, which determines the capacity of the power supply, is minimized, the power dissipation in the system is very high. In contrast, minimization of power loss only will lead to high reactive power. However, power loss increases manifold when reactive power decreases beyond 15.2 (even for a small decrease in reactive power) and vice versa. Thus a better-balanced solution can be obtained in the range [(2.4, 15.1) and (0.1, 15.4)], which has smaller power dissipation and the reactive power in the system. It is also noteworthy that although the reactive power in the above range increases from 15.1VA to 15.4VA, there is a great decrease in power loss from 2.4W to 0.1W. To get the above optimization result, the weight for the real power in the objective function α should be in the range of 0.25~0.72.

The relationship between the switching frequency and α is given in Figure 7-11. The switching frequency of the driving circuit will decrease when α becomes larger. The

reason for this is that the switching loss, which is proportional to the switching frequency of the circuit, is the dominating part in the real power dissipation of the circuit. If we minimize the real power, the switching frequency will be also minimized.

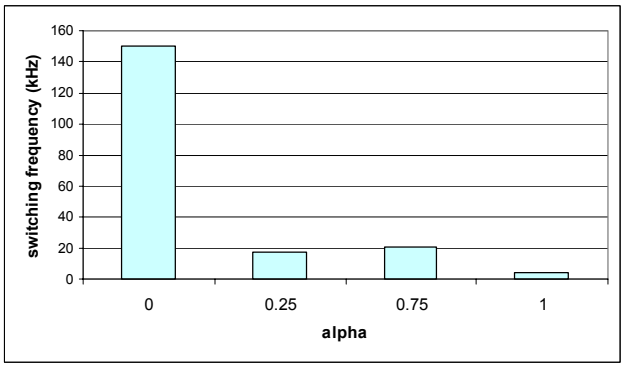
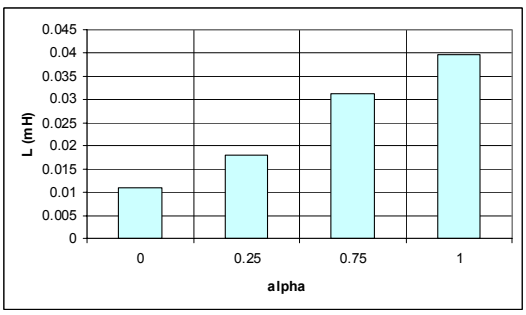
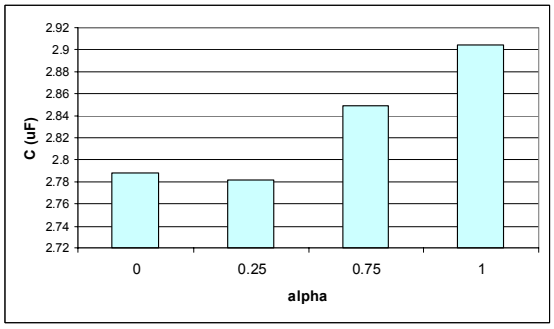


Figure 7-11 Switching frequency vs. α

When α is increased, which means the reactive power has a larger portion in the objective function, the inductor and capacitor in the circuit will be reduced where the reactive power is stored, shown in Figure 7-12.





(a) Inductance **(b) Piezo actuator equivalent capacitance**

Figure 7-12 Reactive components values. vs. α

7.5 Summary

The mathematical optimization of a switching amplifier and the PZT Recurve actuator as its load is proposed in this work. The power amplifier is composed of a flyback converter to step-up the input voltage, and a half-bridge circuit to generate the amplified reference signal. To focus on the methodology, only the half-bridge circuit is considered for optimization.

To be executable with commercial software, the average model of the half-bridge circuit is developed. Two separate optimization problems are presented: circuit optimization and system optimization. The purpose of circuit optimization is to design the amplifier in a nearly automatic way when the actuator has already been developed. The objective function is to minimize the total weight of the circuit, which includes the weight of the inductor, heat sink and bus capacitor. The weight of the heat sink must be considered in this problem because it connects the weight and the power dissipation of the circuit. However, when considering the interaction between the amplifier and the actuator, system optimization is needed. A multi-objective function is proposed as the combination of real power dissipation in the amplifier and the whole reactive power in the system.

The genetic algorithm (GA) is applied to this problem in order to make the optimization more realistic. The models for the circuit and the actuator are established in MATLAB, which has an interface with the GA algorithm.

The optimization result shows that the weight and the power dissipation of the circuit have been significantly reduced. This method can also be expanded to other similar problems for better design.

CHAPTER 8 SUMMARY AND FUTURE WORK

More Electric Aircraft is the trend for the future aircraft power systems, which is more reliable, lighter and smaller. As a result of this trend, the aircraft power system becomes more complex, and more power electronics techniques are applied. System simulation is necessary before hardware synthesis. The average modeling technique can reduce the system simulation time, and provides the basis for the small-signal model of the system-level study.

This dissertation has focused on the development of average models for line-commutated diode rectifiers and the application of average models of switching power converters in system-level study.

8.1 Summary

There are two main approaches to deriving average models for line-commutated diode rectifiers: mathematical derivation and the transfer function method. These two methods are described and compared in detail in Chapter 2. The transfer function method is to obtain the coefficients of the relationship between the input and output voltage/current by the data from detailed switching simulations or hardware experiments. It is straightforward and can deal with nonlinearity in the system, but it is limited to the static model. Mathematical derivation consists of averaging the differential equations derived during the commutation and conduction periods. Depending on the assumption of

the load current, either static or dynamic average model can be derived. Mathematical derivation is more suitable than the transfer function method for a variable-frequency system, which is the system of concern in this work.

Average models with improved dynamics of three-phase and nine-phase diode rectifiers are developed in Chapter 3 using the mathematical method. Assuming the load current using its first-order Taylor Series expansion, the boundary conditions of existing equations for dynamic average models are modified on the dc side. For ac currents, the averaged *dq*-axes currents are derived considering the dynamics of the load current.

For nine-phase diode rectifiers, the feeder's inductance before the autotransformer influences the commutation period as well. The total equivalent commutation inductance is a summation of this inductance referred to the secondary side and the secondary leakage inductance of the autotransformer. When the feeder's inductance is referred to the secondary side, the current transfer function of the autotransformer is used instead of the turns ratio because the secondary current is not sinusoidal. The current transfer function of the autotransformer is derived by combined equations of the Kirchoff current law at each node and the Ampere law for each leg of the autotransformer. The coefficient in the transfer function changes during different commutation instances. Because of the requirement of the averaging technique, the coefficients must be averaged in the entire line voltage period. For different topologies of autotransformers, the transfer function must be re-derived.

The time domain validation results for the improved average models are given in Chapter 4. Another two existing average models, the static average model and the dynamic average model, are described based on different load current assumptions. By

comparing the three average models with the switching model, the improved model is proven to have the best accuracy during both steady-state and transient conditions. The quantified results are given using the interpolation method. The parameter sensitivity for commutation inductance is also studied in this chapter.

The output impedance of the diode rectifier is an important characteristic for system-level study. After obtaining the average model, the output impedance can be derived following a standard linearization procedure, which is derived in Chapter 5. The feeder's inductance is now referred to the secondary side by multiplying the square of the autotransformer's turns ratio, which is different from the model for the commutation period calculation.

When the rectifier is connected with the generator, the generator impedance should be considered as well. The subtransient impedance of the generator is used for the commutation period calculation and total output impedance calculation.

It is well-known that average models of PWM converters are limited within half of the switching period. This limitation is still effective for average models of rectifiers. Chapter 5 includes Fourier analysis of the waveform of the rectifier under disturbance is given to show the sampling effect.

In Chapter 6, average models of switching power converters are applied to system harmonic resonance study. The system is composed of a synchronous generator, a nine-phase diode rectifier and a motor drive. The nine-phase diode rectifier, along with the generator, is modeled as a Thevenin's equivalent circuit. The VSI-controlled motor drive is modeled as a Norton's equivalent circuit. Each block represents a potential harmonic source of the system. The impedances of these equivalent circuits are obtained from

average models, and the harmonic sources are modeled by Fourier analysis from switching models under open-circuit or short-circuit conditions. Transfer functions from each harmonic source to the bus capacitor are then derived respectively. This method is proven to be effective for predicting the resonance in the system.

Some issues for resonance are discussed in this chapter. The relationship of stability and resonance is investigated, and the conclusion is that a more stable system does not guarantee less probability of having resonance. For the motor drive, its controller parameters influence the damping factor significantly, and there is an optimum bandwidth to have the highest damping factor at the resonance frequency.

Optimization is another application of the average modeling technique. It is demonstrated in this dissertation by optimizing a half-bridge circuit driving a piezoelectric actuator. In order to include different types of power devices into the design variables, a genetic algorithm is selected for optimization. The optimization is performed for the circuit at first. The objective function is the total weight of the circuit, including the inductor, bus capacitors and heat sinks for switches. When the switching frequency is a design variable, the weight of heat sinks cannot be ignored, which is to make a trade-off between the weight and the power dissipation. The system optimization is given after the circuit optimization to account for the interaction between the circuit and the load. Because energy is the direct interaction, the objective function is selected as the combination of the real power dissipation and the reactive power circulating in the system. Optimizations using the genetic algorithm are presented in Chapter 7. It is a powerful way to automatically design the actuator system.

8.2 Future Work

8.2.1 Average modeling of diode rectifier

Average models of line-commutated diode rectifiers in this dissertation have some limitations. First, it is only valid when a current transfer is completed during one switching period. When this condition is not satisfied, there are three intervals within one switching period instead of two (commutation and conduction) [38]. The average model needs to be re-derived following a similar procedure in this dissertation.

Second, the equivalent commutation inductance of the rectifier requires consideration of all the inductors before the rectifier. This becomes impossible if the network before the rectifier is complicated. Obtaining the equivalent commutation inductance in a complicated system is a challenge.

Third, modeling rectifiers in parallel is not discussed in this dissertation, yet it is very common in reality. Obtaining the equivalent commutation inductance for each rectifier is still a major challenge.

8.2.2 System resonance study

The Thevenin's and Norton's equivalent circuits are developed for system resonance study in this dissertation for system linearization. Even though there is only one branch in the system, this method is still valid when multiple branches are in parallel at the dc bus. Each block of switching power converters can be replaced by its equivalent circuit. The blocks could then be connected at the dc bus, though there might be more than two harmonic sources in the system. However, if some branches are in parallel at the ac bus,

this modeling method cannot be applied directly. More detailed analysis could be performed on the resonance phenomenon in multi-branch ac-dc system.

8.2.3 System Optimization

Optimization provides the possibility of designing the electronics circuit and the actuator automatically. It is effective, but the result is theoretical to some extent. Modifying the constraints might generate more practical design.

Furthermore, a global/local optimization method could be utilized when optimizing a complicated system [106]. The multi-level modeling of the system is the prerequisite of the optimization. This optimization method is feasible when there are many design variables and constraints in a large system.

REFERENCE

MEA

[1] Joseph A. Weimer, "Past, present & Future of Aircraft Electrical Power Systems", 39th AIAA Aerospace Sciences Meeting & Exhibit, Jan 8-11, 2001, Reno, Nevada

[2] A.K.Hyder, "A Century of Aerospace Electrical Power Technology", Journal of Propulsion and Power, Vol.19, No.6 November-December 2003, pp1155-1179

[3] Richard E. Quigley, "More Electric Aircraft", Applied Power Electronics Conference and Exposition, 1993. APEC '93. Conference Proceedings 1993., Eighth Annual 7-11 March 1993 pp 906 – 911

[4] R I Jones, "The More Electric Aircraft: The Past and the Future?", Electrical Machines and Systems for the More Electric Aircraft (Ref. No. 1999/180), IEE Colloquium on 9 Nov. 1999 pp1/1 - 1/4

[5] Ian Moir, "The ALL-Electric Aircraft – Major Challenges", All Electric Aircraft (Digest No. 1998/260), IEE Colloquium on 17 June 1998 pp 2/1 - 2/6

[6] Ian Moir, "More-Electric Aircraft –System Considerations", Electrical Machines and Systems for the More the More Electric the More Electric Aircraft (Ref. No. 1999/180), IEE Colloquium On 9 Nov. 1999 pp10/1 – 10/9

[7] James S. Cloyd, "Status of the United States Air Force's More Electric Aircraft Initiative", IEEE AES Systems Magazine, Vol.13, Issue 4, April, 1998, pp17-22

[8] A. Emadi and M.Ehsani, "Aircraft Power Systems: Technology, State of the Art, and Future Trends", IEEE AES Systems Magazine, January, 2000, pp28-32

[9] Mike Bailey, Neville Hale, Gian Ucerpi, Jo-Anne Hunt, Stefan Mollov and Andrew Forsyth, "Distributed Electrical Power Management Architecture", Electrical Machines and Systems for the More Electric Aircraft (Ref. No. 1999/180), IEE Colloquium on 9 Nov. 1999 pp 7/1 - 7/4

[10] Miguel A. Maldonado, Naren M. Shah, Keith J. Cleek, Paramjit S. Walia and George J. Korba, "Power Management and distribution system for a more-electric aircraft (MADMEL) – program status", Aerospace and Electronic Systems Magazine, IEEE Volume 14, Issue 12, Dec. 1999 pp 3 - 8

[11] Carl Burleson and Lourdes Maurice, "Aviation and the Environment: Challenges and Opportunities", AIAA/ICAS International Air and Space Symposium and Exposition, July 14-17, 2003, Dayton, Ohio

[12] Konstantin P. Louganski, "Modeling and Analysis of a DC Power Distribution System in 21st Century Airlifters", Master thesis, Virginia Tech, Blacksburg, 1999

AC-DC Converter for aircraft power system

[13] J, Weimer, "Power Electronics in the More Electric Aircraft", 40th AIAA Aerospace Sciences Meeting & Exhibit, Jan 14-17, 2002, Reno, Nevada

[14] Mohamad H Taha, "Power Electronics for Aircraft Application", Power Electronics for Demanding Applications (Ref. No. 1999/059), IEE Colloquium on 15 April 1999 pp 7/1 - 7/4

[15] Louis J. Feiner, "Power electronics for transport aircraft applications", in Proc. of the IECON '93, Nov. 15-19, 1993, Vol. 2, pp. 719 – 724

[16] Louis J. Feiner, "Power Electronics Transforms Aircraft Systems", WESCON/94. 'Idea/Microelectronics'. Conference Record 27-29 Sept. 1994 pp166 – 171

[17] K.W.E.Cheng, "Comparative Study of AC/DC Converters for More Electric Aircraft", Power Electronics and Variable Speed Drives, 1998. Seventh International Conference on (IEE Conf. Publ. No. 456) 21-23 Sept. 1998 pp 299 – 304

[18] Guanghai Gong, Marcelo Lobo Heldwein, Uwe Drofenik, Johann Minibock, Kazuaki Mino and Johann W.Kolar, "Comparative Evaluation of Three-Phase High-Power-Factor AC-DC Converter Concepts for Application in Future More Electric Aircraft", IEEE Transactions on Industrial Electronics, Vol 52, No.3 June 2005 pp 727-737

[19] Bulent Sarlioglu, "Power Quality Solutions Using Active and Passive Rectification for Future More Electric Aircraft", SAE Power Systems Conference, Reno, Nevada, Nov 2-4, 2004

[20] Kaz Furmanczyk and Mark Stefanich, "Demonstration of Very High Power Airborne AC to DC Converter", SAE Power Systems Conference, Reno, Nevada, Nov 2-4, 2004

[21] IIeana Rusan and David Lazarovich, "Design and Integration of DC Power System with Regulated Transformer Rectifiers", SAE Power Systems Conference, Coral Springs, Florida, Oct 29-31, 2002

[22] Alexander Uan-Zo-Li, Rolando Burgos, Fred Wang, Dushan Boroyevich and Alain Tardy, "Comparison of Prospective Topologies for Aircraft Autotransformer-Rectifier Units", Industrial Electronics Society, 2003. IECON '03. The 29th Annual Conference of the IEEE Volume 2, 2-6 Nov. 2003 Page(s):1122 - 1127 Vol.2

[23] F.J.Chivite-Zabalza, A.J.Forsyh and D.R.Trainer, "Analysis and practical evaluation of an 18-pulse rectifier for aerospace applications", Power Electronics, Machines and Drives, 2004. (PEMD 2004). Second International Conference on (Conf. Publ. No. 498)

[24] Lev Sorkin, Eli Liebermann and Cory Ackerman, "Low-Weight, Los Cost AC/DC Converter for the V-22", SAE Power Systems Conference, Coral Springs, Florida, Oct 29-31, 2002

[25] Bill Johnson, Benino Casimir, Bob Hanson, John Fitzpatrick and George Pusey, "Development of 200 Ampere Regulated Transformer Rectifier", SAE Aerospace Power Systems Conference, Mesa, Arizona, Apr 6-8, 1999

Average model

[26] V.Rajagopalan, "Modeling and simulation of power electronic converters for power supplies", Industrial Electronics, Control, and Instrumentation, 1995., Proceedings of the 1995 IEEE IECON 21st International Conference on Volume 1, 6-10 Nov. 1995 pp 27 - 32 vol.1

[27] Jih-Sheng (Jason) Lai, "Power Electronics System Modeling and Simulation",

Computers in Power Electronics, 1994., IEEE 4th Workshop on 7-10 Aug. 1994 pp 45 – 55

[28] A.M.Gole, Albert Keri, C.Nwankpa, E.W.Gunther, H.W.Dommel, I.Hassan, J.R.Marti, J.A.Martinez, K.G.Fehrle, L.Tang, M.F.McGranaghan, O.B.Nayak, P.F.Ribeiro, R.Iravani, R.Lasseter, "Guidelines for Modeling Power Electronics in Electric Power Engineering Applications", IEEE Transactions on Power Delivery, Vol. 12, No.1, Jan 1997, pp505-514

[29] P.J.van Duijsen, "Multi-level Modeling and Simulation of Power Electronics Systems", Proceedings EPE Brighton, England 1993

[30] Zoran Mihailovic, "Modeling and Control Design of VSI-FED PMSM Drive Systems with Active Load", Master thesis, Virginia Tech, Blacksburg, 1998

[31] R.D.Middlebrook, "Input Filter Considerations in Design and Application of Switching Regulators", in IEEE proc. IASAM, 1976

[32] R.D.Middlebrook and Solbodan Cuk, "A General unified approach to modeling switching-converter power stages," in IEEE PESC Rec. 1976, pp. 18-34.

[33] Seth R.Sanders, J.Mark Noworolski, Xiaojun Z.Liu and George C. Verghese, "Generalized Averaging Method for Power Conversion Circuits", IEEE Transactions on Power Electronics, Vol. 6, No.2, April 1991 pp251-259

[34] Seth Sanders, S.R.; Noworolski, J.M.; Liu, X.Z.; Verghese, G.C, "Generalized Averaging Method for Power Conversion Circuits", Power Electronics, IEEE Transactions on Volume 6, Issue 2, April 1991 pp 251 – 259

[35] Emadi, A.; Abur, A, "Real Time State Estimation of Multi-Converter DC Power Electronic Systems Using Generalized State Space Averaging Method", Power

Electronics Specialists Conference, 2002. PESC 02. 2002 IEEE 33rd Annual Volume 2, 23-27 June 2002 pp 881 - 886

[36] Emadi, A, "Modeling of Power Electronic Loads in AC Distribution Systems using the Generalized State Space Averaging Method", Industrial Electronics, IEEE Transactions on Volume 51, Issue 5, Oct. 2004 pp 992 – 1000

[37] Dushan Boroyevich, "Modeling and Control of 3-phase PWM Converters", class notes, Blacksburg, Virginia Tech 2004

[38] Kimbark, Edward Wilson, "Direct Current Transmission", Volume I, New York, Wiley-Interscience, 1971

[39] Erickson, Robert W., "Fundamentals of Power Electronics", New York : Chapman & Hall, 1997

[40] Kassakian, John G., "Principles of Power Electronics", Addison-Wesley, 1991

[41] Paul C. Krause, Oleg Wasynczuk, S.D.Sudhoff, "Analysis of Electric Machinery and drive systems", New York: IEEE Press, 2002, pp 395-425

[42] S.D.Sudhoff, and O.Wasynczuk, "Analysis and Average-Value Modeling of Line-commutated Converter-Synchronous Machine Systems," IEEE Trans. of Energy Conversion, vol. 8, no. 1, Mar. 1993, pp 92-99.

[43] S.D.Sudhoff, K.A.Corzine, H.J.Hegner and D.E.Delisle, "Transient and dynamic average-value modeling of synchronous machine fed load-commutated converters," IEEE Trans. of Energy Conversion, vol. 11, no. 3, Sep. 1996, pp 508-514.

[44] Wolfgang Hammer, "Dynamic modeling of Line and Capacitor Commutated Converters for HVDC Power Transmission," Ph.D dissertation, Swiss Federal Institute of Technology Zurich, 2003, pp 45-63

[45] S.D.Sudhoff, "Analysis and average-value modeling of dual line-commutated converter – 6 phase synchronous machine systems," IEEE Trans. of Energy Conversion, vol. 8, no. 3, Sep. 1993, pp 411-417.

[46] C.A.Baghramian, A.J. Forsyth, "Average-value models of twelve-pulse rectifier for aerospace applications", in Proceeding of 2nd International Conference on Power Electronics, Machines and Drives, 2004, vol. 1 pp 220-225.

[47] Juri Jatskevich, Eric A. Walters, Charles E. Lucas and Peter T. Lamm, "Average-Vaule Model of a High-Frequency Six-Phase Generation System", SAE Power Systems Conference, Reno, Nevada, Nov 2-4, 2004

[48] Ivan Jadric, Dushan Boroyevich, Martin Jadric, "A simplified model of a variable speed synchronous generator loaded with diode rectifier," in IEEE PESC Rec. 1997., vol. 1, pp 497-502.

[49] Ivan Jadric, Dushan Boroyevich, Martin Jadric, "Modeling and Control of a Synchronous Generator with an Active DC Load," IEEE Trans. on Power Electronics, vol. 15, no. 2, Mar. 2000, pp 303-311.

[50] C.T.Tinsley, E.M.Hertz, R. Carie, D.Boroyevich, "Average modeling of a hexagon transformer and rectifier," in IEEE PESC Rec. 2003, vol. 4 pp. 1505-1509.

[51] Jatskevich, J.; Aboul-Seoud, T., "Impedance Characterization of a Six-Phase Synchronous Generator-Rectifiers System using Average-Value Model", Electrical and Computer Engineering, 2004. Canadian Conference on Volume 4, 2-5 May 2004 pp 2231 - 2234

[52] Alexander Uan-Zo-Li, Frederic Lacaux, Rolando Burgos, Fred Wang and Dushan Boroyevich, “Multi-level Modeling of Autotransformer Rectifier Units for Aircraft Applications”, CPES seminar, 2004, pp 726-730

[53] Uan-Zo-li, A.; Burgos, R.P.; Lacaux, F.; Wang, F.; Boroyevich, D., “Assessment of multipulse converter average models for stability studies using a quasistationary small-signal technique”, Power Electronics and Motion Control Conference, 2004. IPEMC 2004. The 4th International Volume 3, 14-16 Aug. 2004 pp1654 - 1658

[54] S.D.Sudhoff, "Waveform Reconstruction from the Average-Value Model of Line-commutated Converter-Synchronous Machine Systems," IEEE Transactions on Energy Conversions, Vol.8, No.3, Sep 1993, pp 404-410

[55] J.T.Alt and S.D.Sudhoff, "Average value modeling of finite inertia power systems with harmonic distortion," in Proceeding of SAE Power systems conference, Oct, 2000.

[56] Fred C. Lee, “Power Converter Modeling and Control”, class notes, Blacksburg, Virginia Tech, 2003.

[57] Arthur R. Brown and R.D.Middlebrook, "Sampled-Data Modeling of Switching Regulators," In: PESC '81; Power Electronics Specialists Conference, Boulder, CO, June 29-July 3, 1981, Record. New York, Institute of Electrical and Electronics Engineers, Inc., 1981, pp 349-369

[58] Raymond B. Ridley, "A New, Continuous-Time Model for Current-Mode Control”, IEEE Transactions on Power Electronics, Vol.6, No.2, Apr 1991, pp 271-280

[59] David J. Perreault and George C. Verghese, "Time-Varying Effects and Averaging Issues in Models for Current-Model Control" IEEE Transactions on Power Electronic, Vol.12, No.3, May 1997, pp453-461

[60] Philip T.Krein, Joseph Bentsman, Richard M. Bass and Bernard L. Lesieutre, "On the Use of Averaging for the Analysis of Power Electronic Systems", IEEE Transactions on Power Electronic, Vol.5 No.2, May 1990, pp182-190

[61] J.A.Sanders, F.Verhulst, "Averaging Methods in Nonlinear Dynamical Systems", Springer-Verlag, New York, 1985

[62] Soumitro Benerjee, George C. Verghese, "Nonlinear Phenomena in Power Electronics: Attractors, Bifurcations, Chaos, and Nonlinear control", IEEE Press, New York, 2001

[63] R.Scott Copper, "The Designer's Guide to Analog & Mixed-Signal Modeling", Avant! Corporation

[64] D.Boroyevich, F.Wang, D.Lindner and F.C.Lee, "Modeling & Simulation of Aircraft Power Systems – Switching Models User's Guide", report, Blacksburg, Virginia Tech, 2005

[65] Mohamed Belkhayat, "DQ Impedance Extraction Techniques", report, 2005

Resonance

[66] Massey, G.W, "Power distribution system design for operation under nonsinusoidal load conditions", Industry Applications, IEEE Transactions on Volume 31, Issue 3, May-June 1995 pp 513 – 519

[67] Yousin Tang and Alex Y. Wu, "Harmonics and System Natural Frequencies", Cement Industry Technical Conference, IEEE-IAS/PCA 2001. 29 April-3 May 2001 pp 51 – 58

[68] Ali Mihirig, "Harmonic Study Analysis Guidelines for Industrial Power Systems", Electricity Today Magazine, Issue 3, 2001

[69] Fang Z. Peng and Donald J. Adams, "Harmonic Sources and Filtering Approaches – Series/Parallel, Active/Passive, and Their Combined Power Filters", Industry Applications Magazine, IEEE Volume 7, Issue 4, July-Aug. 2001 pp 18 – 25

[70] Zhenyu Huang, Wilsun Xu and V.R.Dinavahi, "A Practical Harmonic Resonance Guideline for Shunt Capacitor Applications", IEEE Transactions on Power Delivery, Vol.18, No.4, Oct 2003, pp1382-1387

[71] Roger C. Dugan and Barry W. Kennedy, "Predicting Harmonic Problems Resulting From Customer Capacitor Additions for Demand-Side Management", IEEE Transactions on Power Systems, Vol.10, No.4, Nov 1995, pp1765-1772

[72] Evan J. Currence, John E. Plizga and Howard N. Nelson, "Harmonic Resonance at a Medium-Sized Industrial Plant", IEEE Transactions on Industry Applications, Vol.31, No.4, Jul/Aug 1995, pp 682-690

[73] A.David Graham, "Non characteristic line harmonics of PWM AC-DC converters", Harmonics and Quality of Power, 2000. Proceedings. Ninth International Conference on Volume 3, 1-4 Oct. 2000 pp 955 - 960

[74] Guy Lemieux, "Power System Harmonic Resonance - A Documented Case", IEEE Transactions on Industry Applications, Vol.26, No.3, May/Jun 1990, pp 483-488

[75] Z. Chen, F.Blaabjerg and J.K.Pedersen, "Harmonic Resonance Damping with A Hybrid Compensation System in Power Systems with Dispersed Generation", Power Electronics Specialists Conference, 2004. PESC 04. 2004 IEEE 35th Annual Volume 4, 2004 pp 3070 - 3076

[76] Hideaki Fujita, Takahiro Yamasaki and Hirofumi Akagi, "A Hybrid Active Filter for Damping of Harmonic Resonance in Industrial Power Systems", IEEE Transactions on Power Electronics, Vol.15, No.2, March 2000, pp 215-222

[77] Hirofumi Akagi, "Control Strategy and Site Selection of a Shunt Active Filter for Damping of Harmonic Propagation in Power Distribution Systems", IEEE Transactions on Power Delivery, Vol.12, No.1, Jan 1997, pp 354-363

[78] Ikuo Kawaguchi, Akinobu Okui, Haruo Ikeda and Kouki Matsuse, "Harmonic Resonance Phenomenon in the DC Circuit of Inverter to Drive LSM", Power Conversion Conference, 2002. PCC Osaka 2002. Proceedings of the Volume 3, 2-5 April 2002 pp 1009 - 1014

[79] Toshihiko Tanaka, Shinji Fujikawa and Shigeyuki Funabiki, "A New Method of Damping Harmoic Resonce at the DC Link in Large-Capacity Rectifier-Inverter Systems Using a Novel Regenerating Scheme", IEEE Transactions on Industry Applications, Vol.38, No.4, Jul/Aug 2002, pp 1131-1138

[80] Bathurst, G.N.; Arrillaga, J.; Watson, N.R.; Wood, A.R., "Advanced Modeling of the Harmonic Impedances of AC-DC Converters", Generation, Transmission

and Distribution, IEE Proceedings-Volume 149, Issue 6, Nov. 2002 pp700 – 704

[81] S.Rosado, X.Ma, C.Han, F.Lacaux, F.Wang and Dushan Boroyevich, "Model-Based Digital Controller for a Variable Frequency Aircraft Synchronous Generator with Brushless Exciter", CPES seminar, 2004, pp 692-697

[82] Pragasan Pillay and R. Krishnan, "Modeling of Permanent Magnet Motor Drives", IEEE Transactions on Industry Electronics, Vol.35, No.4, Nov 1988, pp 537-541

[83] Carl M. Wildrick, Fred C. Lee, Bo H. Cho and Byungcho Choi, "A Method of Defining the Load Impedance Specification for a Stable Distributed Power System", IEEE Transactions on Power Electronics, Vol.10, No.3, May 1995, pp 280-285

[84] S.D.Sudhoff, S.D.Pekarek, S.F.Glover, S.H.Zak, E.Zivi, J.D.Sauer and D.E.Delisle, "Stability Analysis of a DC Power Electronics Based Distribution System", SAE Power Systems Conference, Coral Springs, Florida, Oct 29-31, 2002

[85] Derek A. Paice, "Power Electronic Converter Harmonics: Multipulse Methods for Clean Power", IEEE Press, Piscataway, NJ. 1996

Optimization

[86] Christopher Niezrecki, Diann Brei, Sivalumar Balakrishnan, and Andrew Moskalik, "Piezoelectric Actuation: State of the Art", Shock and Vibration Digest, Vol. 33, No. 4, 2001, pp 269–280

[87] Lindner, D.K., M. Zhu, N. Vujic, and D. Leo, "Comparison of linear and switching drive amplifiers for piezoelectric actuators", Proceedings of the AIAA/ASME/ASCE/AHS/ASC 43th Structures, Structural Dynamics, and Materials Conference, Denver, CO, April, 2002, paper number AIAA 2002-1352.

[88] Jiyuan Luan and Fred C. Lee, "Design of a High Frequency Switching Amplifier for Smart Material Actuators with Improved Current Mode Control," Power Electronics Specialists Conference,. 29th Annual IEEE, PESC 98 Record, Volume 1, pp 59-64, 1998

[89] Lindner, D. K., H. Zhu, C. Song, W. Huang, D. Cheng, "Low Input Voltage Switching Amplifiers for Piezoelectric Actuators," Proceedings of SPIE's 2002 North American Symposium on Smart Structures and Materials: Industrial and Commercial Applications of Smart Structures Technologies, Vol. 4698, Anne-Marie McGowen, Ed., San Diego, CA, March 18-21, 2002, pp. 282-292

[90] Chandrasekaran, S., S. A. Ragon, D. K. Lindner, Z. Gurdal, and D. Boroyevich, "Optimization of an Aircraft Power Distribution Subsystem," Journal of Aircraft 2003 0021-8669 vol.40 no.1 pp16-26

[91] Frecker, M., "Recent Advances in Optimization of Smart Structures and Actuators", Journal of Intelligent Material Systems and Structures, Vol.14, No.4/5, Apr/May, 2003, pp207-216.

[92] Ridley R.B., C. Zhou, and F.C. Lee, "Application of Nonlinear Design Optimization for Power Converter Components", IEEE Transactions on Power Electronics, vol.5, no.1, January 1990, pp 29-39.

[93] Ashraf W. Lotfi, Qing Chen and Fred C. Lee, "A Nonlinear Optimization Tool for the Full-Bridge Zero-Voltage-Switched DC-DC Converter", Proceedings of the Power Electronics Specialists Conference, PESC'92 Record., 23rd Annual IEEE, 1992, pp 1301-1309.

[94] S.J. Wang and Y.S. Lee, "Development of an Expert System for Designing, Analyzing and Optimizing Power Converters", Proceedings of the 19th Convention of Electrical and Electronics Engineers, Israel, 1996, pp 359-362.

[95] S.J. Wang, Y.S. Lee etc, "Expert System Aided Design, Simulation and Optimization of Power Converters", Industrial Electronics, Proceeding of the 23rd International Conference on Power Electronics, Vol 3, 1997. pp 1016-1021.

[96] C.Song and D.K.Lindner, "Optimization of Drive Amplifiers for Smart Materials", Proceeding of 2nd Canada-US Workshop on Smart Materials and Structure, Montreal, Quebec, Canada, October, 2002

[97] Song, C., Lindner, D.K., Abdalla, M.M., Gürdal, Z., "Energy Optimization of Driving Amplifiers for Smart Actuators", annual report, Blacksburg, Virginia Tech, 2002

[98] Busquets-Monge, S.; Soremekun, G.; Hertz, E.; Crebier, C.; Ragon, S.; Zhang, J.; Boroyevich, D.; Gurdal, Z.; Lindner, D.K.; Arpilliere, M., "Design optimization of a boost power factor correction converter using genetic algorithms", Applied Power Electronics Conference and Exposition, 2002. APEC 2002. Seventeenth Annual IEEE Volume 2, 10-14 March 2002 pp 1177 - 1182

[99] Busquets-Monge, S.; Crebier, J.-C.; Ragon, S.; Hertz, E.; Boroyevich, D.; Gurdal, Z.; Arpilliere, M.; Lindner, D.K., " Design of a boost power factor correction converter using optimization techniques," Power Electronics, IEEE Transactions on Volume 19, Issue 6, Nov. 2004 pp 1388 – 1396

[100] D. E. GoldBerg, Genetic Algorithms in Search, Optimization, and Machine Learning, Addison-Wesley Publishing Company, Inc., Reading, MA, 1989.

[101] Abdalla, M.M., Gürdal, Z., and Lindner, D.K., "Design of a Recurve Actuator for Maximum Energy Efficiency", 44th AIAA/ASME/ASCE/AHS/ASC Structures, Structural Dynamics, and Materials Conference, AIAA Paper 2003-1804.

[102] Song, C., M. M. Abdalla, D. K. Lindner, and Z. Gürdal, "Combined Optimization of Active Structural Systems and Drive Circuits," Proceedings of SPIE's 2002 North American Symposium on Smart Structures and Materials: Modeling, Signal Processing, and Control, Vol. 4693, Vital S. Rao, Ed., San Diego, CA, March 18-21, 2002, pp. 136-147.

[103] Zhu, H.; Ragon, S.; Lindner, D.K.; Abdalla, M.M.; Seresta, O.; Gurdal, Z., "Optimization of Driving Amplifiers for Smart Actuators Using Genetic Algorithm", Industrial Electronics Society, 2003. IECON '03. The 29th Annual Conference of the IEEE Volume 3, 2-6 Nov. 2003 pp 2951 - 2956

[104] McMahon, M.T., Waston, L.T., Soremekun, G.A., Gürdal, Z., and Haftka, R.T., "A Fortran 90 Genetic Algorithm Module for Composite Laminate Structure Design", Eng. Computers, Vol 14, 1998, pp 260-273

[105] Aavid thermalloy website

[106] Scott Ragon, "Development of a Global/Local Approach and a Geometrically Non-linear Local Panel Analysis for Structural Design", Ph.D Dissertation, Blacksburg, Virginia Tech, 1998

VITA

The author, Huiyu Zhu, was born in Shijiazhuang, Hebei, China on August 8th, 1974. She received her B. S. and M. S. degrees from Tsinghua University, China in 1998 and 2000 respectively, both in electrical engineering. She started her PhD program at Virginia Tech in the fall 2000 as a graduate research assistant at the Center of Power Electronics Systems. Her research work has been concentrated on average modeling of the switching power converter, DC power system resonance study, optimization in power electronics and actuator. She will join the Linear Technology at San Jose, California as an application engineer.